Politecnico di Torino

Avio Aero
a GE Aerospace company

Effect of different turbulence models on stability flutter evaluation of an LPT rotating blade

Master's degree in aerospace engineering, A.A.2023/2024

Department of Mechanics and Aerospace, DIMEAS.
Master's Degree Thesis

Supervisors:
Prof. Giuseppe Battiato
Ing. Antonio Giuseppe D'Ettole

Candidate
Micaela Perillo *s301823*

Contents

List of figures

List of Tables

Abstract

The most important goals of the Aviation nowadays are improving fuel efficiency and reducing emissions as well as noise. Such goals usually require designing lighter components, which are more prone to mechanical vibrations. In this regard blades are the most critical components in term of high cycle fatigue (HFC) failure occurrence.

This Master Thesis work is developed in collaboration with Avio Aero and its purpose is to evaluate the flutter stability of a Low Pressure Turbine (LPT) blade. The case of study is the blade of the LPT ARiAS test article. ARiAS (Advanced Research into Aeromechanical Solutions) is a Horizon 2020 funded Research Project in the field of aeronautical engineering whose objective is to improve the predictive capability of numerical methods used to analyze aerodynamically induced blade vibrations in aircraft engines.

The aim of this Thesis Work is to analyze the predictive capability of non-linearized flutter solvers with different turbulence closure models. If the flow field is either transonic or supersonic, the non-linearized method is necessary.

Comparison of flutter stability results, computational times and convergence error have been investigated for the turbulence models Wilcox k-w and RQEVM k-w (Realizable Quadratic Eddy Viscosity Model).

1 Introduction

Nowadays the main goals of aeronautical industry are: polluting emission reduction (in particular NOx and CO2), noise abatement, maximum performance and cost reduction. One of the ways in which these goals could be achieved is the aero-engine weight reduction.
This can help to decrease the total cost of maintenance, but leads to fewer mechanical parts and higher blade loads.
The consequences to these choices are more flexible and more loaded blades. In these conditions, the major problems are *vibrations* caused by aeroelastic phenomena due to the interaction between solid and fluid, such as forced response and flutter, that are more evident.
It is important to analyze these phenomena in order to predict and to avoid high cycle fatigue failures caused by excessive blade vibrations.

This Master's Thesis is structured as follows:

- **Chapter 1** : contains a short introduction about the E-TDC, different types of Aircraft Engines and the ARiAS Project that is the main subject;
- **Chapter 2** : is about theoretical concepts that are the fundamentals to understand Rotor Dynamics;
- **Chapter 3** : explanation of the concept of Aeroelasticity, in particular the Flutter phenomenon;
- **Chapter 4** : contains theoretical concepts useful to understand Computational Fluid Dynamics, in particular Turbulent Flow and its Closure Models used in the tests carried out;
- **Chapter 5** : is the core of this Thesis work in which are explained the simulations that have been made in these months regarding Flutter phenomenon and the results obtained;
- **Chapter 6** : conclusive chapter, in which are reported the considerations about tests carried out.

1.1 What is E-TDCs?

The E-TDCs, European Technology Development Clusters, launched in May 2020, is a network operating into the Research and Innovation Field, with a unique collaborative model in Europe, whose members work together under one single framework agreement which defines financial provisions, IP rules, dissemination, publications.
The E-TDCs include up today 39 parties: 16 Universities, 7 Research Institutions, 4 SMEs and 12 GE Affiliates, see Fig. 1. The Academia, Research Centers and SMEs involved have proven technical and scientific skills, as well as unique experimental assets and expertise in the collaborative Research and Innovation environment. The E-TDCs count 10 different Clusters, consisting of Research Institutions and GE Aerospace teams, each of them focused on dedicated disciplines or products of GE Aerospace interest, set up taking into consideration the complementarity of knowledge and operating on the basis of an Innovation Plan with the following responsibilities:

- to execute and monitor the Innovation Plan and monitor the international scientific scenario;
- to leverage the complementary knowledge and capability of teams;
- to propose, where necessary, extension of the collaboration to other research teams;
- to promote, where necessary, integration with SMEs;
- to evaluate financing opportunities through participation external funded projects;
- to manage publications and events to disseminate the results obtained;
- to identify, train and involve new talent, including through degree theses, PhD, etc;
- to develop skills and highly specialized human resources.

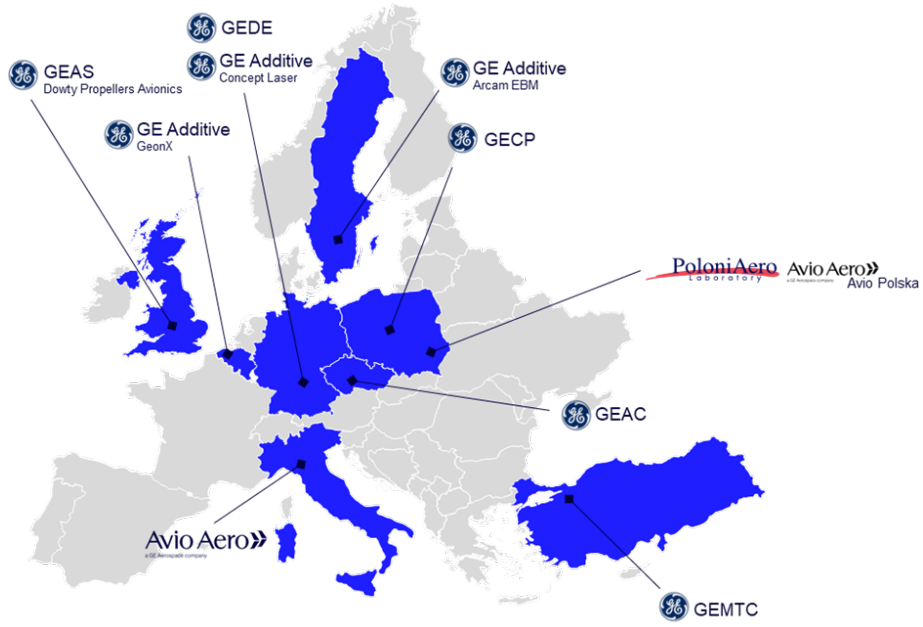

Figure 1: E-TDCs Network and Clusters

Figure 2: E-TDCs Network and Clusters 2

The network extension and the Clusters progress, results, and ongoing plans are overseen trough a well-established Governance structure, see Figure 3, which defines Operating Rhythm and key actors. Just in November 25th it has been held the 2021 edition of the E-TDCs Annual Event: LKD. [1]

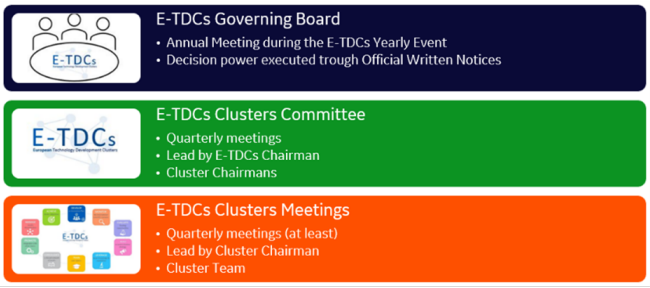

Figure 3: E-TDCs Governance

1.2 Aicraft Engines

In aviation there are different type of engines used in different application. They are in constant evolution to satisfy the requirements in term of emissions and performances. The following engines are based on the Joule-Brayton Cycle: the flow flux is compressed at first in the inlet, then it is compressed again in a compressor, the supply of energy occurs through the chemical reactions that take place in the combustor. Lastly, the flux expands in the turbine and eventually also in a nozzle.

1.2.1 Turbojet

It is the simplest and oldest engine. Its task is to produce the necessary thrust, according to the third principle of dynamic. Today is not used anymore because the turbofan has taken its place. The performances are represented by:

- Specific Thrust $I_a = \frac{S}{\dot{m}}$;
- Specific Consumption of Thrust $q_s = \frac{\dot{m}_b}{S}$;
- Thermal Efficiency $\eta_\theta = \frac{P_c}{\dot{m}_b H_i}$ where P_c is the kinetical power of thrust, defined as difference between the kinetical energy of exhaust gases and air in inlet.

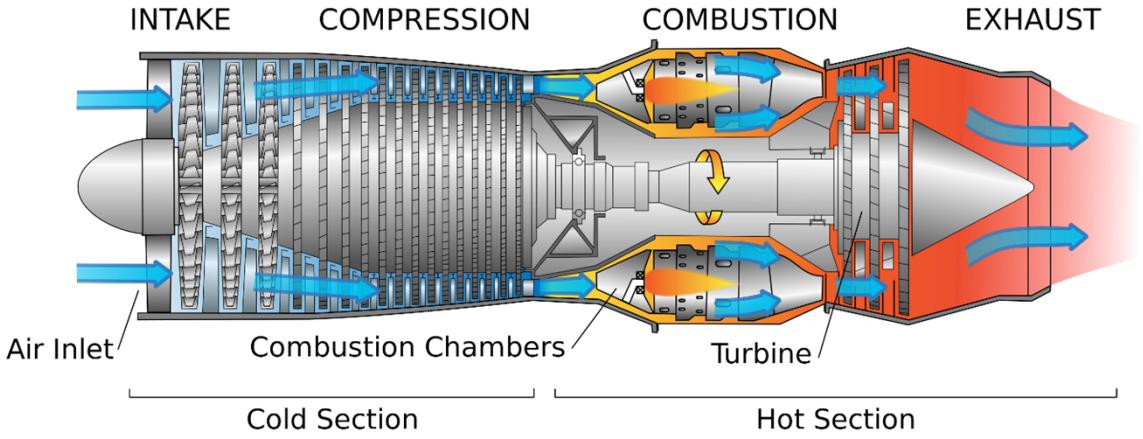

Figure 4: Turbojet Cold and Hot Sections
[5]

1.2.2 Turbofan

The turbofan is an airbreathing jet engine, that took the place of the turbojet. The flow is divided in two parts: a cold flow and a hot flow. Downstream of the inlet, there was introduced a Fan, to split the flow entering the engine. The hot flow, also called core flow, proceeds through a second compressor, the combustion chamber, and generally a low-pressure and high-pressure turbine. The flow exits the engine through a nozzle, where is reunited with the cold flow. It was invented to improve the performances, to reduce the fuel consumption of turbojet. It is important to introduce the following parameters:

- By Pass Ratio $BPR = \frac{\dot{m}_c}{\dot{m}_h}$, where $\dot{m}_c$ is the mass of the cold flow and $\dot{m}_h$ is the hot one;
- Propulsion Efficiency $\eta_p = \frac{P_t}{P_t+P_d} = \frac{2}{1+\frac{v_g}{v_0}}$, where P_t is the thrust power, P_d is the dissipated power, v_g is the gasses velocity and v_0 is the aircraft velocity;
- Thermal Efficiency $\eta_{th} = \frac{P_k}{P_{ch}}$, where P_k is the kinetic power and P_{ch} is the chemical power contained in the fuel;
- Global Efficiency $\eta_g = \eta_p \eta_{th}$.

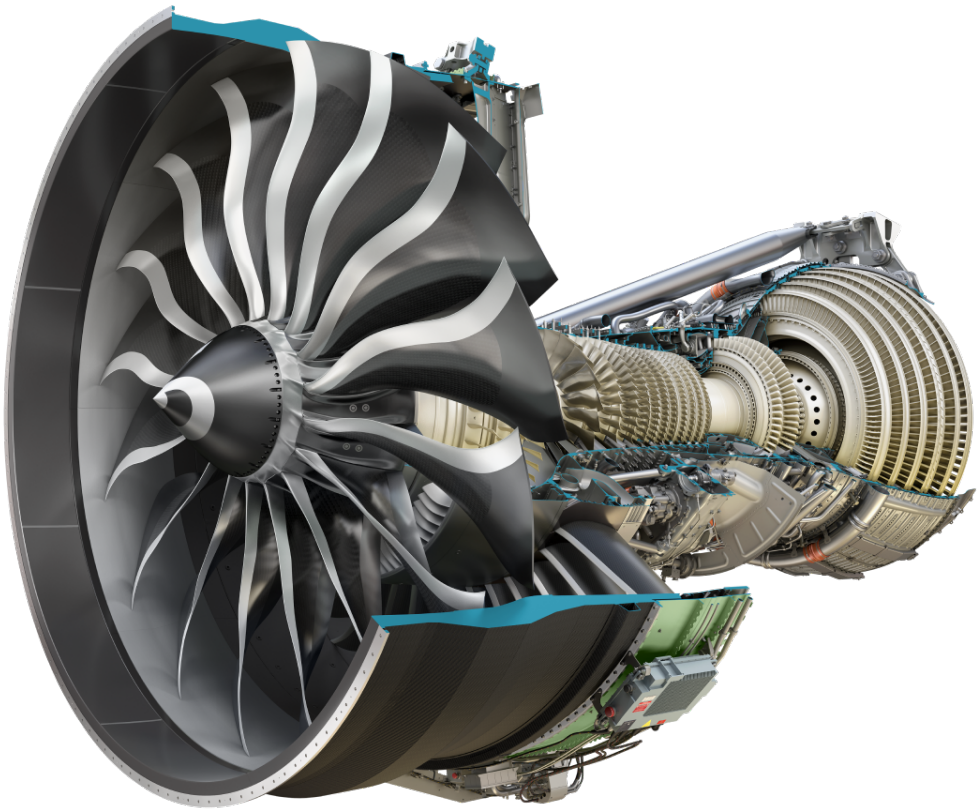

Figure 5: Turbofan GE9X Section
[6]

1.2.3 Turboprop

It is composed by a propeller that is driven by a turbine. It is different from the turbojet engine, because with the turboprop the propulsion is mainly by air set in motion by the rotation of a propeller and to a lesser extent by the thrust of exhaust gases.
Compared with the turbojet, the turboprop allows lower cruise speed and higher noise than turbofan engine.
The advantages of the turboprop are lower fuel consumption, higher thrust at take off and higher efficiency at low altitude.
They are used on really much transportation aircraft, military and domestic, with a limitation due to the efficiency loss if the speed increases.

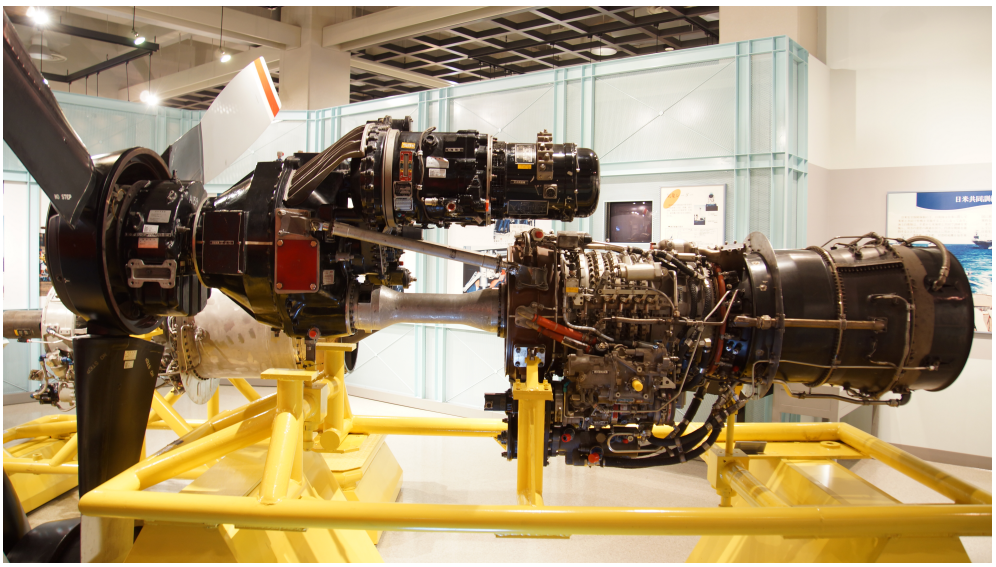

Figure 6: Turboprop Engine
[7]

1.2.4 Turboshaft

Its task is to produce Power to provide one or more propeller through shafts. Typically, this engine is used on helicopters. The Power generated by the cycle is extracted to power the utility it requires and partly to fuel the compressor. The important parameters are:

- Specific Power $L = \frac{P}{\dot{m}_b}$, how much Power is generated by the engine per Mass Flow Unit;
- Specific Consumption of Power $q_b = \frac{\dot{m}_b}{P}$, how much mass flow of fuel is necessary per Power Unit.

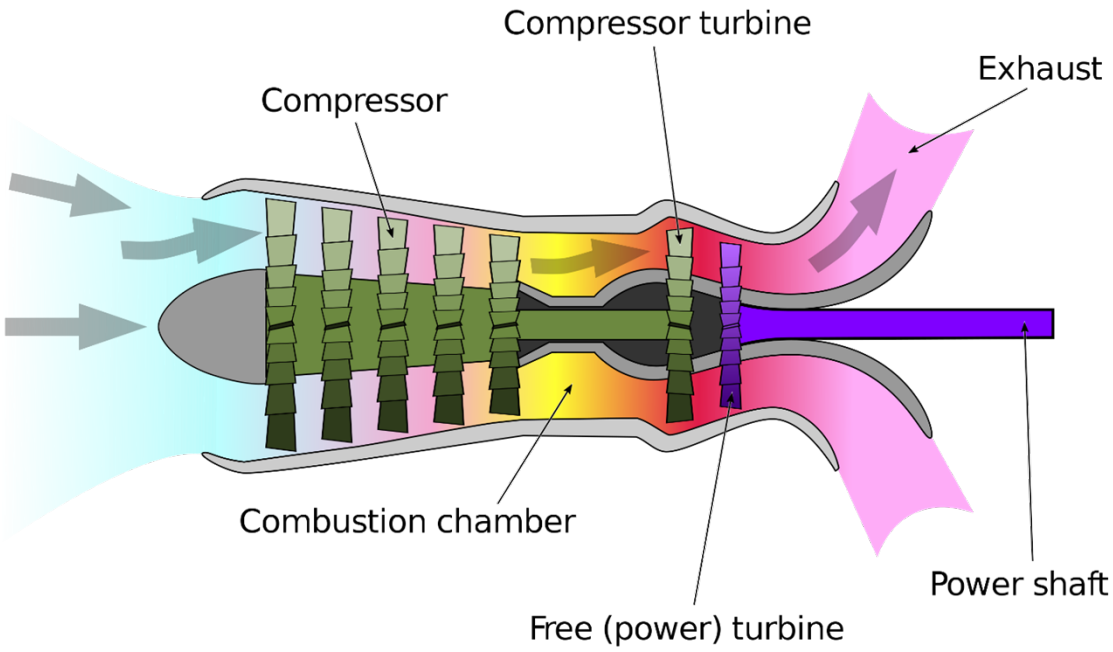

Figure 7: Turboshaft Section
[8]

1.3 ARiAS Project

As written in the abstract, ARiAS (Advanced Research into Aeromechanical Solutions) is a Horizon 2020 funded research project in the field of Aeronautical Engineering and its object is to improve the predictive capability of methods used to analyze aerodynamically induced blade vibrations in aircraft engines. The ARIAS project consortium consists of 19 partners, embracing all major European aircraft engine industries together with the leading universities and research institutes in the field of turbomachinery aeromechanics. [2]

Project structure

The project is structured in different work packages, located in different parts of Europe:

- WP1 = Forced response and Flutter in Compressors (GKN)
- WP2 = Forced response-Flutter interaction in Turbines (ITP)
- WP3 = Flutter in labyrinth seals (RR)
- WP4 = Future enabling technologies (GE Avio)
- WP5 = Communication, exploitation and e-learning (KTH)

- WP6 = Project management and Coordination (KTH)

Objectives
WP1 = generate rig data to validate analysis method in axial compressors.
Different activities were performed as:

- transonic compressor rig tests with aerodynamic/aeromechanical evaluation (TU Darmstad);

- vacuum rotating rig tests of split ring dampers (ECL);

- oscillating transonic compressor cascade rig tests with unsteady pressure evaluations (KTH);

- tests of rotating compressor rotor with controlled excitation amplitude with measurements of aerodynamic damping (Stuttgart);

- analytical studies on unsteady aerodynamics, aeromechanics and friction damping.

WP2 = improving the understanding of non-linear aero-elastic interactions and the effect of mistuning on unstable modes.
Different activities were permormed as:

- design for flutter and forced response interaction and rig adaptation;

- cold flow aeroelastic test in turbine (CTA);

- superimposition of flutter and forced response in spin rig (GE Avio);

- validation/development of simulation technologies.

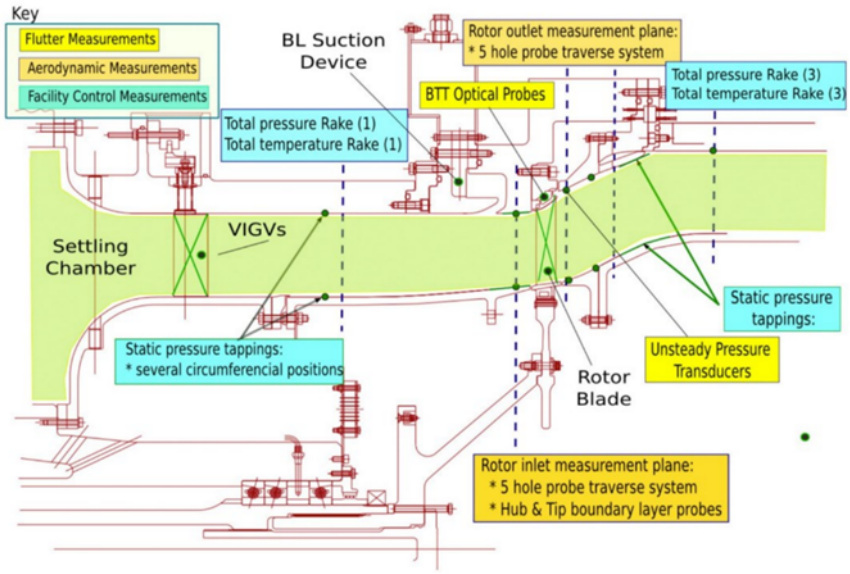

Figure 8: Test rig at CTA

WP3 = understanding the physic of seal flutter. Different activities were performed as:

- design of a static seal rig (Imperial College);
- understand the interdependencies of all design parameters on flutter stability by static rig tests;
- predict seal flutter;
- validation in a full rotating rig (CTA).

WP4 = focusing on developing different areas as:

- innovative methods to assess flutter and forced response;
- new methods to measure aeromechanic vibrations;
- new technologies to mitigate aeromechanic vibrations.

WP5 = preparation of website, data knowledge management and communication materials.

Different Configurations

In order to evaluate the interactions between forced response and flutter, a previous project called FUTURE was modified, including dampers, mistuning masses and magnet

frames.
In the next figure are proposed some configurations usable.

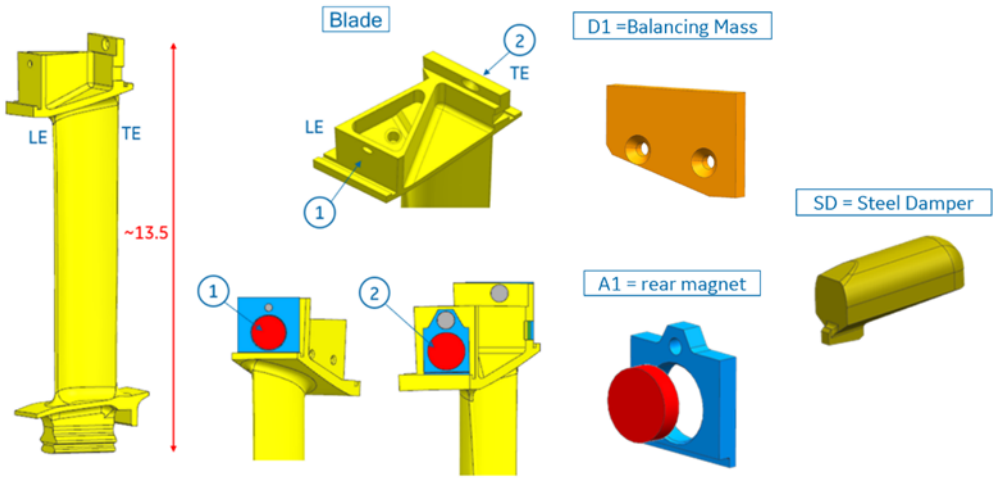

Figure 9: Different Configurations

Afterwards, we will see the configuration chose for the case study of this Thesis Work, that is the one with only the rear magnet.

2 Rotor Dynamics of bladed disk

The Dynamic analysis of bladed disk is the most difficult. These types of analyses are conducted to avoid resonance condition in the operative range of the machine or to control the vibration amplitude with damping.
The dynamic analysis starts with *modal analysis* of the system to identify the natural frequency and the modal shape of vibration. After that, is necessary to evaluate the typical frequencies of the forced vibration and verify the presence of resonances in the operative range and calculate the amplitude response.
All the steps can be done with the assumption based on the structural characteristic of these component, the *Cyclic symmetry*.

2.1 Cyclic Symmetry

Bladed disks are components consisting of identical sectors (at first approximation) and it is possible to analyze only one sector, applying the right boundary conditions on the structure.
Considering a cylindrical coordinates system, with z axis the engine axis of rotation, it is possible to use the same model, in particular a 2 DOF (degrees of freedom), for every sector.

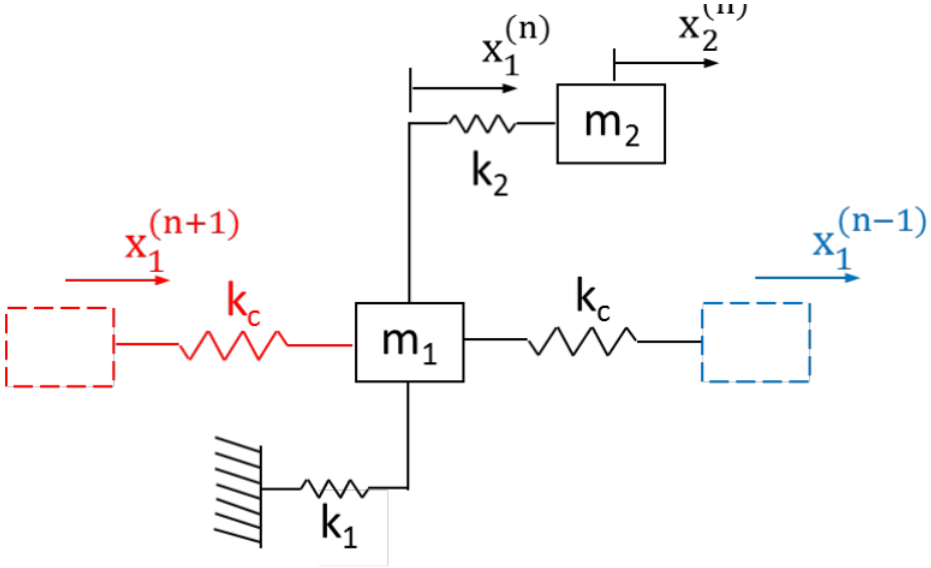

Figure 10: 2 DOF model

The equilibrium equations for the N sector are:

$$\begin{cases} m_1 \ddot{x_1}^{(n)} + k_1 x_1^{(n)} + k_2(x_1^{(n)} - x_2^{(n)}) + k_c(x_1^{(n)} - x_1^{(n+1)}) + k_c(x_1^{(n)} - x_1^{(n-1)}) = 0 \\ m_2 \ddot{x_2}^{(n)} + k_2(x_2^{(n)} - x_1^{(n)}) = 0 \end{cases}$$

The equations can be re-written in matrix form as:

$$[m^{(n)}]\left\{\ddot{x}^{(n)}\right\} + [k^{(n)}]\left\{x^{(n)}\right\} + [k_c^{(n)}]\left\{x^{(n+1)}\right\} + [k_c^{(n)}]\left\{x^{(n-1)}\right\}$$

The equilibrium equations of the whole structure, will have the following form:

$$[M]X + [\ddot{K}]X = 0$$

Since all sectors are the same, the terms of this last equation are:

$$[\mathrm{M}] = \begin{bmatrix} [m] & 0 & \dots & \dots & 0 \\ 0 & \ddots & 0 & \ddots & \dots \\ \vdots & 0 & [m] & 0 & \vdots \\ \vdots & \ddots & 0 & \ddots & 0 \\ 0 & \dots & \dots & 0 & [m] \end{bmatrix}$$

$$[\mathrm{K}] = \begin{bmatrix} [k] & [k_c] & 0 & \dots & \dots & 0 & [k_c] \\ [k_c] & [k] & [k_c] & 0 & \dots & \dots & 0 \\ 0 & \ddots & \ddots & \ddots & \ddots & \ddots & \vdots \\ \vdots & \ddots & [k_c] & [k] & [k_c] & \ddots & \vdots \\ \vdots & \ddots & \ddots & \ddots & \ddots & \ddots & 0 \\ 0 & \dots & \dots & 0 & [k_c] & [k] & [k_c] \\ [k_c] & 0 & \dots & \dots & 0 & [k_c] & [k] \end{bmatrix}$$

$$\{X\} = \begin{Bmatrix} x^{(1)} \\ x^{(2)} \\ \vdots \\ x^{(n)} \\ \vdots \\ x^{(N-1)} \\ x^{(N)} \end{Bmatrix}$$

$$\left\{\ddot{X}\right\} = \begin{Bmatrix} \ddot{x}^{(1)} \\ \ddot{x}^{(2)} \\ \vdots \\ \ddot{x}^{(n)} \\ \vdots \\ \ddot{x}^{(N-1)} \\ \ddot{x}^{(N)} \end{Bmatrix}$$

The only requirement for a solid composed by N equal sector is that the modal shape should be the same also after a rigid rotation of $\frac{2\pi}{N}$ angle, which is the size of a sector. It is useful to define as ϕ the *modal shape*.
There can be three types of modal shape:

a. Equal in every sector $\Phi^{(n)} = \Phi^{(n+1)}$

b. Equal modal shape, but opposite sign, in every sector $\Phi^{(n)} = -\Phi^{(n+1)}$

c. Other mode shapes, obtained with rigid rotation, result as a linear combination of two initial modes Φ and $\hat{\Phi}$ These mode shapes have double multiplicity, meaning that there are pair of modes with the same natural frequency. Among the possible linear combinations, we can also define the complex modes as $\{\theta\} = \{\Phi\} + i\left\{\hat{\Phi}\right\}$ that physically represent a vibration mode in which different points of the system vibrate phase-shifted, one compared to the other. The two mode shapes $\left\{\overline{\Theta}^{+}\right\}$ and $\left\{\overline{\Theta}^{-}\right\}$ are counter rotating waves.

We can define some parameters that can be useful in the following chapters:

- $N\psi = 2\pi h$, where h:*harmonic index*
- $\psi = h\frac{2\pi}{N}$ is the *Inter-Blade Phase Angle* (IBPA)

For the two following case, we have real mode shapes, with phase equal to zero or π.
For $\psi = 0, (h = 0)$ we have a mode shape of type a), in which all the blade sectors move together.
For $\psi = \pi, (h = N/2)$ we have a mode shape of type b), in which the modal shape change sign going from a sector to the other. This mode exists only if N is an even number.
For other values of ψ, we have mode shapes of type c), that represent complex mode shapes.
The real modes associated to complex modes of harmonic index h, have a harmonic trend along the circumferential direction. There will be h number of diametric lines characterized by null displacements, called Nodal Diameters.

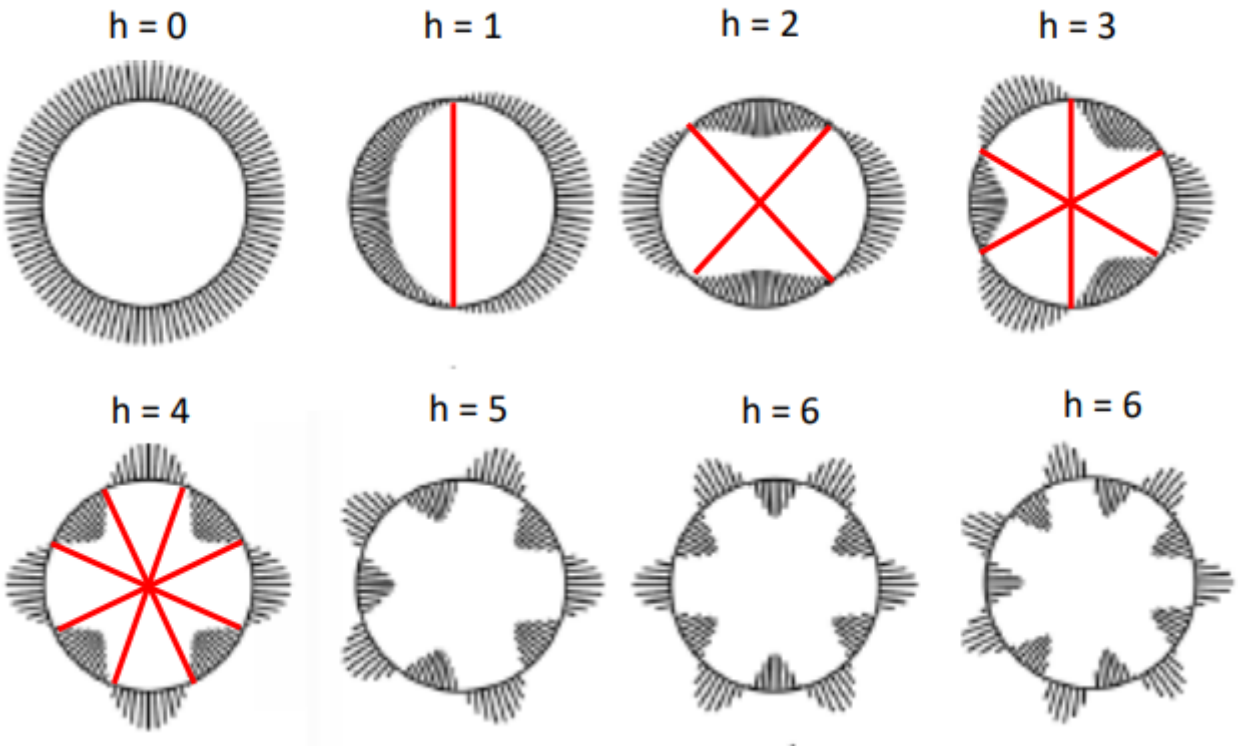

Figure 11: Nodal Diameters

2.2 Modal Analysis

It is possible to use the relationship between the modal displacements of adjacent sectors.

$$\left\{\Theta^{(n)}\right\} = \left\{\Theta^{(n-1)}\right\} e^{ih\frac{2\pi}{N}}$$

to calculate natural frequencies and modal shapes, using the model of the 'fundamental

sector'. Starting from the motion equations of the fundamental sector and substituting $\{x(t)\} = \{x\}\, e^{i\omega t}$, it is possible to obtain:

$$\begin{cases} -\omega^2 m_1 x_1^{(n)} + k_2(x_1^{(n)} - x_2^{(n)}) + k_c(x_1^{(n)} - x_1^{(n+1)}) + k_c(x_1^{(n)} - x_1^{(n-1)}) = 0 \\ -\omega^2 m_2 x_2^{(n)} + k_2(x_2^{(n)} - x_1^{(n)}) = 0 \end{cases}$$

Substituting with the cyclic symmetry relation:

$$x_1^{(n)} = x_1^{(n-1)} e^{(ih\frac{2\pi}{N})} \qquad\qquad x_2^{(n)} = x_1^{(n-1)} e^{(ih\frac{2\pi}{N})}$$

We obtain:

$$\begin{cases} -\omega^2 m_1 x_1^{(n)} + k_1 x_1 + k_2(x_1^{(n)} - x_2^{(n)}) + k_c(x_1^{(n)} - x_1^{(n)} e^{(ih\frac{2\pi}{N})}) + k_c(x_1^{(n)} - x_1^{(n)} e^{(-ih\frac{2\pi}{N})}) = 0 \\ -\omega^2 m_2 x_2^{(n)} + k_2(x_2^{(n)} - x_1^{(n)}) = 0 \end{cases}$$

The equations of the fundamental sector, as the harmonic index h varies:

$$\left(-\omega^2 \left[m_{SC}^{(h)}\right] + \left[k_{SC}^{(h)}\right]\right) \left\{x^{(n)}\right\} = 0$$

It can be used to calculate natural frequencies and modal shapes of the complete system, without solving the complete system. The calculus of modal shapes is limited only to the fundamental sector, that is then expanded with cyclic symmetry:

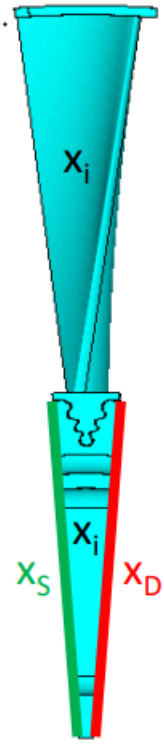

Figure 12: Fundamental Sector

Considering a FEM model for the fundamental sector, the degrees of freedom are:

- internal x_i;
- right interface x_D;
- left interface x_S.

The motion equations are:

$$\left(-\omega^2\left[m^{(n)}\right]+\left[k^{(n)}\right]\right)\left\{x^{(n)}\right\}=0 \qquad \{x\}=\begin{Bmatrix}\bar{x_D}^{(n)}\\ \bar{x_i}^{(n)}\\ \bar{x_S}^{(n)}\end{Bmatrix}$$

Observing that the left interface of n sector fit together with the right interface of n+1 sector, we have:

$$\left(-\omega^2\left[m^{(n)}\right]+\left[k^{(n)}\right]\right)\left\{x^{(n)}\right\}=0 \qquad \{x\}=\begin{Bmatrix}\bar{x_D}^{(n)}\\ \bar{x_i}^{(n)}\\ \bar{x_D}^{(n+1)}\end{Bmatrix}$$

2.3 Forced Response

The results of modal analysis are useful to calculate natural frequencies and mode shapes associated to system. To complete the dynamic analysis, if one or more frequencies are in proximity or in the range of forced frequencies, is necessary to compute the system's forced response.
It is important to remind that we consider a non-axial symmetric pressure field, because inside the engine there are stator sectors upstream and downstream of the rotor sectors. The fundamental sector of a rotor disk with a rotational speed Ω constant, in the pressure field, sees a varying pressure with time and return to the initial value after a complete revolution.
The aerodynamic force has N peaks that correspond to the number of stator sectors.

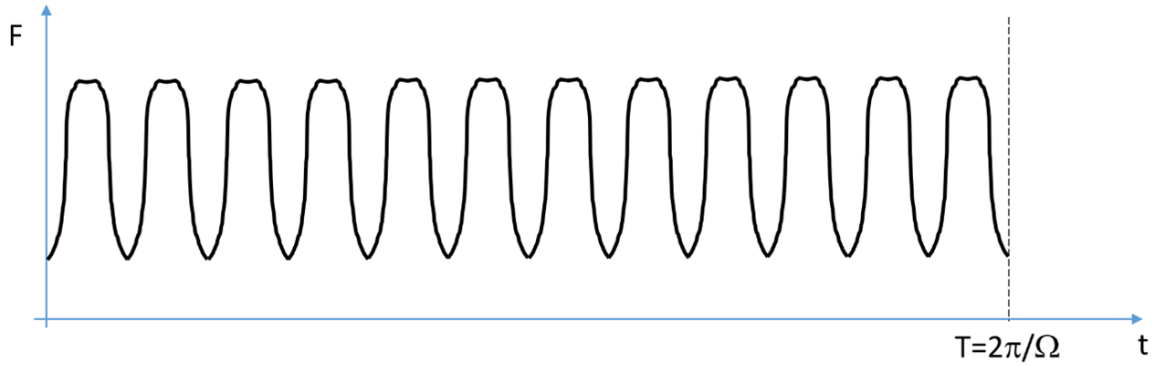

Figure 13: Aerodynamic force

If the pressure field is *stationary*:

- periodic force trend;
- all sectors are stressed in the same way, with a Δt lag between two adjacent sectors.

It is possible to write the aerodynamic force as a Fourier series development, where eo =engine order.

$$F(\alpha) = F_0 + \sum_{eo} F^{(eo)} \cos(eo \cdot \alpha + \delta)$$

where

$$F^{(eo)} = \sqrt{F_c^{(eo)^2} + F_s^{(eo)^2}} \qquad \tan(\delta) = \frac{-F_s^{(eo)}}{F_c^{(eo)}}$$

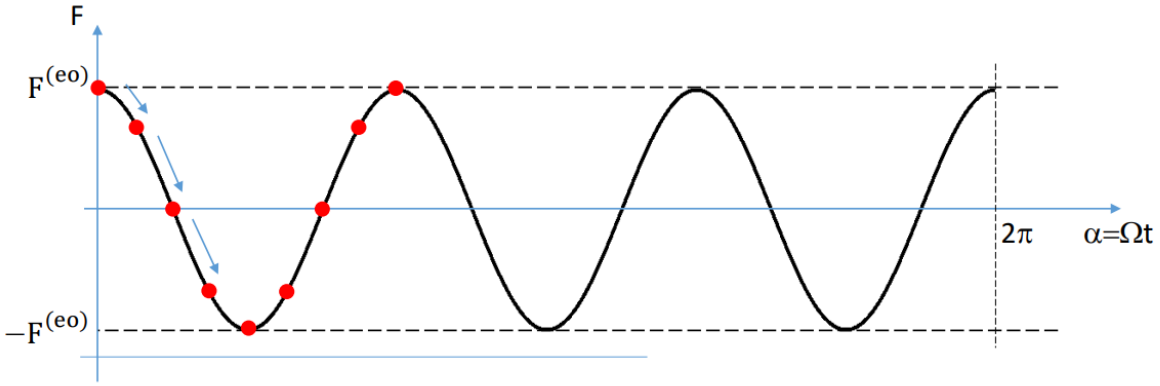

Figure 14: Forced Response

The red dot indicates the position of the nth sector that rotates and is stressed by a Force that depend on time:

$$F^{(n)} = F^{(eo)} \cos(\omega \cdot t + \delta)$$

where $\omega = eo\Omega$.
If we consider two consecutive sectors, which are affected by the same pressure field associated to the eo component of the force:

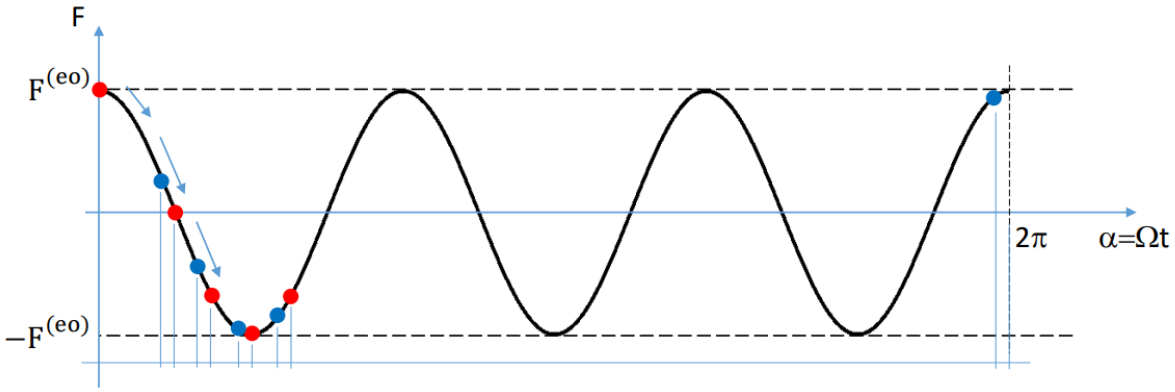

Figure 15: Forced Response of two adjacent sector

The red dot indicates the position of n sector, the blu dot indicates the position of n+1 sector. The lag between the two sectors is given by the following equation:

$$\Delta t = \frac{2\pi}{\Omega N}$$

The forces acting on two adjacent sector are:

$$F^{(n)} = F^{(eo)} \cos(\omega t - \Psi + \delta)$$

In presence of engine order eo, forces of two consecutive sectors are phase lagged of $\Psi = eo\frac{2\pi}{N}$ angle.
To evaluate operative range for possible resonances, it can be useful a graphical representation as the Campbell Diagram.

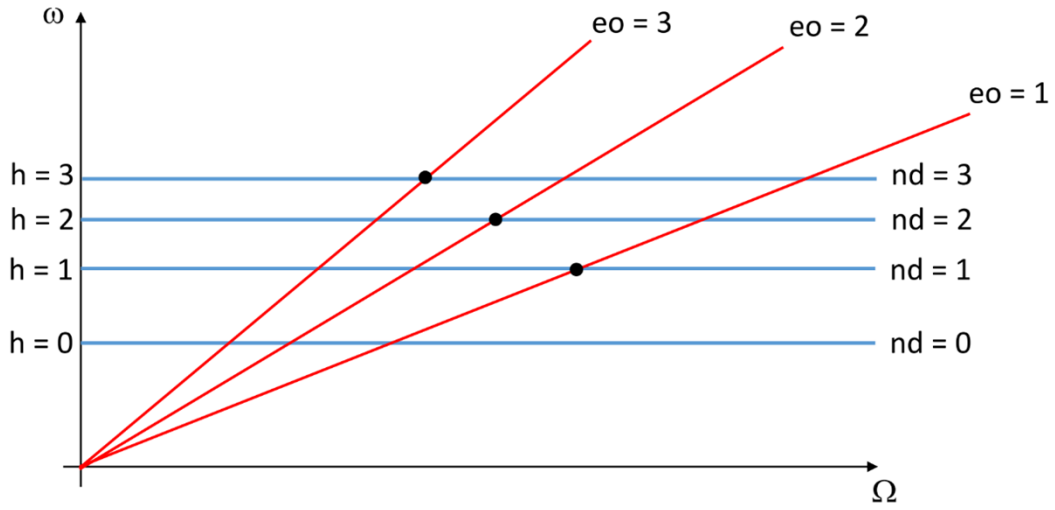

Figure 16: Campbell Diagram

The blue lines represent the natural frequencies, and the red lines are the forced response frequencies in function of the rotational speed of the system ($\omega = eo * \Omega$). The intersections seen in the graphic can be possible resonance points. For resonance behavior, are necessary the following conditions:

- $\omega = \omega_n$;
- $f_n = \{\Phi\}_n^T F \neq 0$, the projection of force vector associated with given engine order on the generic mode is different from zero.

The harmonic index **h** can assume value between 0 and N-1.
The forces can exist also for **engine order** larger than N-1.

$$\sum_{n=0}^{N-1} e^{inh\frac{2\pi}{N}} e^{-ineo\frac{2\pi}{N}}$$

substituting $eo = kN + eo'$ with $0 < eo' < N$, the final equation is:

$$\sum_{n=0}^{N-1} e^{inh\frac{2\pi}{N}} e^{-in(eo')\frac{2\pi}{N}}$$

So the resonance condition verifies when:

$$eo' = eo - kN = h$$

It is possible to represent on graphics the last relationship, with the so called *Zig-Zag Diagram*.

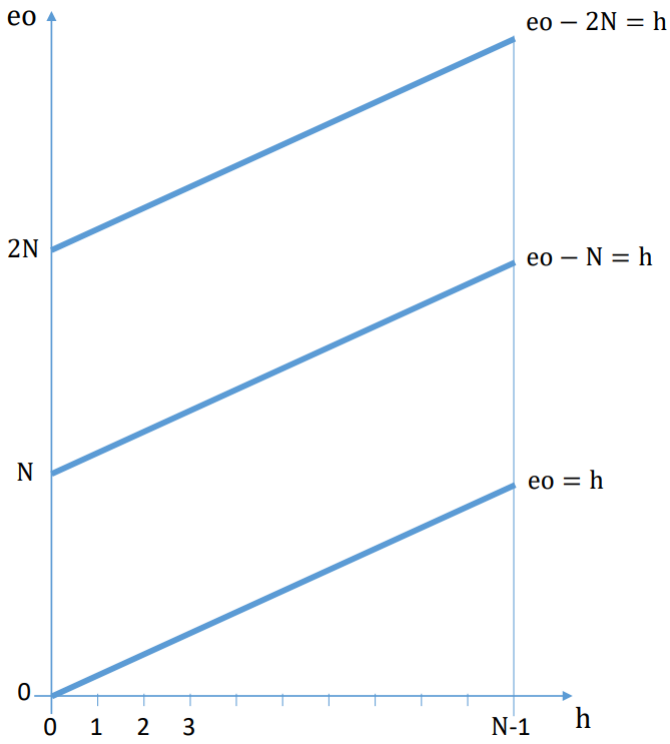

Figure 17: Example of Zig-Zag Diagram

The lines that represent the relationship $eo - kN = h$ are parallels, with an angle of 45° and intercept the ordinate axis at kN values.
It is important to remember that modeshapes with harmonic index $h > \frac{N}{2}$ are identical to the ones having $0 < h < \frac{N}{2}$. [13]

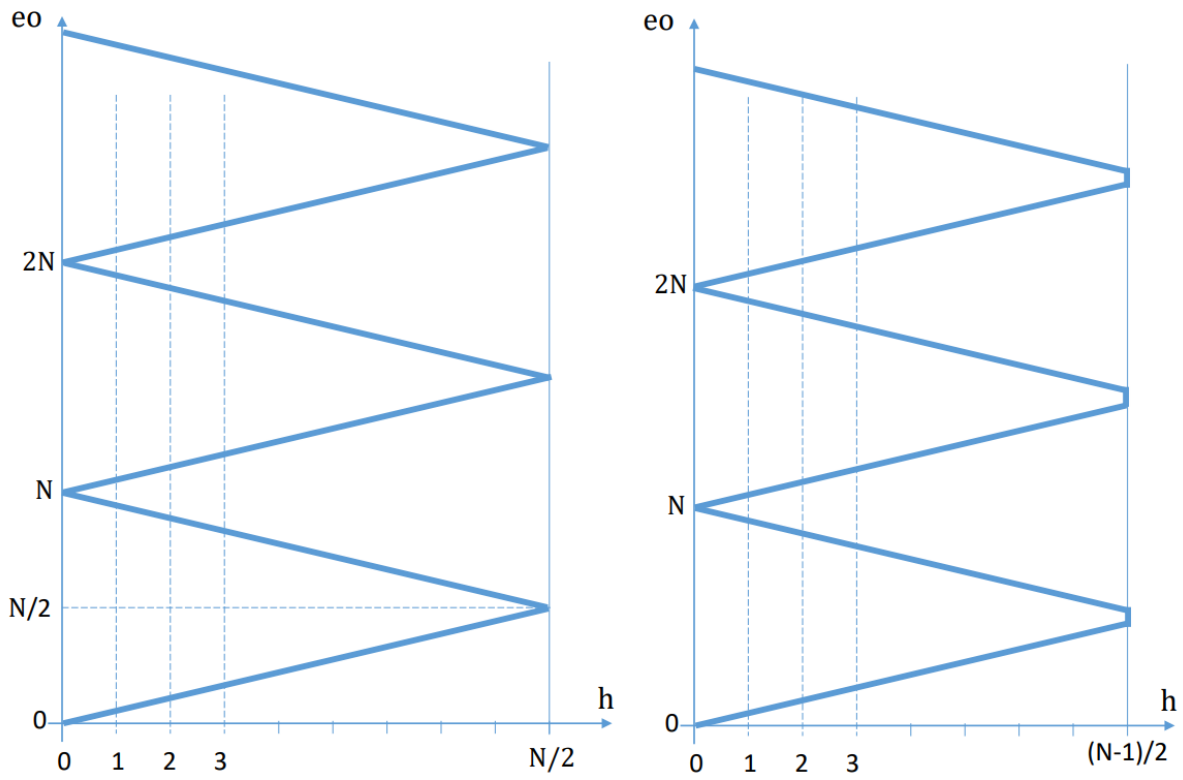

Figure 18: Zig-Zag Diagram N even (left) vs. N odd (right)

3 Aeroelasticity

The Aeromechanics studies the interaction of elastic body with fluid flow to evaluate the static vibrations that can lead to failure.
The Aeroelasticity is the branch of physics and engineering that studies the interaction between: Inertial forces, Elastic forces, and Aerodynamic forces.

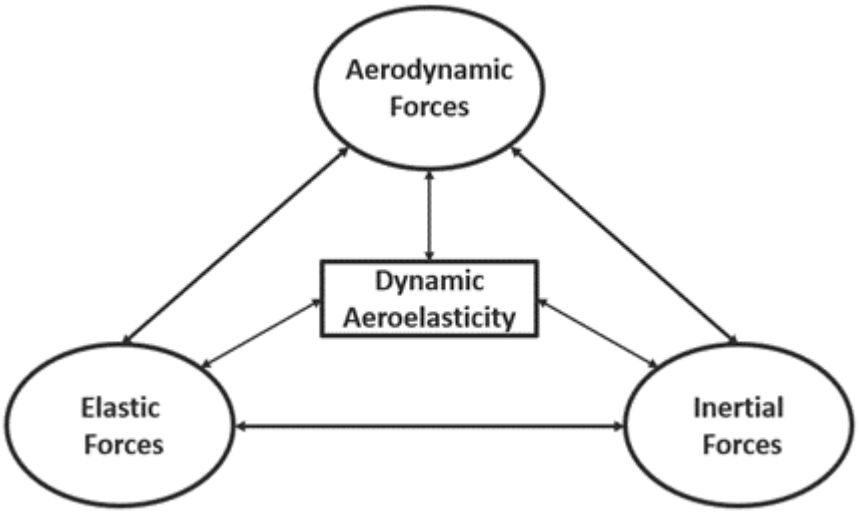

Figure 19: Collar Diagram

- **Structural Dynamics** = Elastic forces + Inertial forces
- **Flight Mechanics** = Inertial forces + Aerodynamic forces
- **Static Aeroelasticity** = Aerodynamic forces + Elastic forces
- **Dynamic Aeroelasticity** = Inertial forces + Elastic forces + Aerodynamic forces

The study of aeroelasticity can be classified in:

- ***Static aeroelasticity*** dealing with static response of an elastic body to a fluid flow.
- ***Dynamic aeroelasticity*** dealing with body's dynamic response.

Following problems detected in gas turbines, the study of aeroelasticity in axial turbomachines has been developed. It was important to: reduce the weight of blade, raise performance and efficiency of compressor blades with high aspect ratio airfoils. High by pass ratio turbofan were interested by induced vibration problems due to flow, and so it

was necessary the introduction of damper like dry friction and under platform damper to prevent high cycle fatigue failures.

Aeroelastic problems are important from the point of view of reliability flight safety and operating cost. The certifications of turbomachinery requires certain limits on maximum bearable stresses for the different components. To avoid vibration issues, it is needed an aeromechanical analysis, to verify that the structure examined didn't reach failures caused by High Cycle Fatigue (HCF) phenomenon. Since turbomachinery blades have become lighter and slender, and they also have high aspect ratio (is given by the radial length of the blade over the axial chord), they turned out to be the more critical components subject to vibration issues.

It is possible to visualize the Aeromechanical problems on the following Campbell Diagram, where there are represented the natural frequencies (red lines) of the blades and the lines with slope called the engine orders.

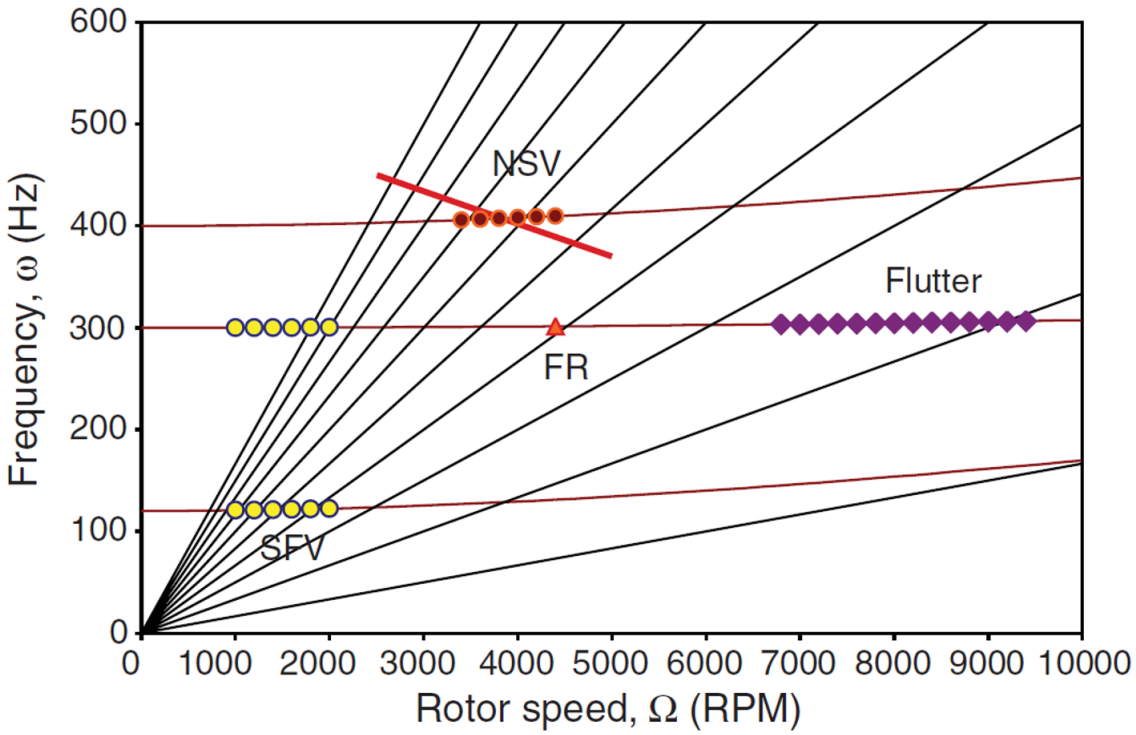

Figure 20: Campbell Diagram with aeromechanical problems

Forced Response (FR)

At campbell crossing. The vibrations are caused by external forces, for example upstream blade wake or potential field from a downstream row. The highest vibration response is at resonance condition, with the excitation frequency is equal to natural frequency of component.

Non-synchronous vibration (NSV)

At low speed off design conditions. Flow instability can occur in high by pass ratio turbofan, where there are higher mass flow in inlet in the compressor. These type of vibrations are caused by instability phenomena in the flow at the leading edge of the blade (vortex shedding, instantaneous unsteady flow separations and tip clearence flows) and resemble the rotating stall. The propagation direction is opposite to the rotating speed.

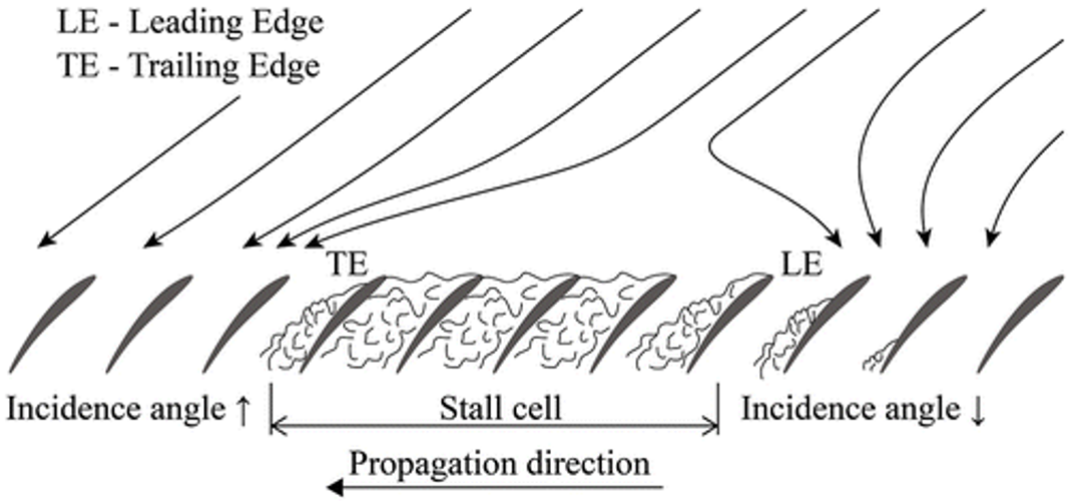

Figure 21: Non-synchronous vibrations

Separated Flow Vibration (SFV)

Chaotic buffeting of the blade. These vibrations are driven by unsteadiness originating from flow, but with different frequencies and phases, resulting as a chaotic buffeting of blades that cannot be solved with RANS equations.

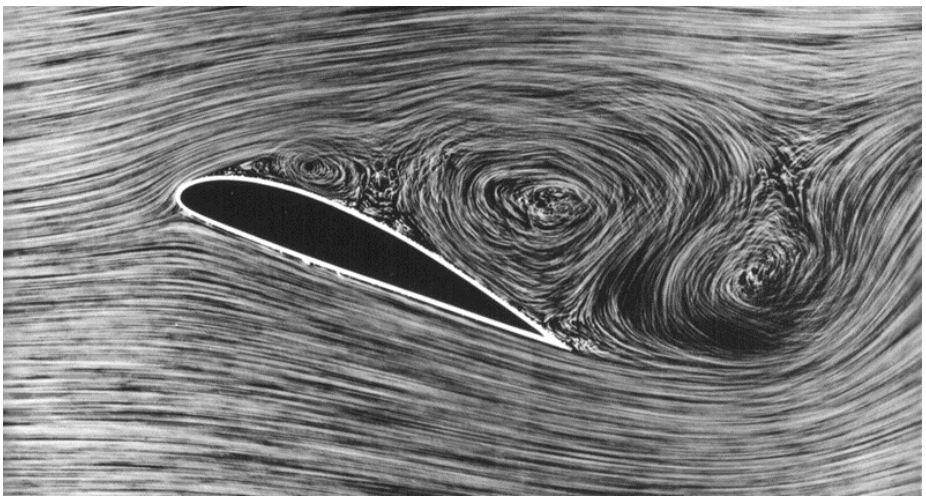

Figure 22: Separated flow vibrations

Flutter

It happens at low natural frequency and high rotational speed. It is an Aeroelastic stability problem, where the influence of adjacent blades plays an important role; in fact, when the blade oscillates, the load changes. It is a vibrational phenomenon where aerodynamic, inertial, and elastic forces are combined, generating a critical response of the mechanical system.

It is an **auto-excited** and **self-sustained** vibration, where the aerodynamic forces acting on an object coupled with the structure's natural mode of vibration, produce rapid periodic movements.

A vibrating body immersed in a flow can extract energy from the flow to increase its mechanical energy. This matches with a negative damping, especially the amplitude of vibration growth exponentially.

In presence of flutter, the surface pressure oscillation can feed energy into the oscillation and the vibration amplitude can grow up to a limit cycle. Otherwise the vibration is damped. Limit cycle oscillation can occur due to non linear effect. It is a non predictable event.

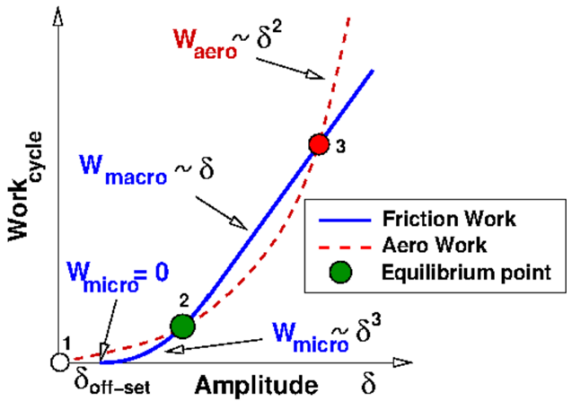

Figure 23: Work cycle and Amplitude

In the previous figure is rapresented the Work per cycle related to the vibration amplitude.
The blue curve represents the Friction Work, the red one is the Aero Work and the green circle is the Equilibrium point.

If the aerodynamic damping is >0, flutter phenomenon will never occurs.
If the aerodynamic damping is <0, the aerodynamic work is positive and follows a parabolic trend ($W_{aero} = \delta^2$).
If there was no mechanical damping, the flutter would cause the blade to grow in amplitude exponentially, with the aerodynamic work always greater then damping work. The limit cycle verifies when there is the equilibrium condition, and despite perturbation, the system will return always at the equilibrium point.

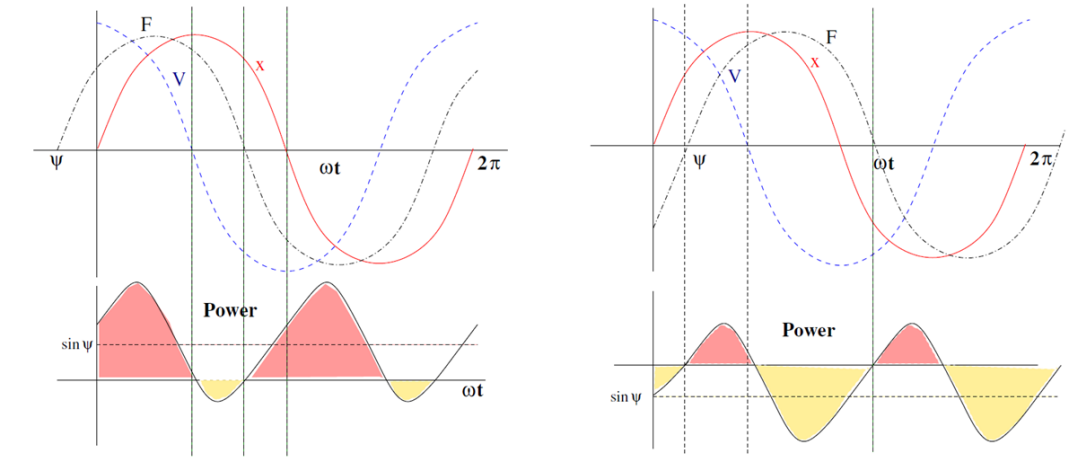

Figure 24: Force Lead and Force Lag

The Work Cycle depends on phase existing between the blade displacement (blade oscillation) and the response under pressure (induced pressure).
As visible in the previous graphics, force and displacement are in quadrature: [16]

- Force Lead = force anticipates the displacement, and provides energy to the structure that absorbs energy;
- Force Lag = displacement anticipates the force, the structure releases energy.

3.1 Flutter Classification

The Flutter can be classified as:

- **Classical flutter**= without separation, due to the phase lag between blade vibration and induced forces.
- **Coalescence flutter**= classical flutter while two natural frequencies are merging, there can be veering zone where the modal shape change at similar frequency.
- **Single degree of freedom flutter**= involves a single vibration mode.
- **Stall flutter**= near stall line, but the flow over the airfoil can be separated and not stalled yet. Often seen in fans and front compressor stages, it may occur at low rotor speeds.
- **Dynamic stall flutter**= blade row stalled only in a part of the vibration cycle.
- **Choke flutter**= near choking conditions, it may occur for pressure ratios below the nominal operating line when a shock wave occurs. It is less common nowadays because blade have now a low aspect ratio.
- **Supersonic unstalled flutter**= classical flutter but in supersonic conditions. It is very dangerous because it can appear during the most critical parts of the flight envelope (take-off, climb). It represents a strong instability that can occurs when large fan rotors operate at supersonic tip Mach numbers. Nowadays, commercial fans that tend to be shroudless, may encounter *stall flutter*. [16]

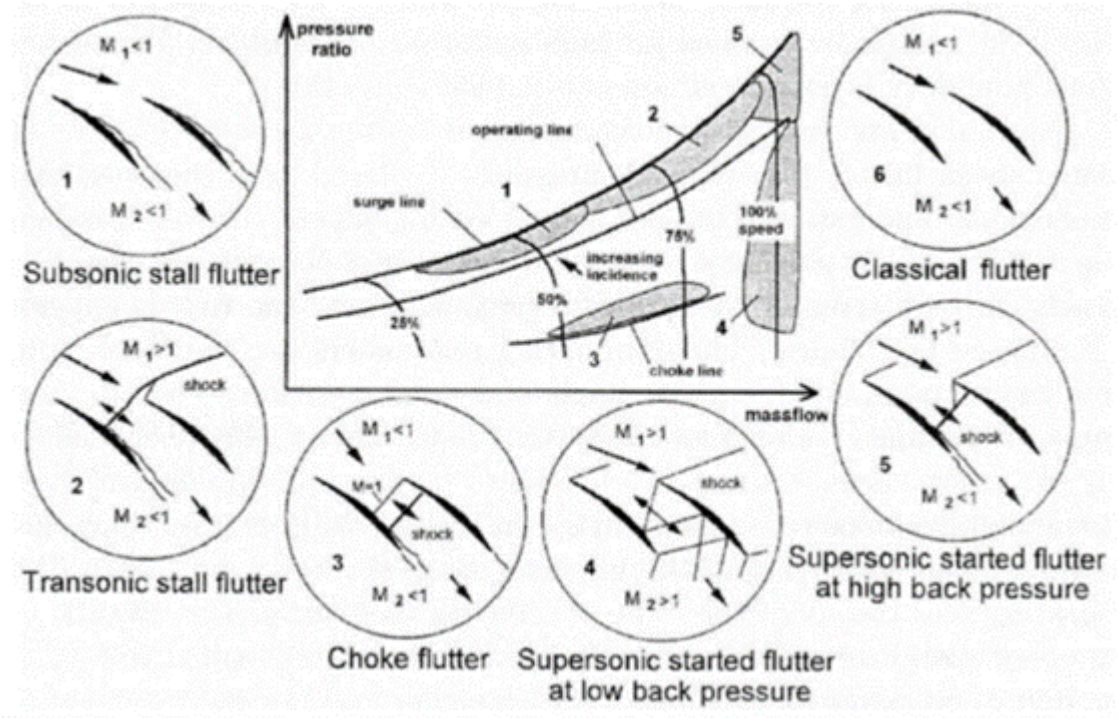

Figure 25: Flutter Classification

3.2 Flutter stability

In this section we are going to see the main aspect that can influence the stability of the structure if the flutter phenomenon verifies. If we are in limit cycle condition, there is an equilibrium between aerodynamic damping and structural damping. Otherwise we aren't at equilibrium condition, the damping growth is exponential and lead to a vibration amplitude that always grow.The aerodynamic damping has a stabilizing effect if positive.

$$(work)_{aerodynamic-damping} = -(work)_{structural-damping}$$

It is important to understand the particular conditions that can simplify the manifestation of flutter phenomenon. Let's define the characteristic parameters: [16]

- **Reduced Velocity**: $V_{reduced} = \frac{V_{in}}{\omega b}$, where V_{in} is the inlet velocity, ω is the blade frequency, and b is the chord or semi chord. If the reduced velocity increases, the risk of flutter rises. If the frequency ω decreases, the reduced velocity increases. If the chord or semi chord b decreases, the reduced velocity increases. The reduced frequency is the inverse of reduced velocity.

- **Mach Number**: important parameter, especially if we are in presence of super-

sonic flow.

- **Blade Load**: it depends on blade shape and from the distribution of aerodynamic static load on blade. A higher blade load involves operative points at high energetic exchange. If blade load parameter increases, the reduced velocity decreases.

- **Pressure and Density**: If gas density increases, it has a stabilizing effect on blade if the aerodamping is >0.

- **Modeshapes**: low frequencies are the most critical but is important also to take a look to the shape, to the center of torsion and the angle.

- The most important parameter to look at for measuring the flutter occurence is the **Aerodynamic Damping Coefficient** computed as:

$$\xi_a = \frac{-L}{8\pi E}$$

where L is the aerodynamic work computed by the following equation:

$$L = \int_t^{t+T} \int_\Sigma (-p)\overline{N} \cdot \overline{c_{blade}} d\Sigma dt$$

3.3 Flutter methods

The methods existing for measuring the flutter phenomenon must be unsteady techniques and can be: Coupled or Uncoupled.
It is important to solve the Navier-Stokes equations with different methods as Time-Linearized (LARS) or Nonlinear time integration (TRAF). Mesh deformation strategies can also be applied in order to adapt in the best way possible, the mesh to the real solution.

Coupled method

This method solves at the same time the unsteady CFD analysis and the dynamic analisys, evaluating the solid and fluid interaction respectively.

Uncoupled methods

This method solves the Unsteady CFD analysis generated by a vibrating row at constant amplitude; the displacements obtained from a previous FEM modal analysis are imposed as vibrating grid. The influence of the solid on the fluid is evaluated.
The aerodynamic work is computed through an energy method and is related to the aerodynamic damping:

- positive aerodamping= NO FLUTTER, stable system, the energy goes from solid to fluid;

- negative aerodamping= FLUTTER, unstable system, the energy goes from fluid to solid.

[16]

4 Computational Fluid Dynamics

The fluid is governed by three *Conservation Principles*:

- Mass
- Momentum
- Energy

The state of the system is known when the thermodynamic state and field vector velocity are known. Applying these three Principles to a control volume, it is possible to obtain the *Governing Equations*, also called *Navier-Stokes Equations*.
First of all, we should clarify the two points of view for the fluid particle:

- Eulerian: the control volume is fixed in space, the behaviour of the fluid is studied in a defined zone;
- Lagrangian: the control volume is moving, the evolution of set of particle is studied.

4.1 Governing Equations

4.1.1 Conservation of Mass

Considering a finite volume V, fixed in the space, delimited by a surface S, the principle of mass conservation prescribes that:
"The temporal variation of mass should be balanced by the net flux through the surface and by any source terms."
Conservative Integral Form:

$$\frac{\partial}{\partial t}\int_V \rho dV = -\int_S \rho\overline{q}\cdot\overline{n}dS + Sources$$

Conservative Differential Form:

$$\frac{\partial\rho}{\partial t} + \nabla\cdot(\rho\overline{q}) = 0$$

Non-Conservative Differential Form:

$$\frac{D\rho}{Dt} + \rho\nabla\cdot\overline{q} = 0$$

4.1.2 Conservation of Momentum

The momentum balance equation prescribes that: *"Changes in momentum with time are due to the net flow through S and any source terms".*

Momentum is defined as the product of mass and velocity.

$$\frac{\partial}{\partial t}\int_V \rho\overline{q}dV = -\int_S \overline{q}\left(\rho\overline{q}\cdot\overline{n}\right)dS + Sources$$

The sources can be:

- Volume Forces: centrifugal, electromagnetic...

$$\int_V \rho\overline{f_e}dV$$

- Surface Forces: developed through surface, can be an exchange of forces in the fluid flux.

  - Real Fluid: $\overline{\sigma}_n = -p\overline{n} + \overline{\tau_n}$, anisotropic pressure;

  - Ideal Fluid: $\overline{\sigma}_n = -p\overline{n}$, isotropic pressure;

It is now possible to write the Conservative Integral Form:

$$\frac{\partial}{\partial t}\int_V \rho\overline{q}dV = \int_S \overline{q}\left(\rho\overline{q}\cdot\overline{n}\right)dS + \int_S \overline{\overline{\sigma}}\cdot\overline{n}dS + \int_V \rho\overline{f_e}dV$$

Conservative Differential Form:

$$\frac{\partial(\rho\overline{q})}{\partial t} = -\nabla\cdot(\rho\overline{q}\overline{q}) + \nabla\cdot\overline{\overline{\sigma}} + \rho\overline{f_e}$$

Non-Conservative Differential Form:

$$\rho\frac{D\overline{q}}{Dt} = \nabla\cdot\overline{\overline{\sigma}} + \rho\overline{f_e}$$

4.1.3 Conservation of Energy

The energy of the system can vary as a result of the exchanges of energy itself due to the work and heat exchanged with the outside.

$$E = e + \frac{q^2}{2}$$

where

- E: total energy;
- e: internal energy, linked to molecular motion;
- $\frac{q^2}{2}$: kinetical energy, mean particle motion.

The Conservative Integral Form is:

$$\frac{\partial}{\partial t}\int_V \rho E dV = -\int_S \rho E\overline{q}\cdot\overline{n}dS + \int_S (\overline{\overline{\sigma}}\cdot\overline{n})\cdot\overline{q}dS + \int_V \rho\overline{f_e}\cdot\overline{q}dV - \int_S \overline{q_T}\cdot\overline{n}dS$$

Conservative Differential Form:

$$\frac{\partial \rho E}{\partial t} + \nabla\cdot(\rho E\overline{q}) = \nabla\cdot(\overline{\overline{\sigma}}\cdot\overline{q}) + \rho\overline{f_e}\cdot\overline{q} - \nabla\cdot\overline{q_T}$$

Non-Conservative Differential Form:

$$\rho\frac{DE}{Dt} = \nabla\cdot(\overline{\overline{\sigma}}\cdot\overline{q}) + \rho\overline{f_e}\cdot\overline{q} - \nabla\cdot\overline{q_T}$$

4.1.4 Navier-Stokes for Compressible Fluxes

The Conservative Differential equation, valid for laminar and tubrulent fluxes are:

$$\begin{cases} \frac{\partial\rho}{\partial t} + \nabla\cdot(\rho\overline{q}) = 0 \\ \frac{\partial\rho\overline{q}}{\partial t} + \nabla\cdot(\rho\overline{q}\overline{q}) = -\nabla P + \nabla\cdot\overline{\overline{\tau}} + \rho\overline{f_e} = 0 \\ \frac{\partial\rho E}{\partial t} + \nabla\cdot(\rho\overline{q}E) = -\nabla\cdot(P\overline{q}) + \nabla\cdot(\overline{\overline{\tau}}\cdot\overline{q}) + \rho\overline{f_e}\cdot\overline{q} + \nabla\cdot(k\nabla T) \end{cases}$$

4.2 Discretization Methods

In Bibliography exist a lot of methods to discretize a domain, especially:

1. Finite Differences: need structured grids, not suitable for complicate geometries;
2. Finite Volumes: cell integration, valid for structured and unstructured grids;
3. Finite Elements: continuous and discontinuous domains, regard complex geometries and elevated graded of approximation.

Structured grid= this grid type cannot be used to discretize complex geometry and is characterized by a number of indices coherent with the domain dimension (for example 2D: i,j; 3D: i,j,k).
Unstrictured grid= this grid type can be used to discretize complex geometry and is characterized by only one index (more complex, there is no link between the index number and the space direction). The three main characteristics are:

- Convergence: when conservation equations are verified with a certain range of tolerance, there is no more changes in the solution adding more time steps.

- Consistency: when the local truncation error tends to zero, when Δt and Δx tend to zero.

- Stability: ability of the scheme to not amplify the error over time steps. It is studied by Taylor expansion in series.

4.2.1 Finite Volumes

Let's take a closer look at this method, that is the most used in CFD and consists of a volume integration in order to solve one of the main problems of this subject: *Computation of flux value exchanged at cell interfaces.*
It is necessary to guarantee the conservativeness, that means that what exits one cell, enter totally the subsequent one. There are different methods that can be used to compute the convective flux:

- **First order upwind** : simple implementation, the value of cell's center is considered;

- **Central Difference Scheme** : more accurate than first order upwind, but can generate some oscillations in the solution and that's why we need to introduce the dissipation factor that damps these oscillations; the interface value is calculated by a linear interpolation of the value on the left and on the right side of the interface to compute;

- **Power Law Scheme** : a better interpolation is used, to obtain a more accurate value; [16]

- **Second Order Upwind** : two cells values are taken upstream, with two linear extrapolation; it can be a problem when a non-linear phenomena as shock/expansion waves may be present.

- **Quick Scheme** : quadratic upwind interpolation for convective kinetics, two upstream nodes and one downstream. this is a very accurate scheme, but if we are in presence of high gradients, the stability is limited.

It can be useful to remember that more accurate means less stability, stiff calculus that is difficult to reach convergence, because of the high computational cost.
In particulat, for First order upwind scheme we can talk about *false numerical diffusion* that can be related to grid refinement.
In fact, if we have a coarse grid, it can be seen a diffusion on a big part of the domain.

Finite Volumes methods divide also in:

- **Pressure-based** : incompressible flow, density constant and not linked to the pressure;
- **Density-based** : compressible flow, the continuity equation is used to compute density, temperature is computed form the enthalpy equation and then is computed the pressure from the equation of state. [15]

4.3 Turbulent Flow

For low number of Reynolds flows are laminar, for high value of Reynold flows are turbulent. Turbulent flows are:

- **Chaotic** : irregularity ad randomness, statistical approach, turbulent flows are always chaotic, but not all chaotic flows are turbulent;
- **Diffusive** : rapid mixing, thermal, momentum and mass exchanges are rapid;
- **Dissipative** : energy decay, flux is laminar if there is no energy supply;
- **Rotational** : vortex presence is crucial.

The domain dimension is proportional to the characteristic length of the body study case and big vortex.
The cell dimension is proportional to small eddy dimension.
Turbulent flow simulation can be made, written in order of increasing accuracy, with:

- **RANS:** Reynolds Averaged Navier Stokes;
- **LES:** Large Eddy Simulation;
- **DNS:** Direct Numerical Simulation

Let's see some difference in the following picture:

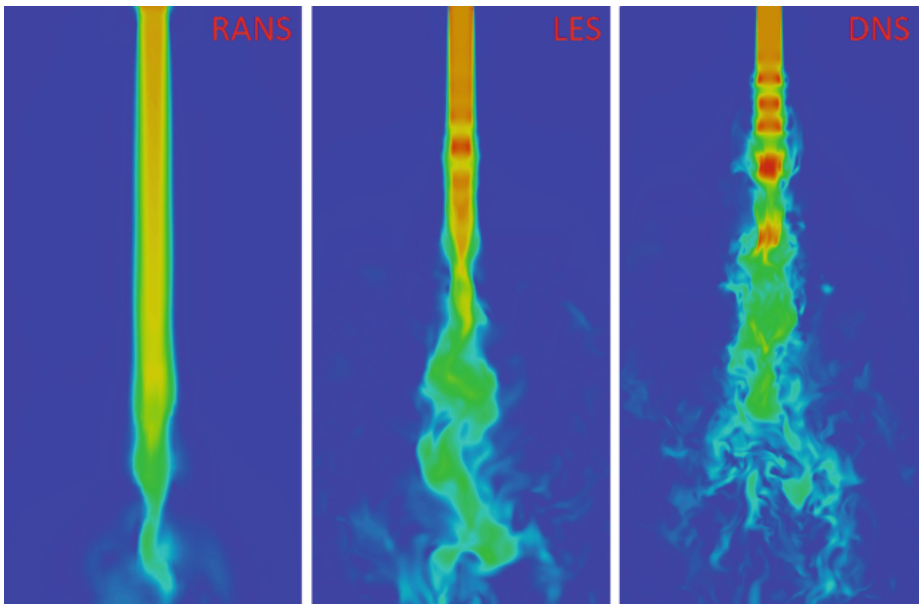

Figure 26: Different simulation accuracy
[9]

In the following picture, is represented the link between the eddy dimension and the type of simulation used:

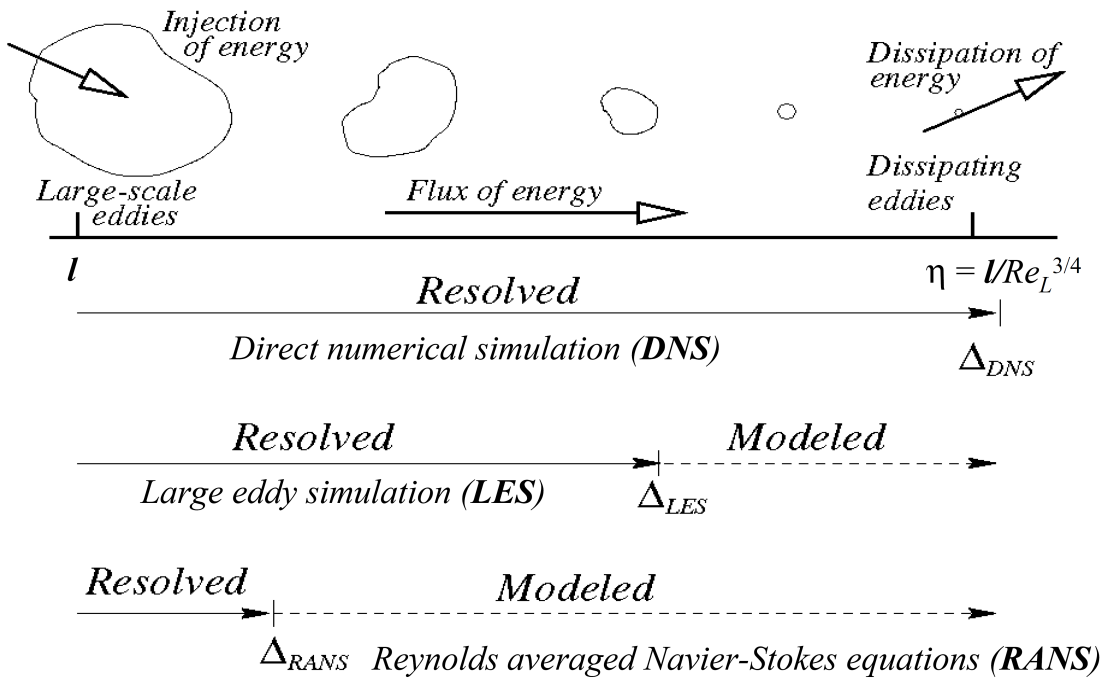

Figure 27: Numerical Modelling
[10]

DNS The grid should be sufficiently refined, because it is a direct simulation with the purpose to solve every eddies, also the smallest one. The computational cost is high, proportional to Re^3 and the number of points that are contained in the grid are proportional to $Re^{9/4}$. A reverse inertial cascade occurs, the eddies that separate from the body are small and moving away they became bigger.

LES This type of simulation solves only the big scale, till the cell dimension; the eddies smaller than the cell dimension are being solved through a universal model. With this method is mentioned also the presence of space filter, relatable to the cell dimension.

RANS The RANS are Navier-Stokes time-averaged equations. In order to compute turbulent flows, a time-averaged flow field solver is implemented . The velocity (and the other conservative variables) are decomposed as follows:

$$U_i(t) = U_i + u_i(t)$$

where U_i indicates the mean velocity independent from time and $u_i(t)$ represents the fluctuating part of velocity dependent from time.

We write the RANS for incompressible flows:

$$\begin{cases} \dfrac{\partial q_i}{\partial x_i} = 0 \\ \rho \dfrac{\partial q_i}{\partial t} + \rho q_j \dfrac{\partial q_i}{\partial x_j} = -\dfrac{\partial P}{\partial x_i} + \dfrac{\partial \tau_{ij}}{\partial x_j} \end{cases}$$

Applying the Reynolds decomposition:

$$q_i = \overline{q_i} + q_i' \quad P = \overline{P} + P'$$

We obtain:

$$\begin{cases} \dfrac{\partial \overline{q_i}}{\partial x_i} = 0 \\ \rho \dfrac{\partial \overline{q_i}}{\partial t} + \rho \overline{q_j} \dfrac{\partial \overline{q_i}}{\partial x_j} = -\dfrac{\partial \overline{P}}{\partial x_i} + \dfrac{\partial \tau_{ij}}{\partial x_j} - \rho \overline{q_j'} \dfrac{\partial \overline{q_i'}}{\partial x_j} \end{cases}$$

The additional term $-\rho \overline{q_j'} \frac{\partial \overline{q_i'}}{\partial x_j}$ represent the effects of fluctuations on the scales that we are not solving and contains the *additional stress tensor*. It is possible to rewrite once again the equations, after further calculus on this additional term.

$$\begin{cases} \frac{\partial \overline{q_i}}{\partial x_i} = 0 \\ \rho \frac{\partial \overline{q_i}}{\partial t} + \rho \overline{q_j} \frac{\partial \overline{q_i}}{\partial x_j} = -\frac{\partial \overline{P}}{\partial x_i} + \frac{\partial}{\partial x_j}(\overline{\tau}_{ij} + \tau_{ij}^R) \end{cases}$$

where $\tau_{ij}^R = -\rho \overline{q_i' q_j'}$ are called the Reynolds stresses and they are larger than viscous stresses, that represent the effects of turbulent fluctuations on mean flow.

$$\boldsymbol{\tau} = \begin{pmatrix} \tau_{xx} & \tau_{xy} & \tau_{xz} \\ \tau_{yx} & \tau_{yy} & \tau_{yz} \\ \tau_{zx} & \tau_{zy} & \tau_{zz} \end{pmatrix} = \begin{pmatrix} -\rho \overline{u'^2} & -\rho \overline{u'v'} & -\rho \overline{u'w'} \\ -\rho \overline{u'v'} & -\rho \overline{v'^2} & -\rho \overline{v'w'} \\ -\rho \overline{u'w'} & -\rho \overline{v'w'} & -\rho \overline{w'^2} \end{pmatrix}$$

Figure 28: Reynolds stress tensor

The normal stresses are always $\neq 0$ because they contain squared velocity fluctuations. The tensor is symmetric so the time averaged equations contain six additional unknowns in the momentum equations. [15]

4.4 Closure Turbulence Model

The main task of turbulence modeling is to develop computational procedures of sufficient accuracy for engineers to be able to predict the Reynolds stresses and the Scalar Transport Terms.
This will then allow the computation of time-averaged flows and scalar fields without having to calculate the actual flow fields over long time periods.
It is necessary to find a mathematical formulation for the stress tensor of Reynolds. This problem originates the closure problem, and is necessary to define which mathematical model is being used in every simulations that we are going to do.
In the following paragraphs are described the turbulence models that have been used for the sensitivity analysis.

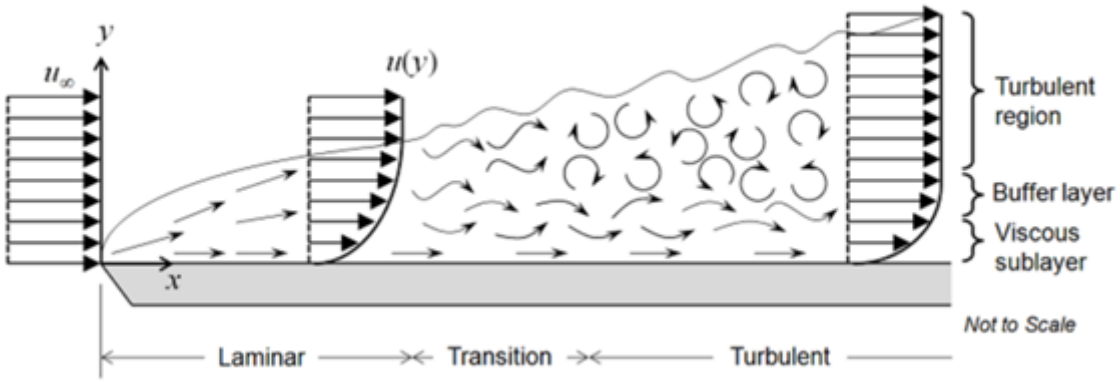

Figure 29: Boundary Layer
[12]

With the term *eddy* is intended the swirling of a fluid and the reverse current created when the fluid is in a turbulent flow regime. The *Eddy viscosity* μ_t is a factor for turbulent transfer of energy because of moving eddies and describes the turbulent flow next to a solid wall.

4.4.1 Baldwin-Lomax Model

It's a two-layer algebraic model [[17]], the eddy viscosity is computed as:

$$\mu_t = \begin{cases} \mu_i, y \leq y_{crossover} \\ \mu_o, y > y_{crossover} \end{cases}$$

where y is the distance normal to the wall and $y_{crossover}$ is the minimum value of y for which $\mu_t = \mu_o$.

- In the inner region the Prandtl- Van Driest formula is used:

  $$\mu_i = \rho l^2 |\omega|$$

  where $|\omega|$ is the vorticity magnitude, l is the mixing length, D is the van Driest damping factor:

  $$D = 1 - e^{\frac{-y^+}{A^+}}$$

  where $A^+ = 26, y^+ = y\frac{v^*}{\nu}, v^* = \sqrt{\frac{\tau_\omega}{\rho}}$

- In the outer region the Clauser formula is used:

  $$\mu_o = kC_{cp}\rho F_{wake} F_{kleb}$$

$k = 0.0168$ is the Clauser constant, $C_{cp} = 1.6$, F wake limits the value of the eddy viscosity in the outer layer in presence of separations and wakes:

$$F_{wake} = min \left\{ y_{max}, f_{max}, C_{\omega k} u_{diff}^2 \frac{y_{max}}{f_{max}} \right\}$$

$$f(y) = y|\omega|D$$

y_max is the distance from the wall where f(y) has a maximum, D is set equal to zero in the wake region, $u_{diff} = |u_{max}| - |u_{min}|$ is the difference between maximum and minimum velocity in the outer layer, $|u_{min}| = 0$ except in the wakes, $C_{\omega k} = 1.0$. kleb is the Klebanoff intermittency function:

$$F_{kleb} = \left[1 + 5.5 \left(C_{kleb} \frac{y}{y_max} \right)^6 \right]^{-1}$$

with $C_{kleb} = 0.3$.

4.4.2 Wilcox k-w Model

The basic equations for this two-equation model are the same as for Wilcox (1988). In this model the eddy viscosity is given by: $\mu_t = \rho \frac{k}{\omega}$.
Two transport equations are solved for the turbulent kinetic energy k and the specific dissipation rate ω:

$$\frac{\partial \rho k}{\partial t} + u_j \frac{\partial \rho k}{\partial x_j} = P_k - \beta^* \rho k \omega + \frac{\partial}{\partial x_j} \left[(\mu + \sigma^* \mu_t) \frac{\partial k}{\partial x_j} \right]$$

$$\frac{\partial \rho \omega}{\partial t} + u_j \frac{\partial \rho \omega}{\partial x_j} = \alpha \frac{\omega}{k} P_k - \beta \rho \omega^2 + \frac{\partial}{\partial x_j} \left[(\mu + \sigma \mu_t) \frac{\partial \omega}{\partial x_j} \right]$$

where k is the turbulent kinetic energy and ω is the specific rate of dissipation of k The production term P_k is given as:

$$P_k = \tau_{ij} \frac{\partial u_i}{\partial x_j}$$

where

$$\tau_{ij} = \mu_t \left[\frac{\partial u_i}{\partial x_j} + \frac{\partial u_j}{\partial x_i} - \frac{2}{3} \frac{\partial u_i}{\partial x_j} \delta_{ij} \right] - \frac{2}{3} \rho k \delta_{ij}$$

The realizability constraint proposed by Durbin [[18]] is used to compute the eddy viscosity value. The boundary conditions are:

- inlet conditions:

$$\omega_\infty = \lambda \frac{u_\infty}{L}$$

$$\mu_{t\infty} = \chi_i \mu$$

$$k_i = \mu_{t\infty}\omega_\infty; \quad \omega_i = \omega_\infty$$

  a value ranging from 1 to 10 is suggested for the constant $\lambda(\lambda = 10default)$, L is the approximate length of the computational domain.

- otulet condition:extrapolation
  Boundary condition for rough and smooth surfaces
  The model uses the no-slip condition for velocity and turbulent kinetic energy: on solid walls k=0. ω satisfies the following equation near the wall (y→0):

$$\omega \frac{6\mu_\omega}{\rho_\omega \beta y^2}$$

  In practice this equation cannot be used for the evaluation of the boundary value for ω due to its infinite value on the wall.

- Boundary condition suggested by Menter:

$$\omega_\omega = 10\frac{6\nu_\omega}{\beta(\Delta y)^2} = 800\frac{\mu_\omega}{\rho_\omega(\Delta y)^2}$$

  where Δy is the grid spacing at the wall.

- On a rough surface:

$$\omega_\omega = \frac{\rho_\omega \nu^{*2}}{\mu_\omega} S_R = S_R \left(\frac{\partial u}{\partial y}\right)_\omega$$

  where the friction velocity is:

$$\nu^* = \sqrt{\frac{\tau_\omega}{\rho_\omega}}$$

- Wilcox 1998 [[22]] correlation:

$$S_R = \begin{cases} \left(\frac{50}{k_s^+}\right)^2, k_s^+ < 25 \\ \frac{100}{k_s^+}, k_s^+ \geq 25 \end{cases}$$

And k_s^+ is the non-dimensional sand grain height:

$$k_s^+ = \frac{\rho \nu^* k_s}{\mu_\omega}$$

k_s is the sand roughness height ($k_s^+ \leq 5.0$ for hydraulically-smooth surface).

Slightly-rough-surface boundary condition:

$$\omega_\omega = \frac{2500 \mu_\omega}{\rho_\omega k_s^2}$$

- Wilcox 2006 [[23]] correlation:

$$S_R = \begin{cases} \left(\frac{200}{k_S^+}\right)^2, k_S^+ < 25 \\ \frac{100}{k_s^+} + \left[\left(\frac{200}{k_S^+}\right)^2 - \frac{100}{k_s^+}\right] e^{(5-k_s^+)}, k_S^+ \geq 25 \end{cases}$$

Slightly-rough-surface boundary condition:

$$\omega_\omega = \frac{40000 \mu_\omega}{\rho_\omega k_s^2}$$

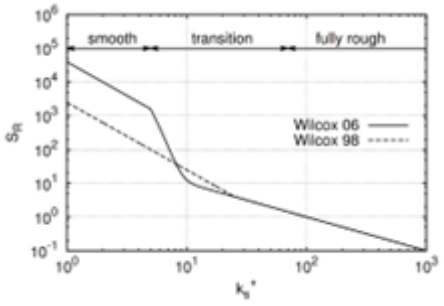

Figure 30: ROUGHNESS PARAMETER AFTER NIKURADSE ($K_S^+ < 400$)

4.4.3 Menter k-w SST Model

The $k-\omega$ equations are solved only inside the boundary layers and the standard $k-\epsilon$ model of Jones-Launder is utilized elsewhere. Menter developed a blending function F_1 that is equal to the one in the inner region and goes towards zero near the edge of the boundary layer.

$$\frac{\partial \rho k}{\partial t} + u_j \frac{\partial \rho k}{\partial x_j} = P - \beta^* \rho k \omega + \frac{\partial}{\partial x_j}\left[(\mu + \sigma_k \mu_t)\frac{\partial k}{\partial x_j}\right]$$

$$\frac{\partial \rho \omega}{\partial t} + u_j \frac{\partial \rho \omega}{\partial x_j} = \alpha \frac{\omega}{k} P - \beta \rho \omega^2 + \frac{\partial}{\partial x_j}\left[(\mu + \sigma_\omega \mu_t)\frac{\partial \omega}{\partial x_j}\right] + 2\rho\sigma_{\omega^2}\frac{1-F_1}{\omega}\frac{\partial k}{\partial x_j}\frac{\partial \omega}{\partial x_j}$$

P is the production of kinetic energy of turbulence and is modelled using the Boussinesq approximation as follows:

$$P = \tau_{ij}\frac{\partial u_i}{\partial x_j} = \left(2\mu_t S_{ij} - \frac{2}{3}\delta_{ij}\rho k\right)\frac{\partial u_i}{\partial x_j}$$

The last term in the ω equation is called the cross-diffusion term, that makes the model insensitive to the freestream ω. The blending function is given by:

$$F_1 = \tanh \Gamma^4$$

where

$$\Gamma = \min\left\{\max\left(\frac{\sqrt{k}}{\beta^* \omega d}\right), \frac{4\rho\sigma_{(\omega)^2} k}{CD_{k\omega} d^2}\right\}$$

The first term is the turbulent length scale divided by the wall distance, is about to 2.5 in the log-layer and tends towards zero in the defect layer; the second term exceeds unity only in the sublayer; the third term is designed to ensure correct behavior of F_1 in cases of very low freestream ω. $CD_{k\omega}$ stands for the positive portion of the cross-diffusion term:

$$CD_{k\omega} = \max\left(\frac{2\rho\sigma_{\omega^2}}{\omega}\frac{\partial y}{\partial x}\frac{\partial y}{\partial x}, 10^{-20}\right)$$

An upper limit for the principal turbulent shear stress in boundary layers is introduced in order to avoid excessive shear stress levels typically predicted with Boussinesq eddy-viscosity models:

$$\mu_t = \frac{a_1 \rho k}{\max(a_1 \omega, |\Omega_{ij}| F_2)}$$

In Boundary layer flows, the principal turbulent shear stress depends on k as follows:

$$\mu_t = \frac{|\rho \overline{u'' v''}|}{|\Omega_{ij}|} = \frac{a_1 \rho k}{|\Omega_{ij}|}$$

This is called SST limitation for μ_t, the SST limitation is suitable only for wall-bounded flows, the purpose of the function F_2 is to prevent the activation of the SST limitation in free shear flows. Otherwise F_2 behaves like F_1 except that it remains at unity further out in the defect layer, and it is given by:

$$F_2 = \tanh \Gamma_2^2$$

where:

$$\Gamma_2 = \max\left(\frac{2\sqrt{k}}{\beta^* \omega d}, \frac{500\mu}{\rho \omega d^2}\right)$$

The boundary conditions are the same as in the Wilcox $k - \omega$ HRN model.

4.4.4 RQEVM Model

The realizable quadratic eddy-viscosity model (RQEVM) proposed by Rung [[19],[21], is based on the original EARSM by Gatski and Speziale [[20]]. The Reynolds stresses are modelled by:

$$-\rho \overline{u_i' u_j'} = 2\mu_t S_{ij} - \frac{2}{3}\rho k \delta_{ij} - \rho k a_{ij}$$

where the extra anisotropy tensor is defined as:

$$a_{ij} = -2C_\mu^* \tau^2 \left[\beta_2 (S_{ik}\Omega_{kj} + S_{jk}\Omega_{ki}) - \beta_3 (S_{ij}^2 - \frac{1}{3}\delta_{ij} S_{kk}^2)\right]$$

the turbulent time scale is given by $\tau = \frac{1}{\beta^* \omega}$ and the effective turbulent viscosity is:

$$\mu_t = \frac{C_\mu^*}{\beta^*} \frac{\rho k}{\omega}$$

The anisotropy parameter is defined as:

$$C_\mu^* = \frac{\beta_1}{1 - \frac{2}{3}\eta^2 + 2\xi^2}$$

The strain and rotation rate tensors are given by:

$$S_{ij} = \frac{1}{2}\left(\frac{\partial U_i}{\partial x_j} + \frac{\partial U_j}{\partial x_i} - \frac{2}{3}\frac{\partial U_k}{\partial x_k}\delta_{ij}\right); \quad \Omega_{ij} = \frac{1}{2}\left(\frac{\partial U_i}{\partial x_j} - \frac{\partial U_j}{\partial x_i}\right)$$

The coefficients and auxiliary functions are defined as [[19]]:

$$\eta^2 = \frac{\beta_3^2 S^2}{8}; \quad \xi^2 = \frac{\beta_3^2 \Omega^2}{2}; \quad \beta_1 = \frac{\frac{4}{3} - C_2}{2g}; \quad \beta_2 = \frac{2 - C_4}{2g}; \quad \beta_3 = \frac{2 - C_3}{2g}$$

$$g = f_g(C_1 - 1) + \frac{S^2}{4 + 1.83\sqrt{0.8\Omega^2 + 0.2S^2}}$$

$$f_g = 1 + 0.95\left[1 - \tanh\left(\frac{S^2}{4.6225}\right)\right]$$

$$C_1 = 2.6; \quad C_2 = \max\left(0.4, \frac{1.5S^{1.7}}{17.1 + 1.875S^{1.7}}\right); \quad C_3 = 1.25, \quad C_4 = 0.45$$

being $\beta^* = 0.09, k$ and ω are the solution of the standard Wilcox $k - \omega$ model [[22]].

5 3D Flutter Analysis

5.1 Workflow Flutter

Before starting with the case study and the results of the analyses performed, it may be appropriate to enumerate the necessary steps for a typical uncoupled flutter simulation.

1. **Modal Analysis** : to calculate natural frequencies and modal shapes, and to obtain the nodal displacements of component of interest to simulate the motion of the structure;

2. **CFD Steady State** : to calculate the mean flow field, it is an initialization of the analysis that will be used afterwards; for this purpose it is possible to use H-type or O-type grid ;

3. **Grid Alignment** : it consists of the alignment between the FEM mesh and the CFD mesh, it should be the most accurate possible in order to simulate the most similar interaction of structure and fluid;

4. **Aeroelastic Computation** : it is the core of flutter stability analysis, an unsteady CFD simulation is performed in order to evaluate the aerodynamic work per cycle.

5.2 Type of Solvers

Lars-MS It is a time-Linearized aeroelastic response solver, that performs analysis starting from the initialization of the CFD steady state flow field computed with *Traf-MBH* solver.
It is based on the uncoupled approach.
The equations are time linearized by using the mean flow obatined with Traf-MBH and the harmonic perturbation, the flow field unsteadiness generated by the blade harmonic motion, is computed with Lars-MS.
The numerical stability is guaranteed by the artificial dissipation and different techniques are used to speed up convergence, as for example local time stepping, multigrid and residual smoothing. The equation that represents the velocity field is the following:

$$\underline{U'} = \underline{U} + Re\left[\underline{\hat{U}}_{\delta} e^{j\omega t}\right]$$

where $\underline{U'}$ is the disturbed velocity field, $\underline{U}$ is the mean velocity field and $Re\left[\underline{\hat{U}}_{\delta} e^{j\omega t}\right]$ is the real components of the modal disturbs.

Traf-MBH It is a code designed for cascade flow predictions, where there are implemented different model equations, turbulence closures and spatial discretization.
It is based on the uncoupled approach and in fact uses the modal analyses results to simulate how the blade vibrates with the specific mode, the grid vibrates, and how the CFD grid interact with the FEM one. The equations are solved in time and the period of computation is the following one:

$$\Delta\tau = \frac{2\pi}{\omega}\frac{1}{N_{div}}$$

where ω is the angular frequency and N_{div} represent the number of divisions of the blade vibration period.

5.3 FEM BC and results

It is important to define the boundary conditions around the FEM model in order to process a modal analysis. The modal analysis will be useful for the flutter computation, because the displacements of the structure are necessary to simulate the influence of the moving FEM mesh on CFD mesh.

5.3.1 FEM Model Configuration

Our objective is to analyze the flutter stability of LPT rotating blades, focusing onto the ARiAS 144 blades, built for studying aeroelastic phenomena.

In the next picture it's possible to admire a part of the real bladed disk:

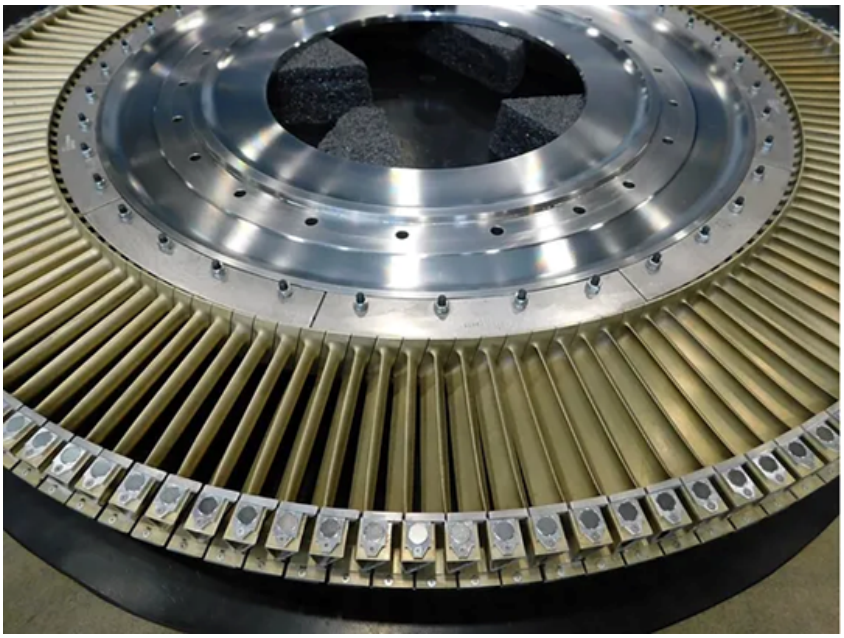

Figure 31: ARiAS Bladed Disk

In the next picture is represented the FEM model of the bladed disk:

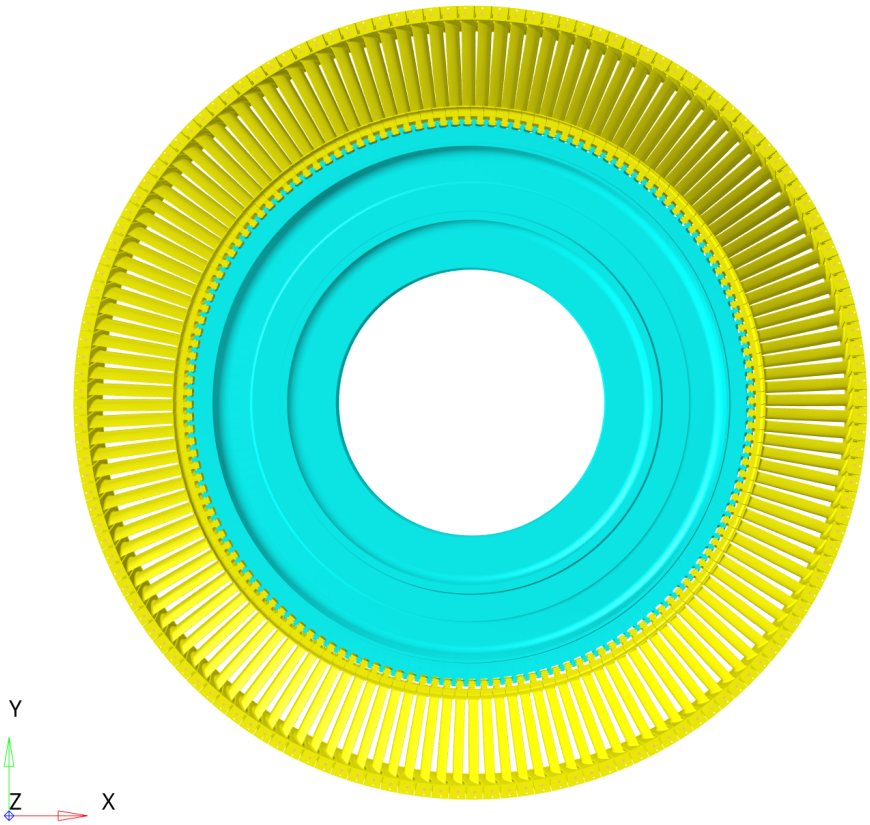

Figure 32: ARiAS Bladed Disk FEM Model

The configuration of blade chosen as ***Case Study Model*** is the following one:

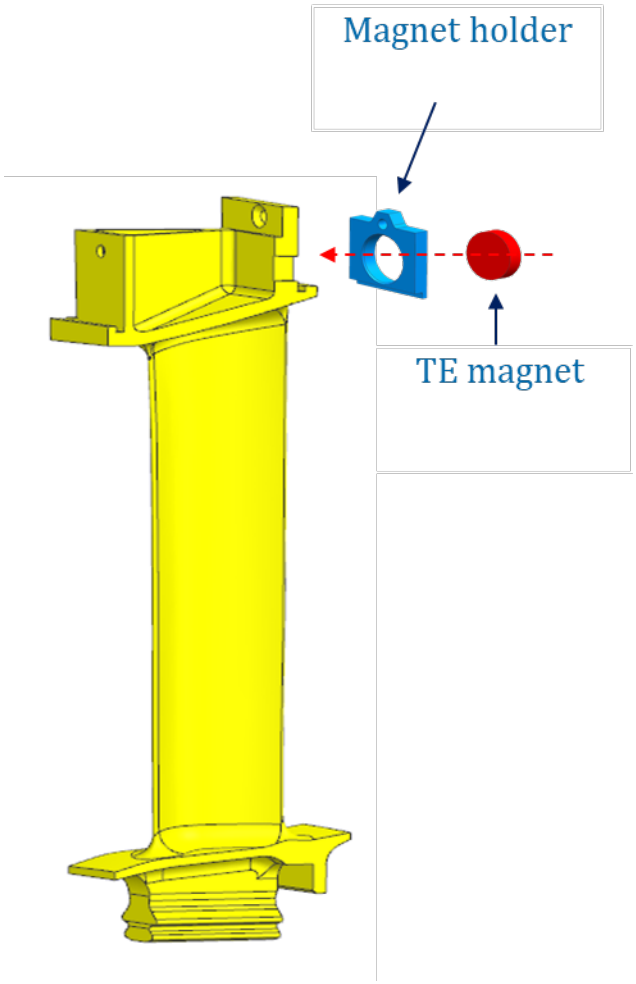

Figure 33: Chosen Configuration ARiAS Blade

For meshing the model was used the software Hypermesh Altair and then the preliminary modal analyses regarding the ARiAS LPT blade were realized on Ansys Mechanical APDL.
As we can see in the following pictures, in the FEM model used in multiple analyses there are second order 3D tetra elements, in particular:

- ***Bladed Disk Total Elements*** = 227102
- ***Blade Elements*** = 184385
- ***Bladed Disk Total Nodes*** = 370899
- ***Blade Nodes*** = 301513

For what concerns the different ***materials***:

- Disk Material: Steel, E = 200000 MPa
- Blade Material: Aluminum, E = 71000 MPa

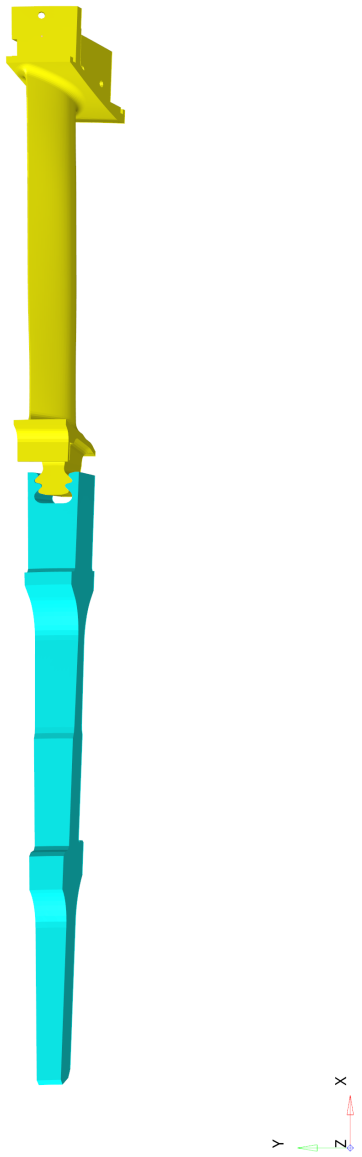

Figure 34: Blade + Disk FEM Model

5.3.2 Boundary Conditions

A rear magnet connected with RBE3 is visible in the following pictures, and it represents a mass without rotary inertia.
This type of connection distributes the force applied at the master node to a set of slave nodes [11].

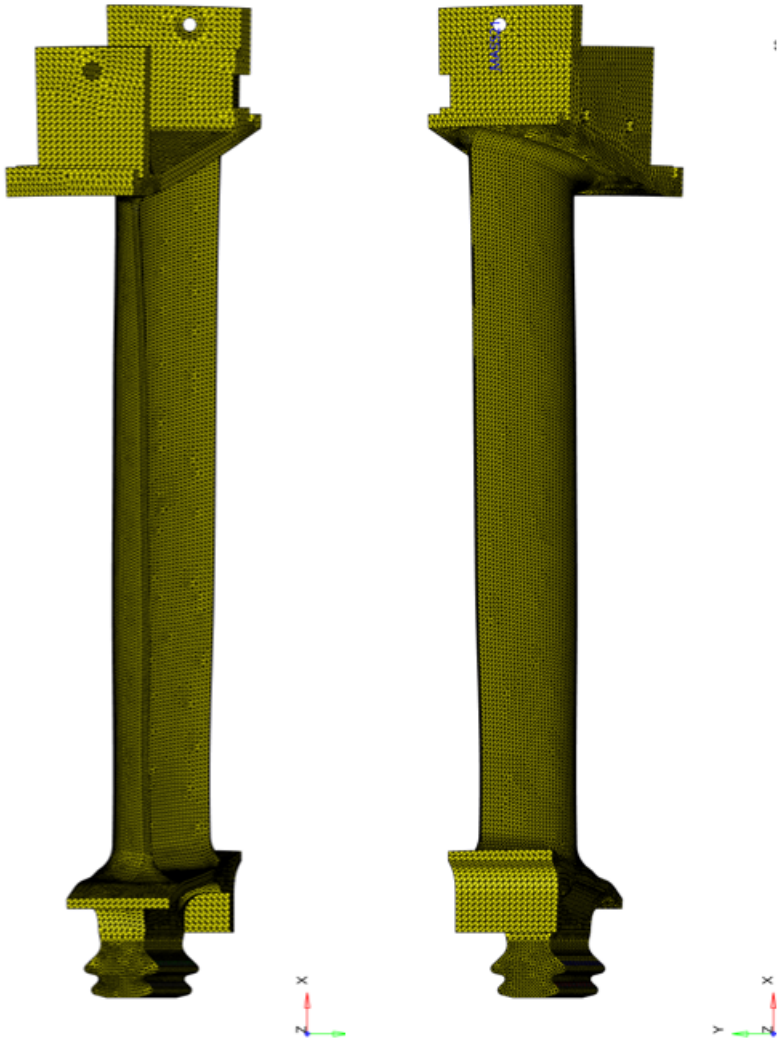

Figure 35: ARiAS blade mesh

In the following picture is possible to see the RBE3 connection in pink:

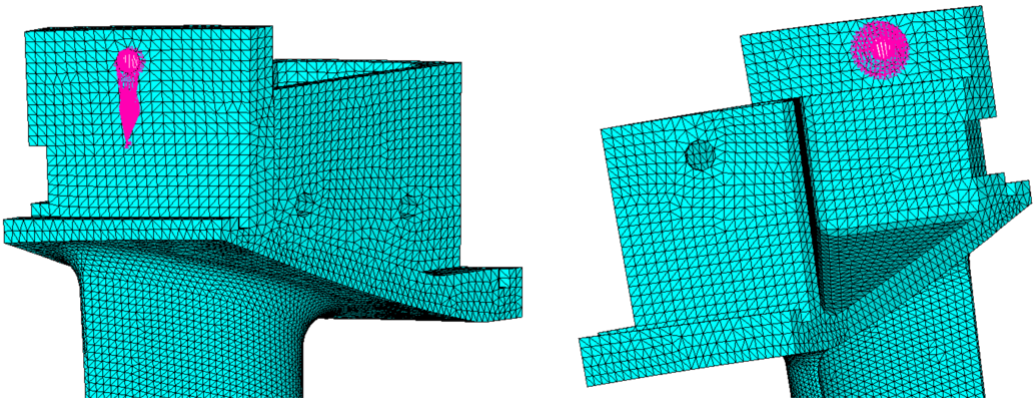

Figure 36: Mass Rear Magnet

In the following picture are visible the Boundary Conditions imposed on the disk, in particular y and z direction are bounded, so only the x direction (radial) is free:

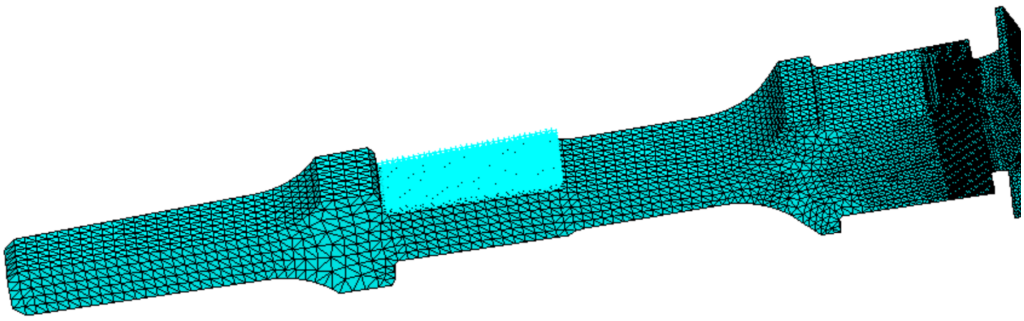

Figure 37: Boundary Conditions on Disk

In order to perform modal analysis, the bladed disk sector was duplicated by imposing cyclic symmetry conditions. The Cyclic Symmetry is applied at the two interfaces' nodes between subsequent blades at suction side and pressure side, as visible in the following picture:

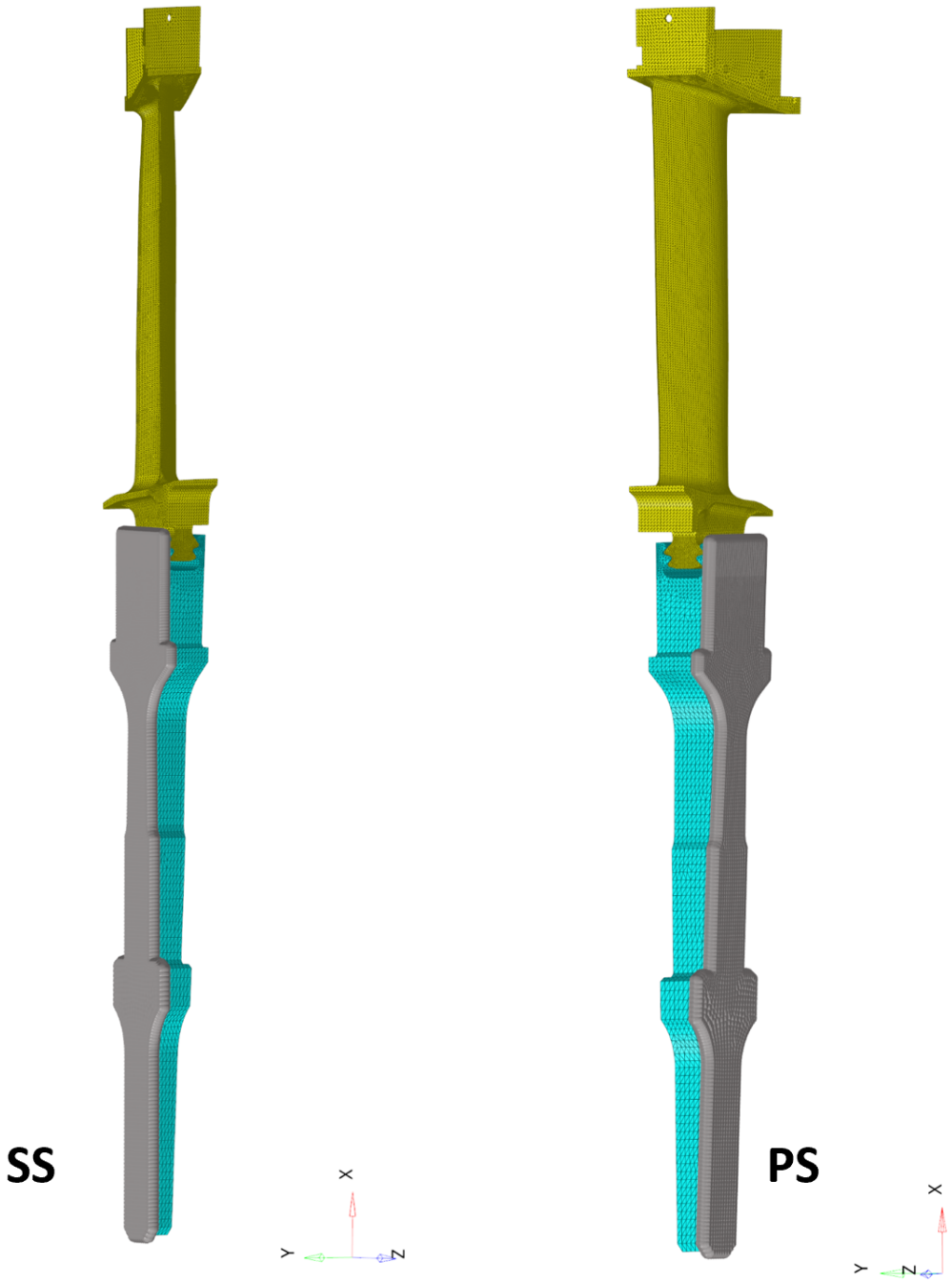

Figure 38: Cyclic Symmetry Suction and Pressure Side on Disk

5.3.3 Results Modal Analysis

In order to analyze the flutter phenomenon of the bladed disk ARiAS, it is important to set the point at which the analyses are going to be run.

- rotation speed = 2850 rpm –> N = 103%
- density = $\rho = 100\%$

In the following sections, are described the sensitivities around the closure turbulence model and on two different flutter solvers. This was made in order to evaluate the differences between the solution obtained with a time linearized method and a non linear one, and to highlight the accuracy of the solution.
It was also important to highlight the difference in terms of numerical model to describe the boundary layer.
First of all, the **Modal Analysis** was made, and in the following plot is visible the trend of frequency with nodal diameters, in a plot called FREND:

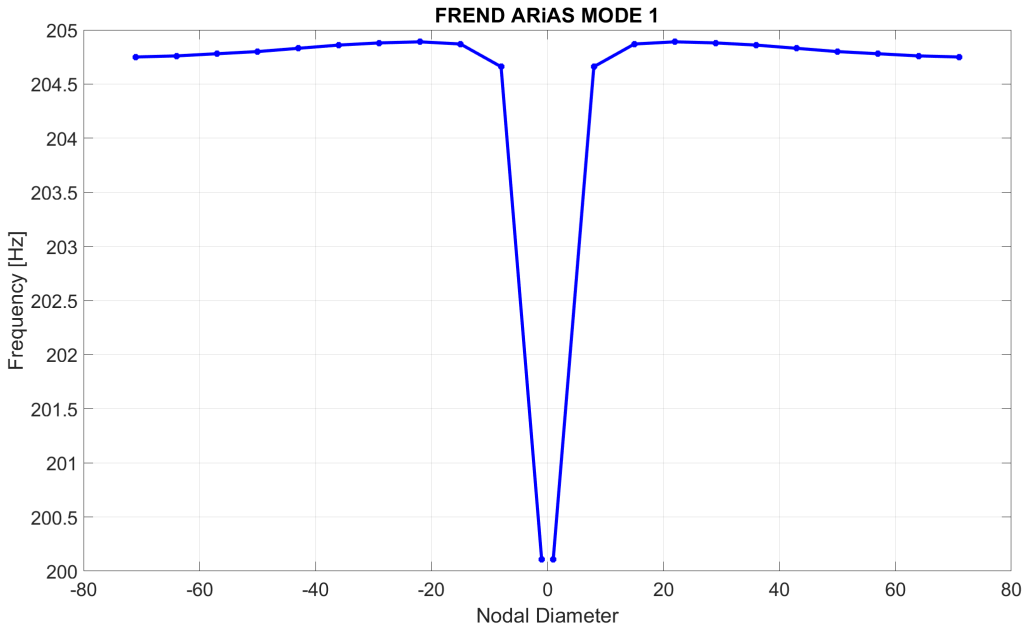

Figure 39: FREND Mode 1

The modeshape identified for these low vibration frequency is called **Flap**, that is characterized by a flex around the machine axis with maximum deformation on the shroud, as visible in the next pictures.

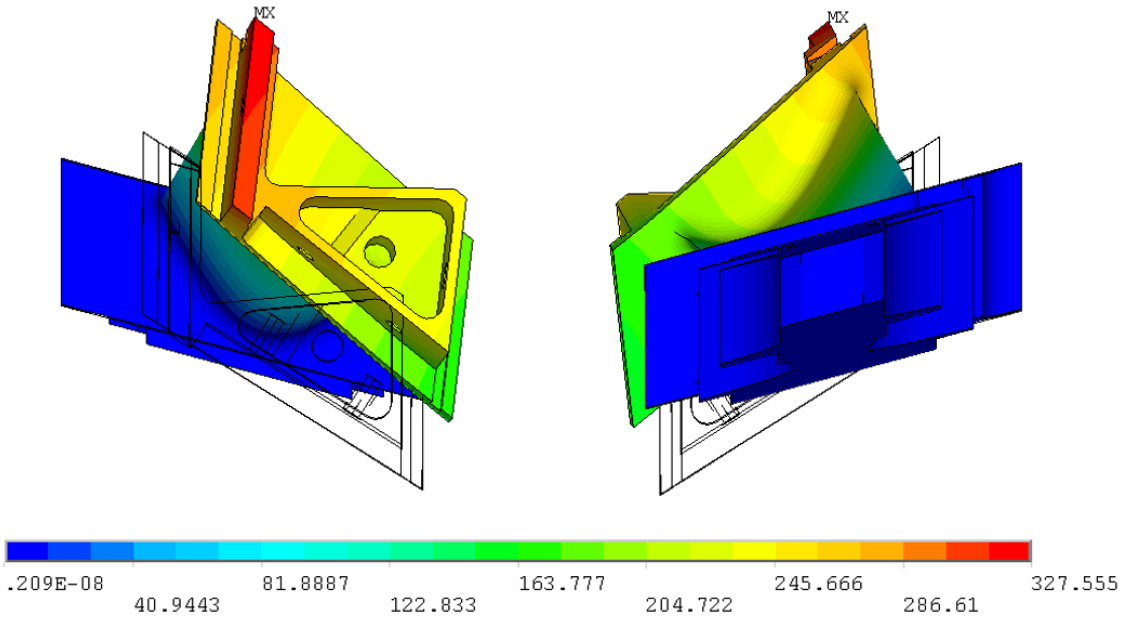

Figure 40: Flap modeshape, ND=29 ,Upper side and Lower side

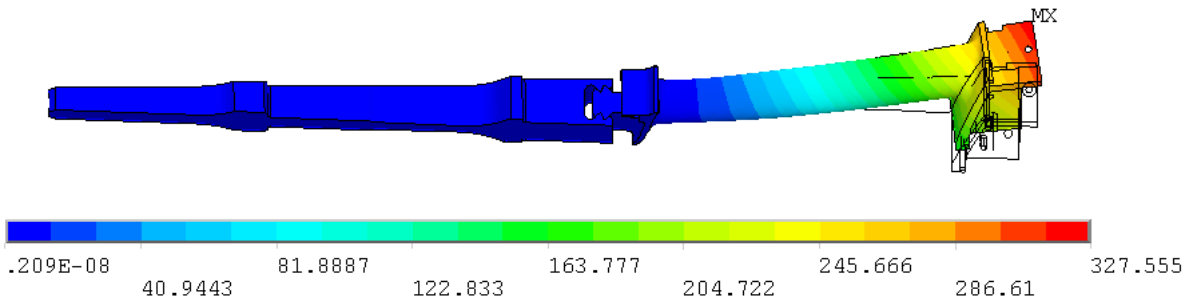

Figure 41: Flap modeshape, ND=29, Frontal view

In the next pictures is visible the behavior of the bladed disk at different nodal diameters for the first mode, where it is represented the total displacements.

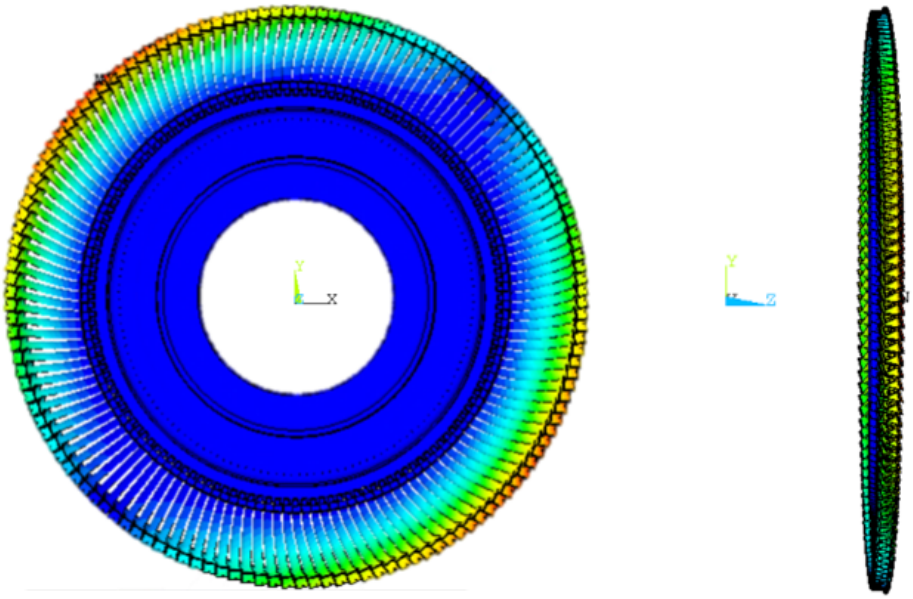

Figure 42: MODE 1, ND=1, Displacement Front and Side View

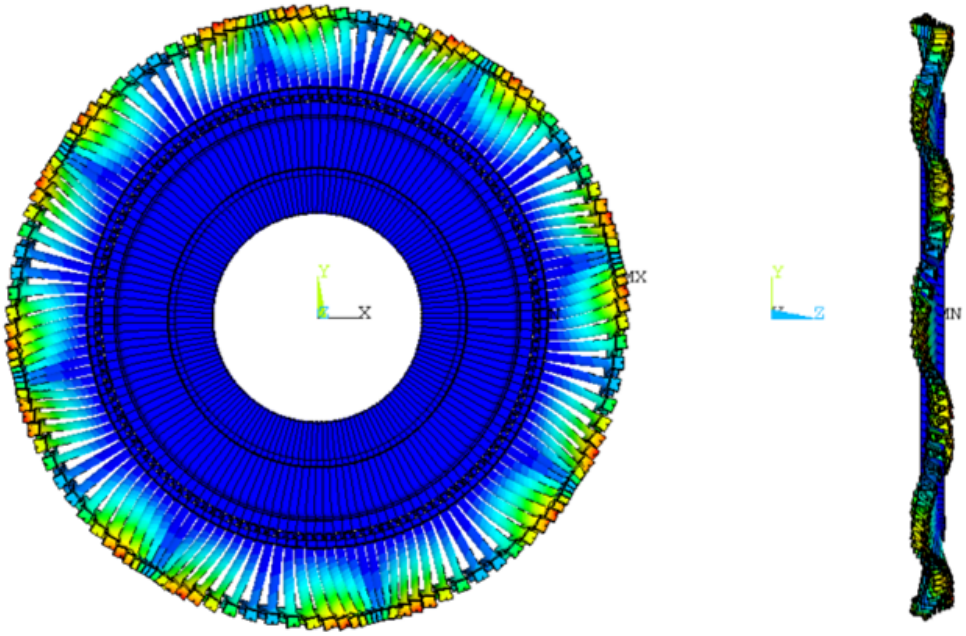

Figure 43: MODE 1, ND=8, Displacement Front and Side View

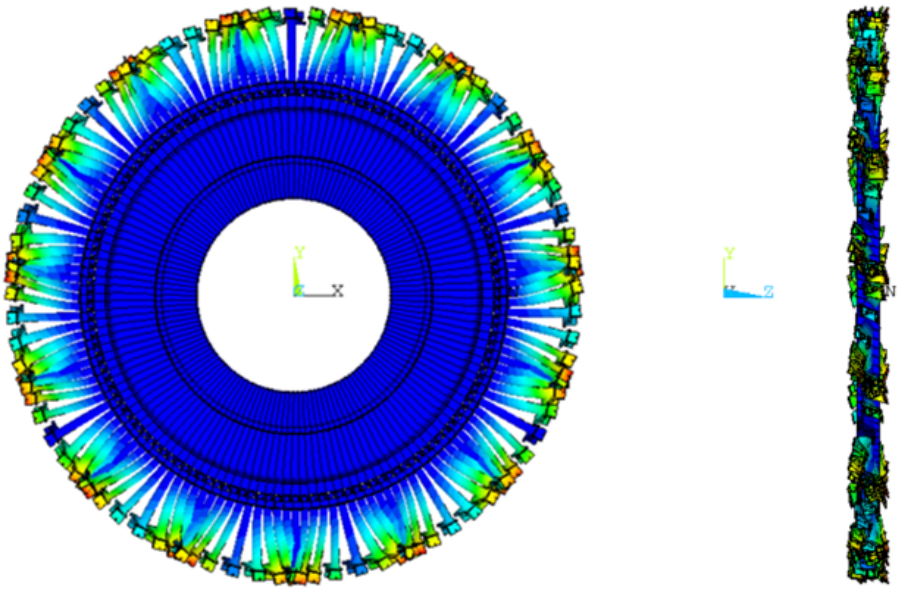

Figure 44: MODE 1, ND=15, Displacement Front and Side View

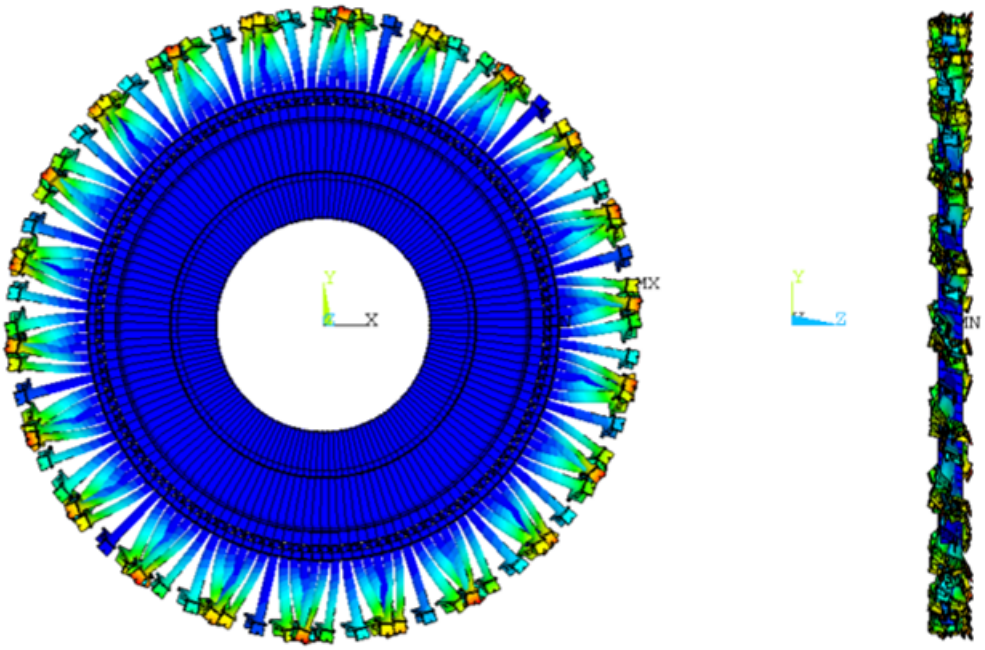

Figure 45: MODE 1, ND=22, Displacement Front and Side View

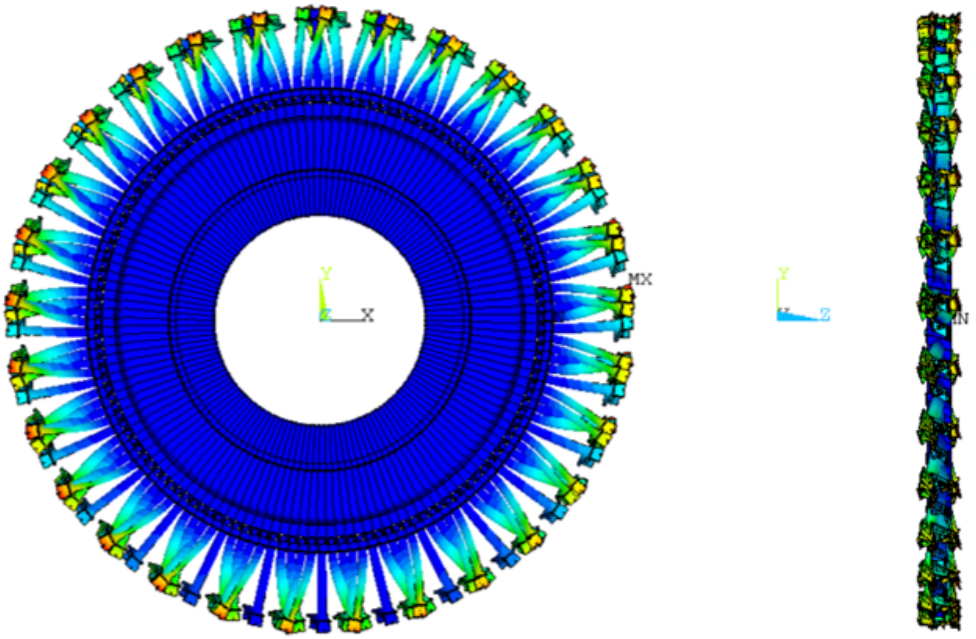

Figure 46: MODE 1, ND=29, Displacement Front and Side View

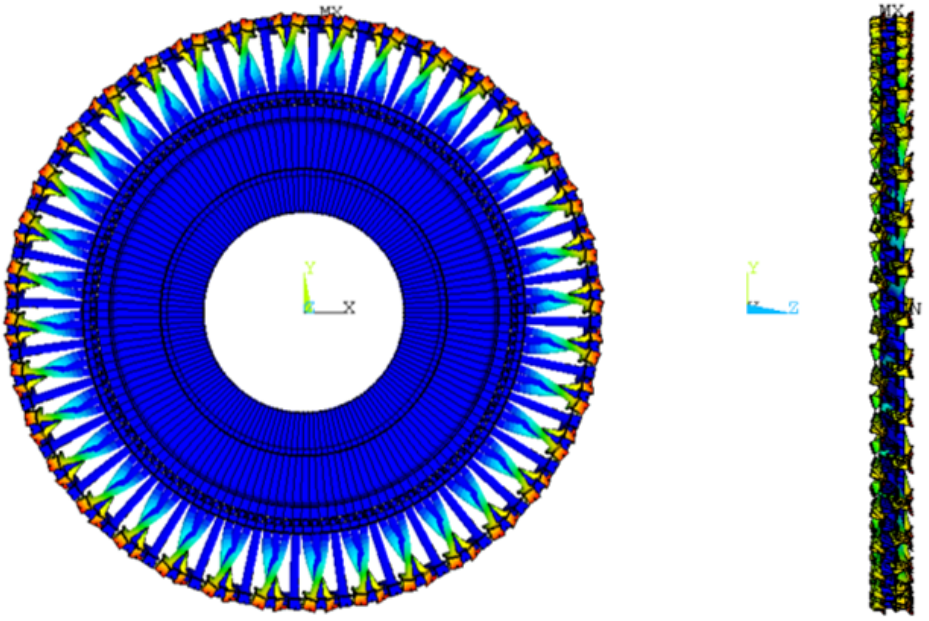

Figure 47: MODE 1, ND=36, Displacement Front and Side View

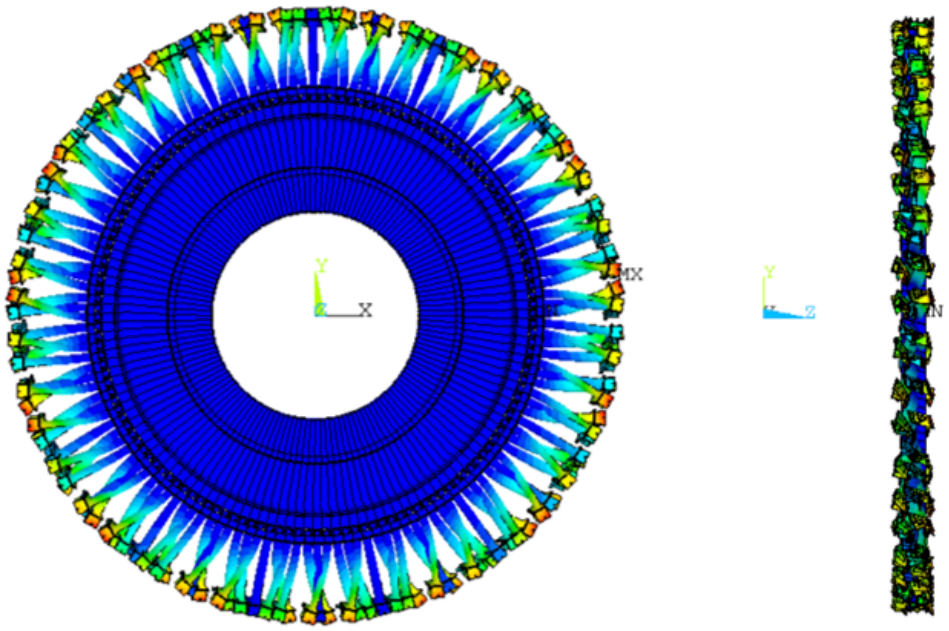

Figure 48: MODE 1, ND=43, Displacement Front and Side View

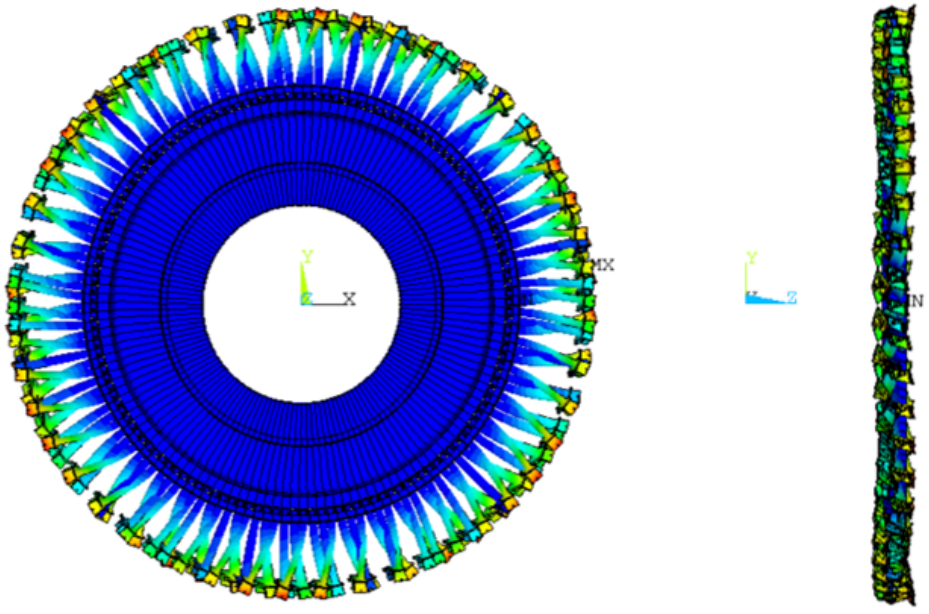

Figure 49: MODE 1, ND=50, Displacement Front and Side View

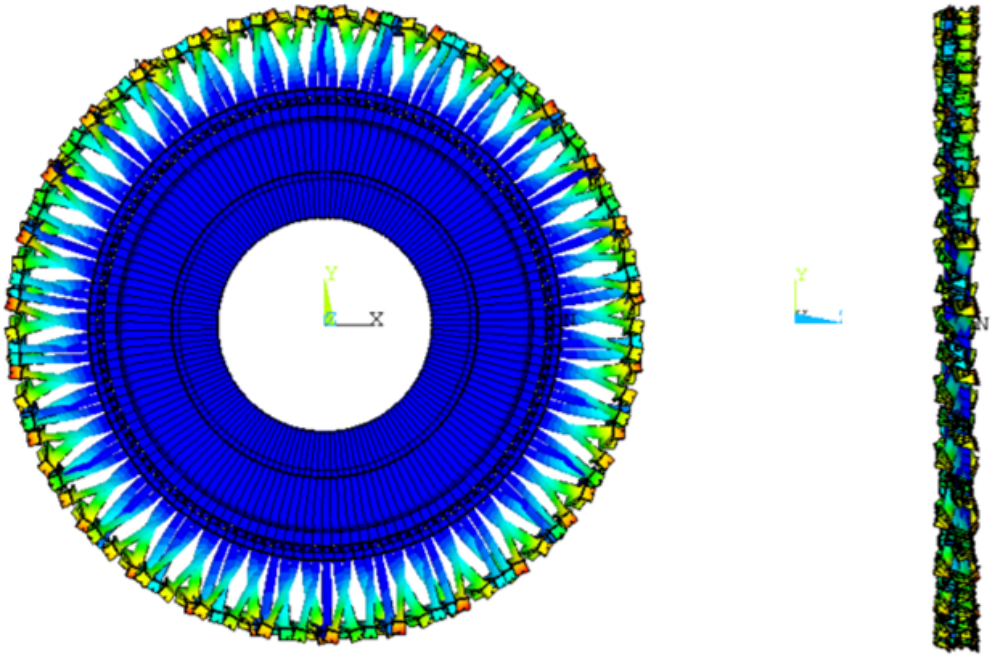

Figure 50: MODE 1, ND=57, Displacement Front and Side View

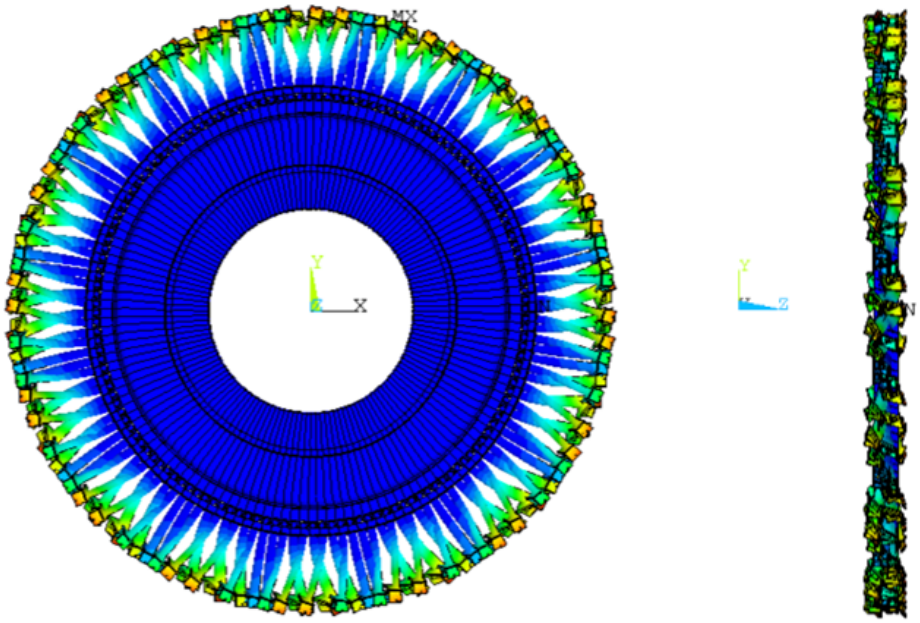

Figure 51: MODE 1, ND=64, Displacement Front and Side View

5.4 CFD BC and results

After the post processing of the modal analysis, we computed the CFD steady state, that will be the same for linearized and non-linearized computations, solved with the TRAF code, that was developed by University of Florence for internal fluxes.

5.4.1 CFD BC for Steady State

In order the compute CFD steady state for the case study, it is necessary to define the inlet and outlet conditions of the domain, to solve the equations with the finite volumes code named before. In particular, the TRAF code, requires in input the following parameters:

- **inlet** $= \alpha, \beta, p_1^\circ, T_1^\circ$
- **outlet** $= p_2$

The equations regarding α: blade-to-blade angle and β: streamline flow angle, are the following ones:

$$\alpha = \arctan \frac{C_\theta}{C_x}$$

$$\beta = \arctan \frac{C_r}{\sqrt{C_x^2 + C_\theta^2}}$$

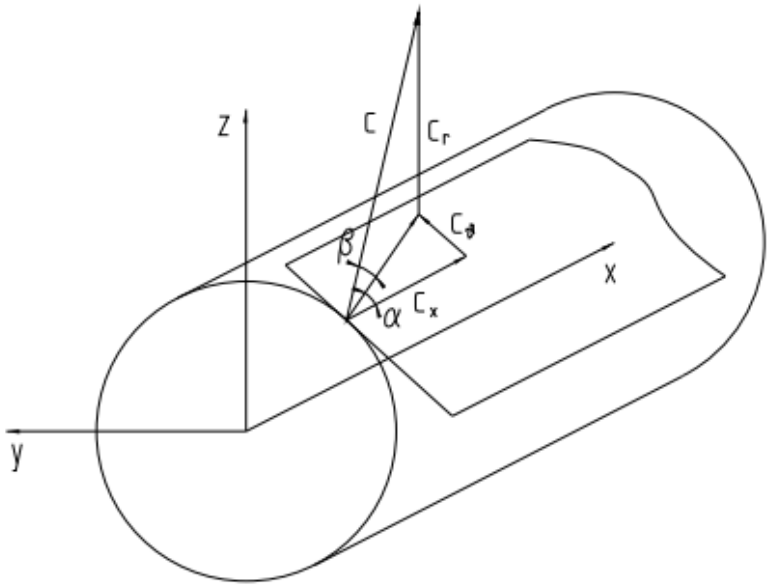

Figure 52: Absolute flow angles α and β for a generic axial turbomachine

In the following pictures are reported the trend of Total Temperature, Total Pressure, Alpha and Beta angle at **Inlet** and Static Pressure at **Outlet** along the blade span.

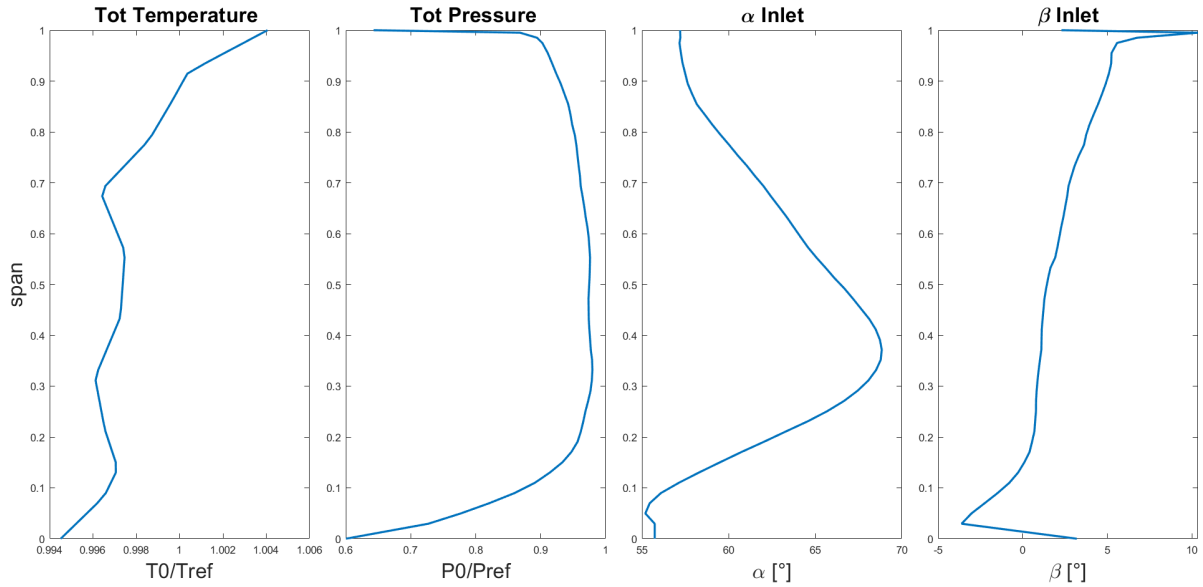

Figure 53: Boundary Conditions at Inlet

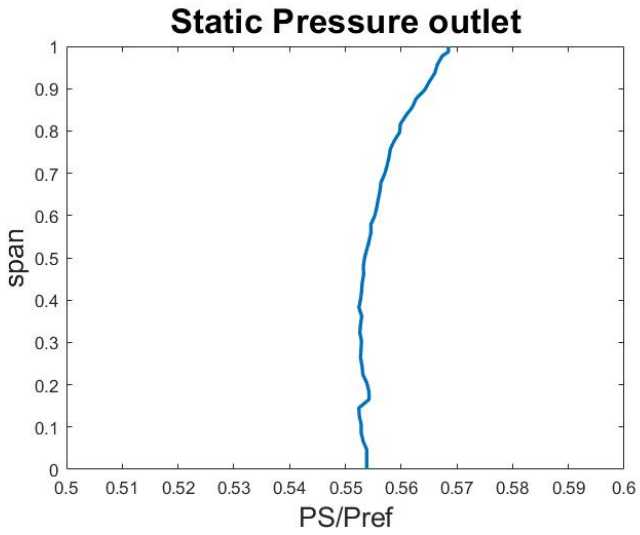

Figure 54: Boundary Conditions at Outlet

Here follows a visual representation of Static Pressure at inlet and outlet of the CFD domain.

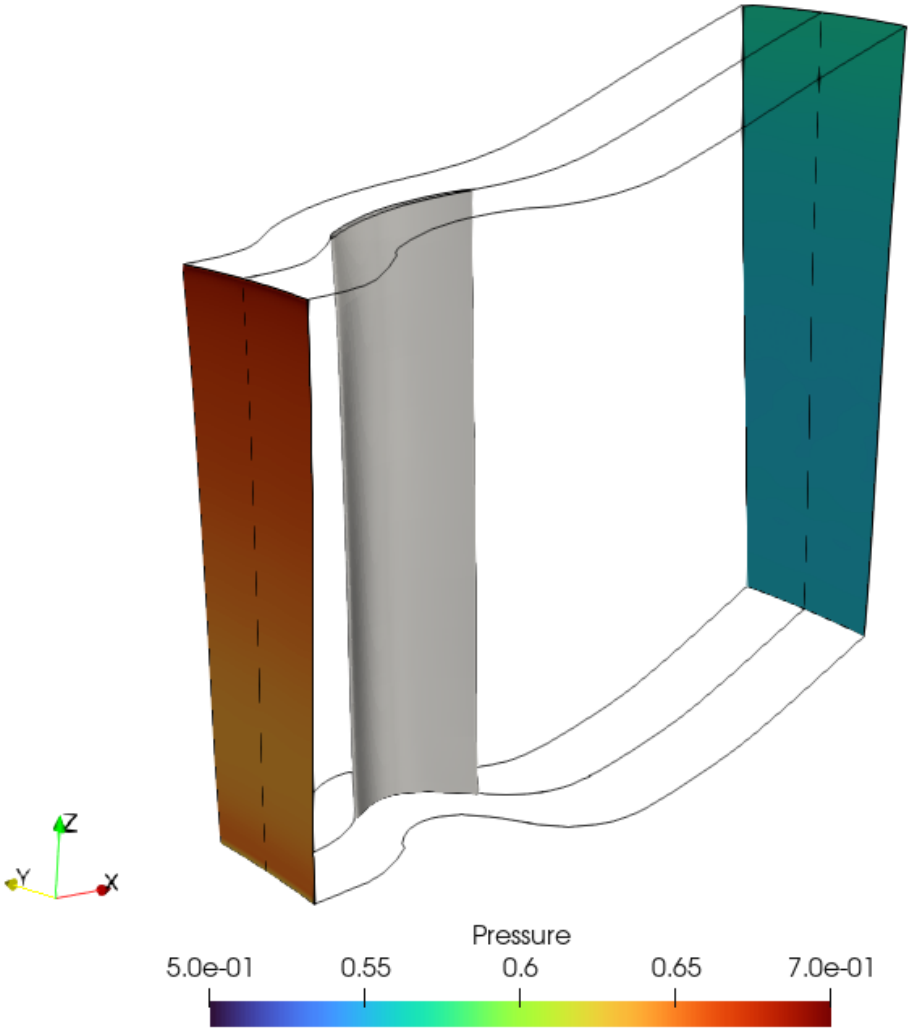

Figure 55: Pressure In and Out Conditions

5.4.2 Results of CFD Steady State

In this section we are going to compare the different closure turbulence models, that approximate differently the boundary layer on the blade. First of all, the boundary conditions for inlet and outlet of the CFD domain are imposed.
Then the CFD steady state was computed with four different turbulence models and the convergence was evaluated with Traf solver, visible on the next picture.
On the y axis is represented the log(R), where R is for the norm of residual, defined as:

$$R = \frac{1}{N} \sum_{n=1}^{N} \sqrt{\sum_{i=1}^{5} R_i^2}$$

with $N = nx \cdot ny \cdot nz$ mesh cells. The target of convergence is half-order above the machine accuracy in single precision.

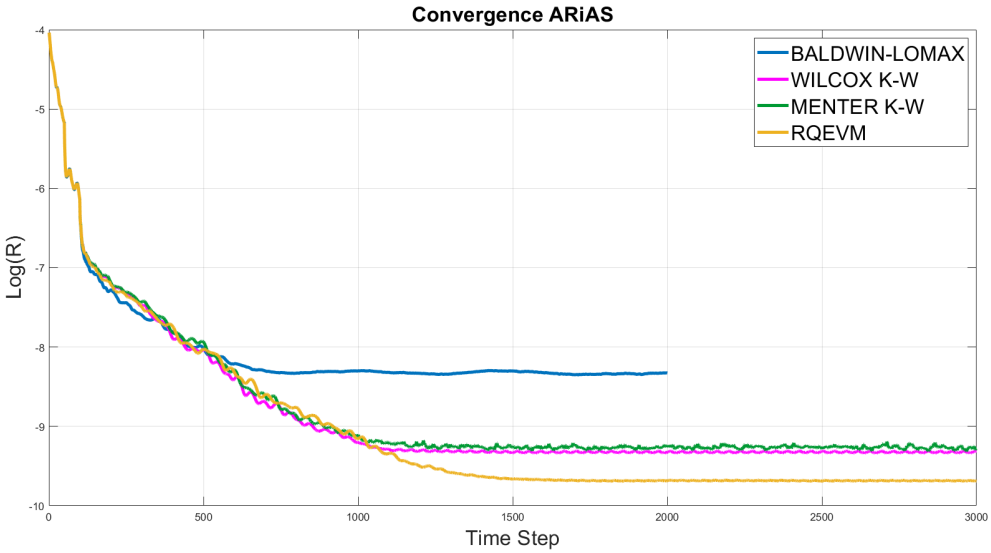

Figure 56: Convergence of Different Turbulence Models

It is visible how the Baldwin-Lomax model reaches convergence with 1500-2000 time steps, and the other models take about double time steps. The complexity of numerical calculus implemented by the different models is visible also with the value of norm of residual. The more accurate the method, the lower the log(R) value is.

For post processing the CFD steady state results, the blade span was 'cut' at five different percentages to see the static pressure distribution along the dimensionless chord, in order to evaluate the differences in the approximation. In the following pictures we are going to see the flow field of Static Pressure along three cuts on the CFD domain at different blade spans.

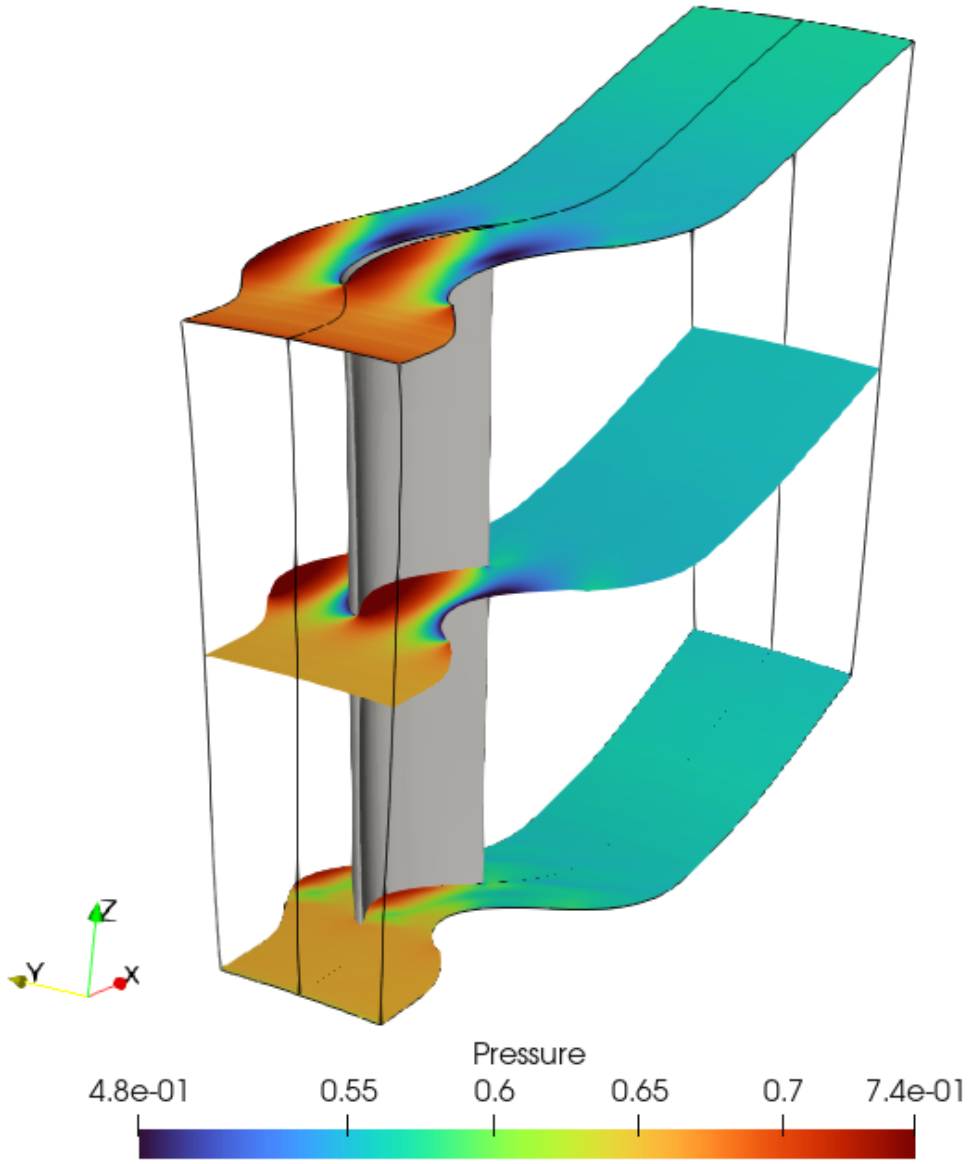

Figure 57: Static Pressure at 5%, 50% and 95% of blade span

Let's see the streamlines at the same blade span percentages in term of Mach number.

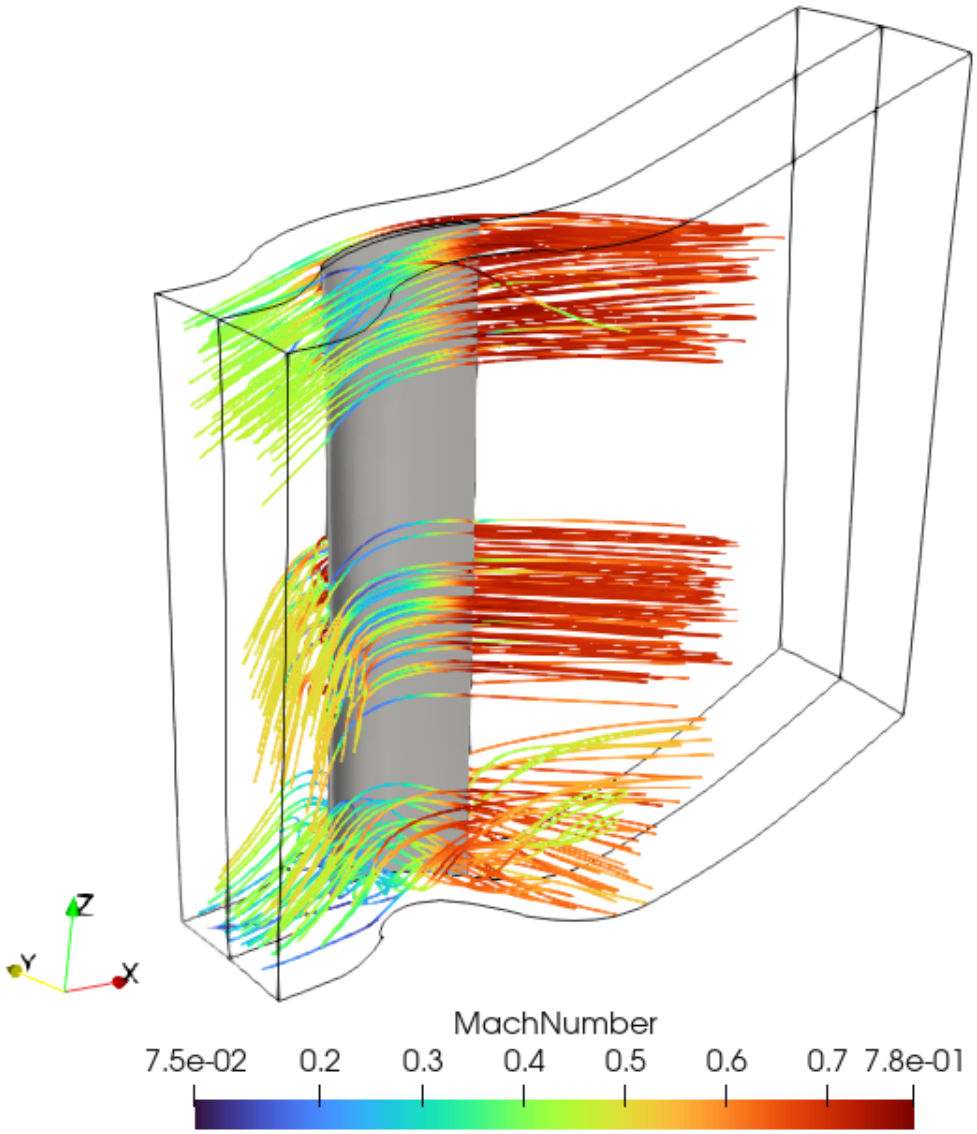

Figure 58: Mach Number at 5%, 50% and 95% of blade span

Clearly the LPT blade is in subsonic regime and there aren't non-linear phenomena in the flow field. This means that a linearized solver can be used to compute the aerodamping in order to evaluate if the blade is stable or not. The results of the analyses are shown in the next pages.

In the following plots is represented the Static Pressure Distribution along the dimensionless axial chord at different percentages.

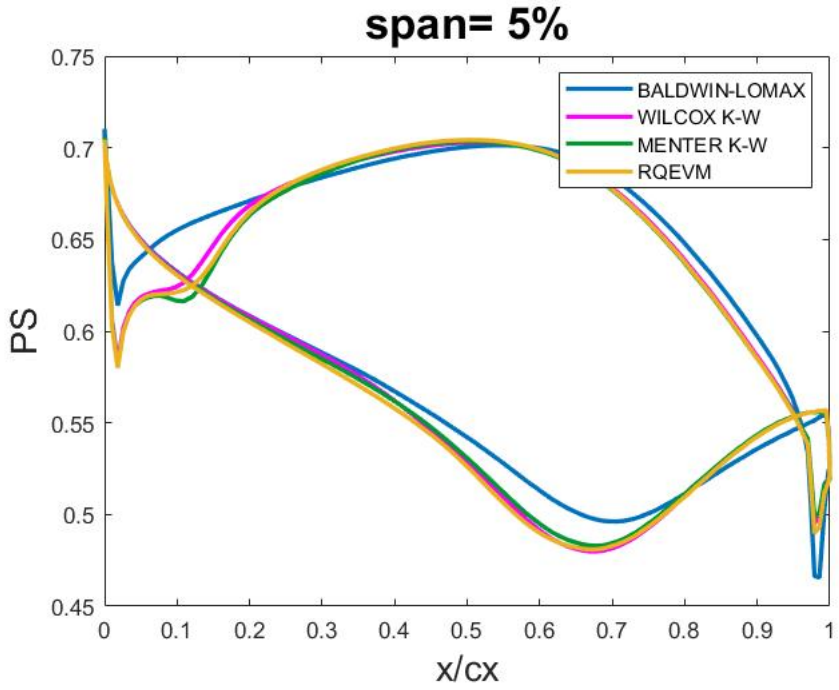

Figure 59: Static Pressure distribution along axial chord at 5% blade span

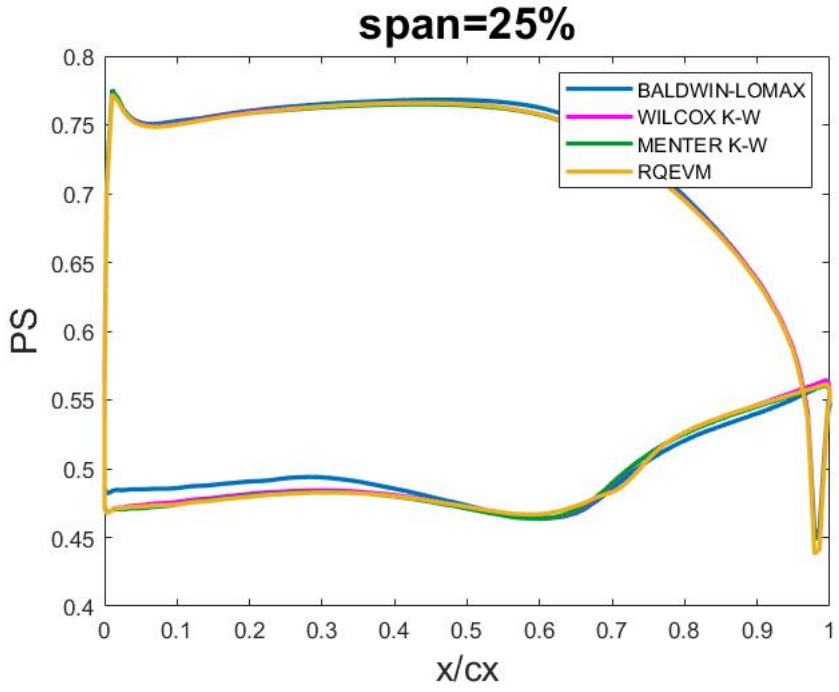

Figure 60: Static Pressure distribution along axial chord at 25% blade span

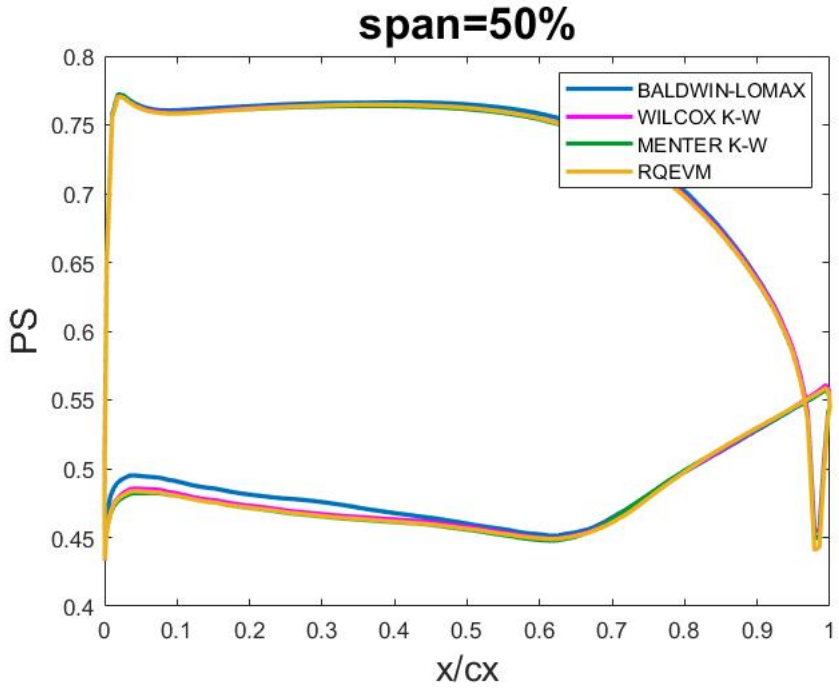

Figure 61: Static Pressure distribution along axial chord at 50% blade span

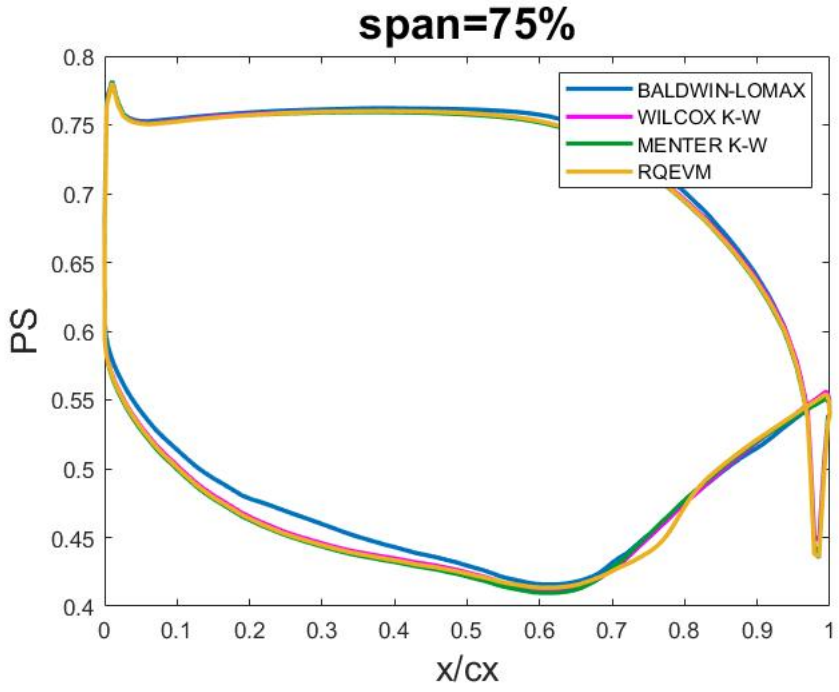

Figure 62: Static Pressure distribution along axial chord at 75% blade span

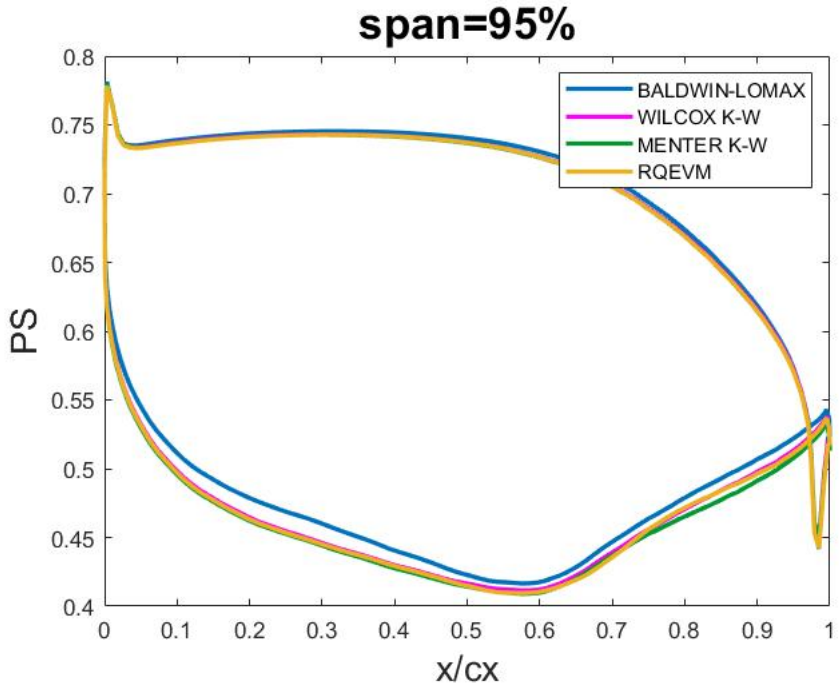

Figure 63: Static Pressure distribution along axial chord at 95% blade span

The differences in the Static Pressure distribution are more evident at 5% of blade span; they are caused also by a different span distribution at hub and tip (inlet file for boundary conditions) and development of secondary flow near the HUB caused by the interaction between fluid and structure.

5.5 Mesh Alignment

It was necessary to align the FEM (pink) and CFD (white) mesh, but for simplicity the blade was cut, not considering the contribute given by the fillet. In the next picture, the meshes used for the tests are visible (on the right).The meshes on the left are the ones that represent faithfully the blade shape, but a simplification was made to reduce computational costs of flutter simulation.

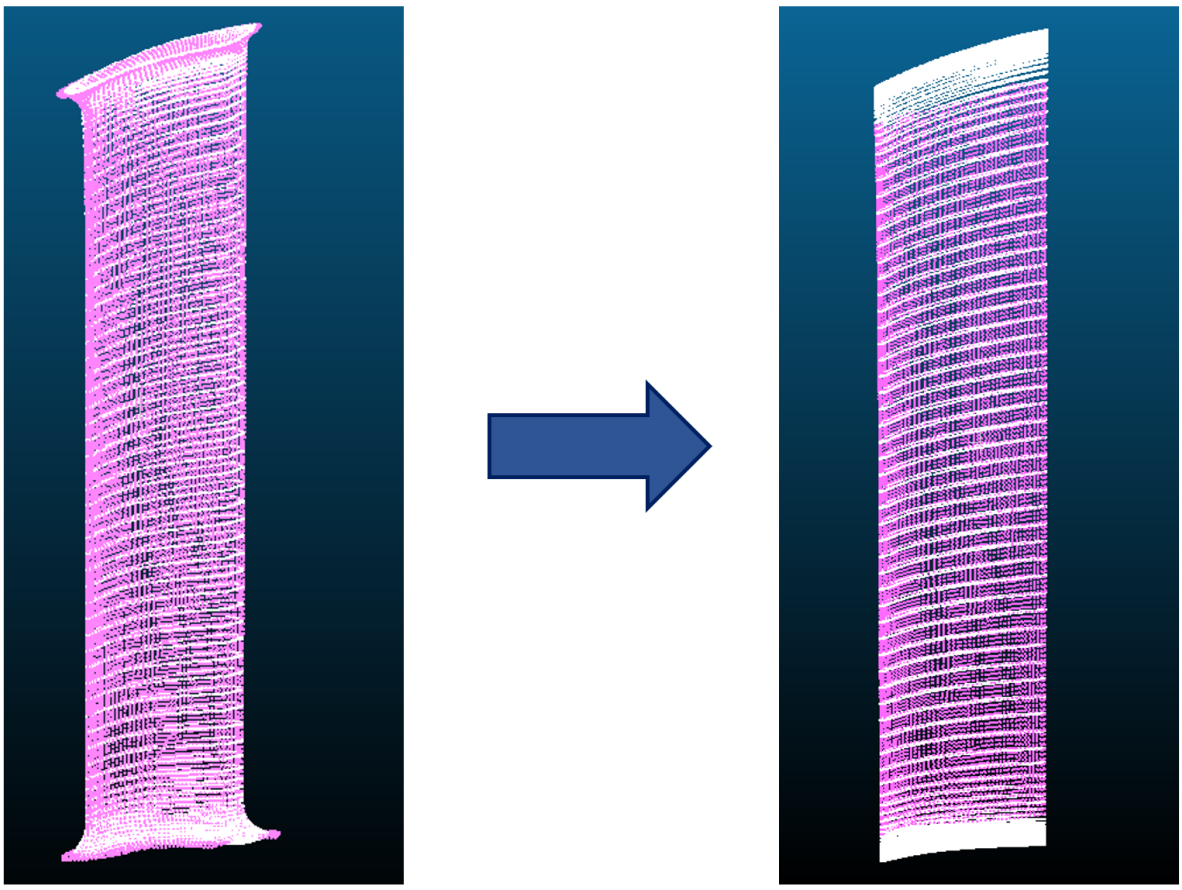

Figure 64: Mesh Alignment Simplified

5.6 Sensitivity on Turbulence Models

In this section are analyzed the results of flutter stability analyses. It is important to remember that the operational point was always the same, and the closure turbulence models implemented were four with two different solvers, one linearized and the other non-linearized.

At first were made the analyses with the *linearized solver*, called LARS.

In the following picture is plotted the Energetic Damping Coefficient for every Nodal Diameter. It is important to highlight that we don't know the behavior of the blade, so it is necessary to analyze the stability of every nodal diameter.

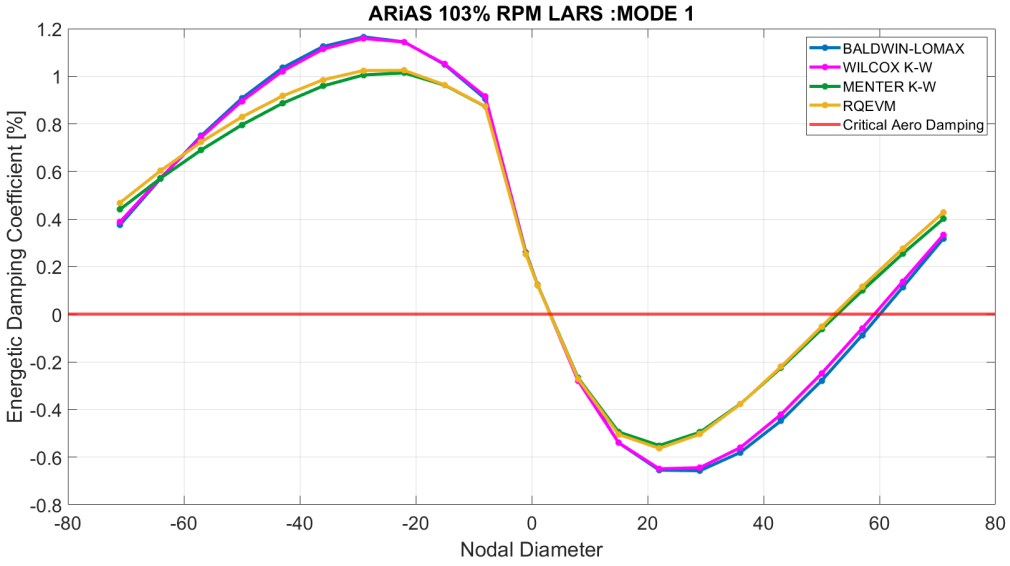

Figure 65: Energetic Damping Coefficient with the turbulence models with LARS solver

As visible in the previous image, the most unstable nodal diameter results to be ND=22, except for the Baldwin-Lomax turbulence model as we will see in the next section.

LARS ND=22	
Turbulence model	Aerodamping [%]
Baldwin-Lomax	-0.654634
Wilcox k-w	-0.648922
Menter k-w	-0.551091
RQEVM	-0.562883

Table 1: Lars turbulence model ND=22

Then the same analyses were made with the non-linearized solver, called TRAF, with the four different models.

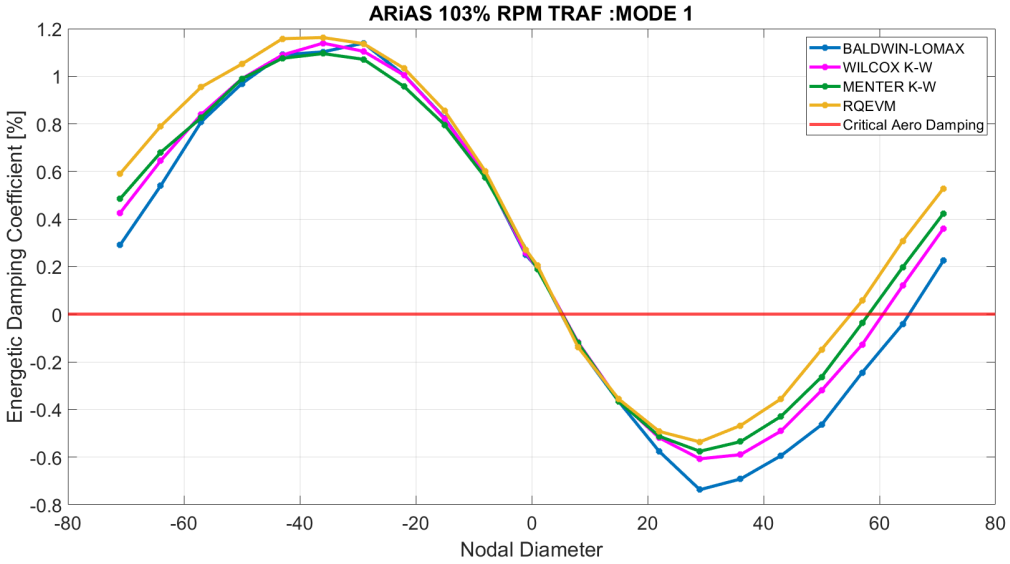

Figure 66: Energetic Damping Coefficient with the turbulence models with TRAF solver

In this case the most unstable nodal diameter results to be ND=29.

TRAF ND=29	
Turbulence model	Aerodamping [%]
Baldwin-Lomax	-0.736893
Wilcox k-w	-0.607005
Menter k-w	-0.575371
RQEVM	-0.536064

Table 2: Traf turbulence model ND=29

Let's see the Energetic Damping Density on blade with ND=29 and the Pressure Harmonic Phase and Amplitude.

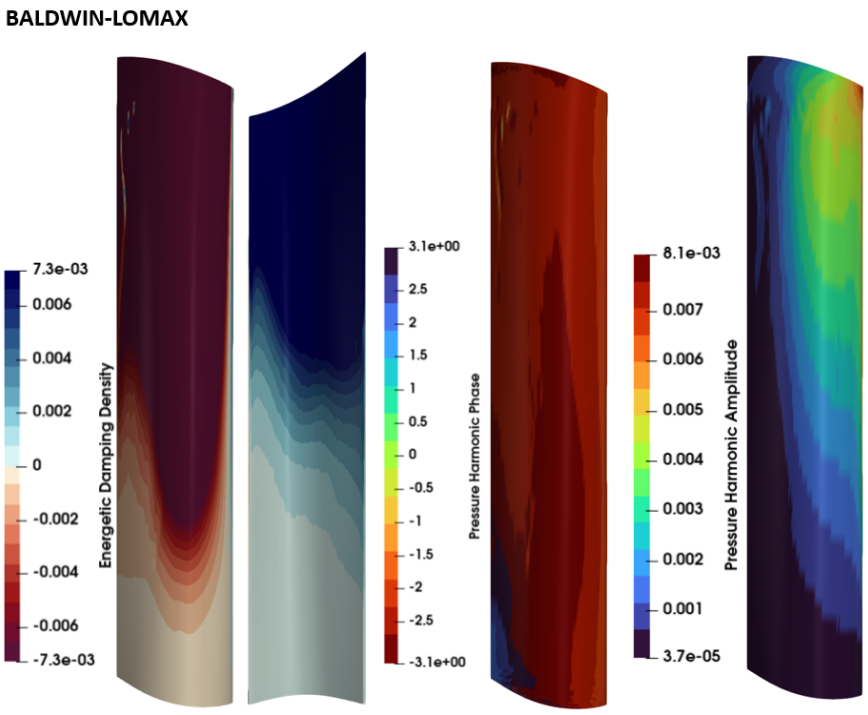

Figure 67: Energetic Damping Density on SS and PS and Harmonic Pressure for Baldwin-Lomax

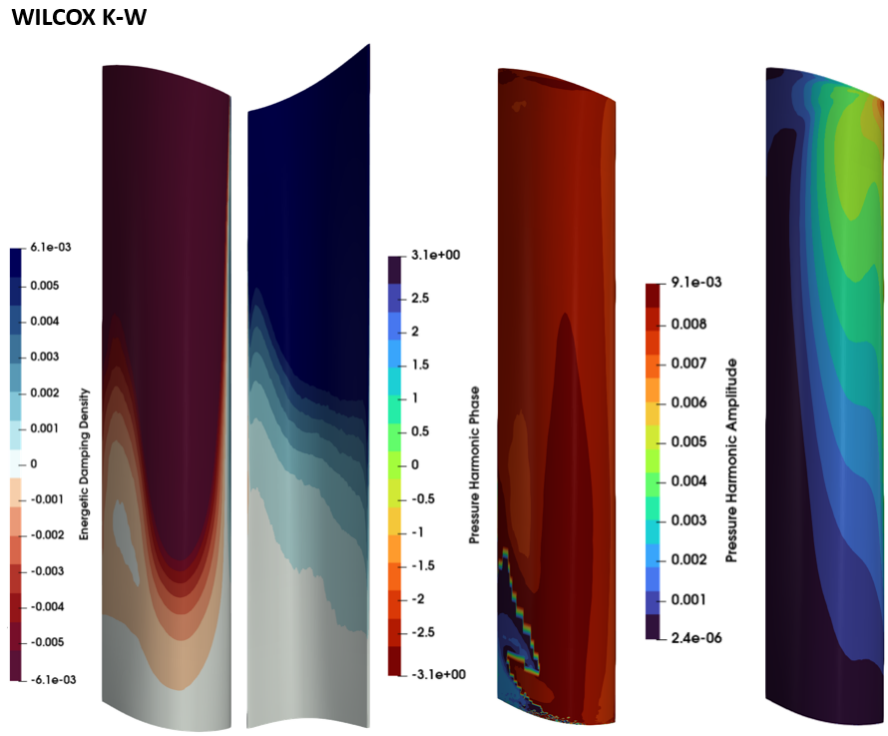

Figure 68: Energetic Damping Density on SS and PS and Harmonic Pressure for Wilcox k-w

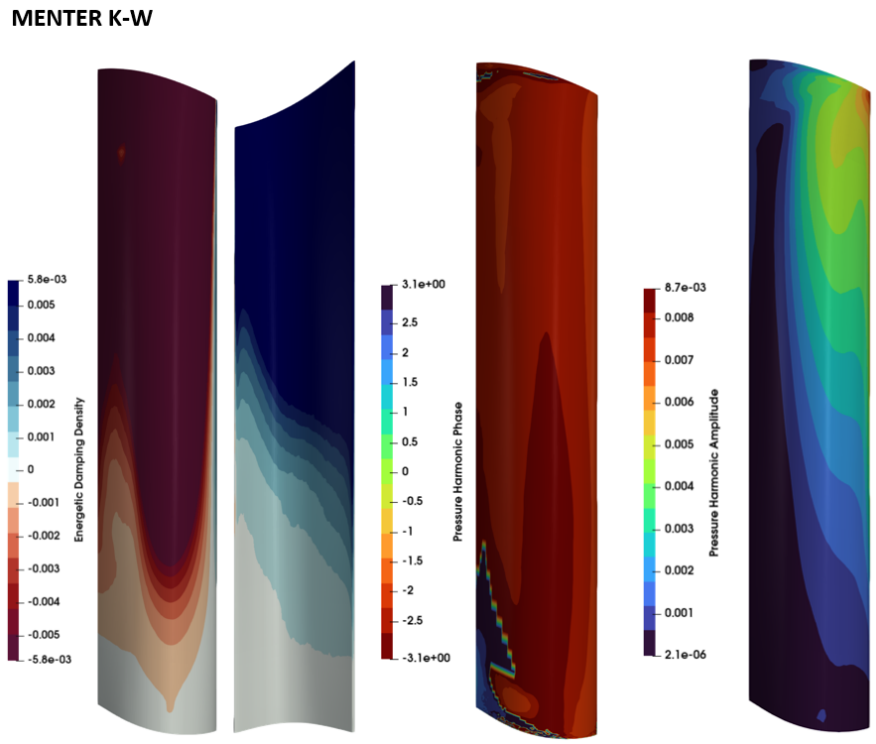

Figure 69: Energetic Damping Density on SS and PS and Harmonic Pressure for Menter k-w

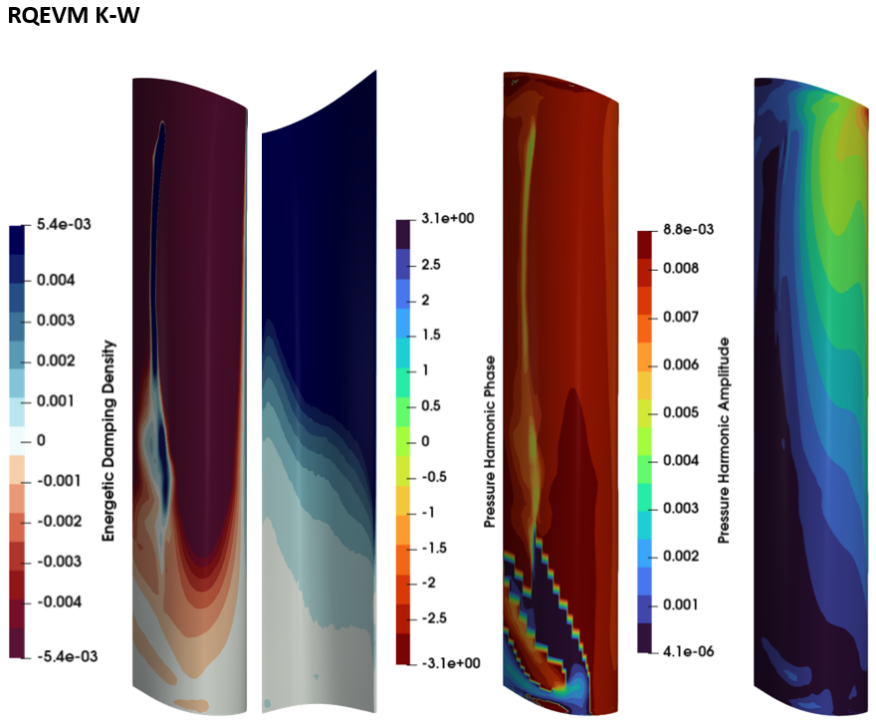

Figure 70: Energetic Damping Density on SS and PS and Harmonic Pressure for RQEVM k-w

The Suction Side, where the flow accelerates, is the most active in term of vibration excitement. The **Energetic Damping Density** is mostly negative on the suction side for the different turbulence models analyzed. The Pressure Side is always stable.
There is a large unstable area near the blade tip responsible to the high rotor instability. It is possible to evaluate the areas of major instability on the blade by looking at the Pressure Harmonic Phase and Amplitude distribution. For the **Pressure Harmonic Phase**, an unstable area is characterized by a phase shift >0; a stable area instead is characterized by a phase shift <0. Looking at the **Pressure Harmonic Amplitude**, the most stressed area is near the Leading Edge. [24]

It is visible that improving the turbulence method used, the blade results more stable, as a blue zone appears on the suction side.

In both cases for linearized and non-linearized methods, the most unstable nodal diameter values of aerodamping are over-estimated with Baldwin-Lomax models. Either methods predict a similar level of instability. Improving the turbulence model used, it is visible from the plots a little improvement of instability.

In fact, with TRAF solver, implementing a more accurate turbulence model, leads to a stabilization of the blade. With LARS, is visible that Baldwin-Lomax and Wilcox k-w model time-averaged have similar values of aerodamping. The same consideration can be done for Menter k-w and RQEVM with LARS.
By only looking at the value of energetic damping coefficient obtained with RQEVM model, the two values with a linearized method and a non linearized one are similar; this means that with the most accurate turbulence model in our disposal, if we are not in presence of non-linear phenomena, the linearized method approximates well the solution.
The substantial difference appears in the calculation time for TRAF and LARS. In the following tables is an example of calculation time for flutter with the different turbulence models with 8 cores.

LARS WITH 8 CORES	
Turbulence model	Time [hh:mm:ss]
Baldwin-Lomax	0:47:45
Wilcox k-w	0:47:41
Menter k-w	0:56:55
RQEVM	0:43:41

Table 3: LARS turbulence models WITH 8 CORES

TRAF WITH 8 CORES	
Turbulence model	Time [hh:mm:ss]
Baldwin-Lomax	19:41:03
Wilcox k-w	8:55:31
Menter k-w	10:42:42
RQEVM	18:56:44

Table 4: TRAF turbulence models WITH 8 CORES

It is evident that computation times taken for LARS simulation are similar between the different turbulence models, because this software solves linearized equation.
For TRAF we have huge differences with a remarkable increase of time, improving the turbulence model.

In the following section comparing one turbulence model with non-linearized and linearized solver, will be visible the huge difference in computation times. It is also true that with LARS we take 2000 steps against the 50x80x15=60000 steps with TRAF.

Let's see the computation time taken for every nodal diameter on HPC (high performance cluster), for simulations with 2 cores, for the turbulence models analyzed with both solvers:

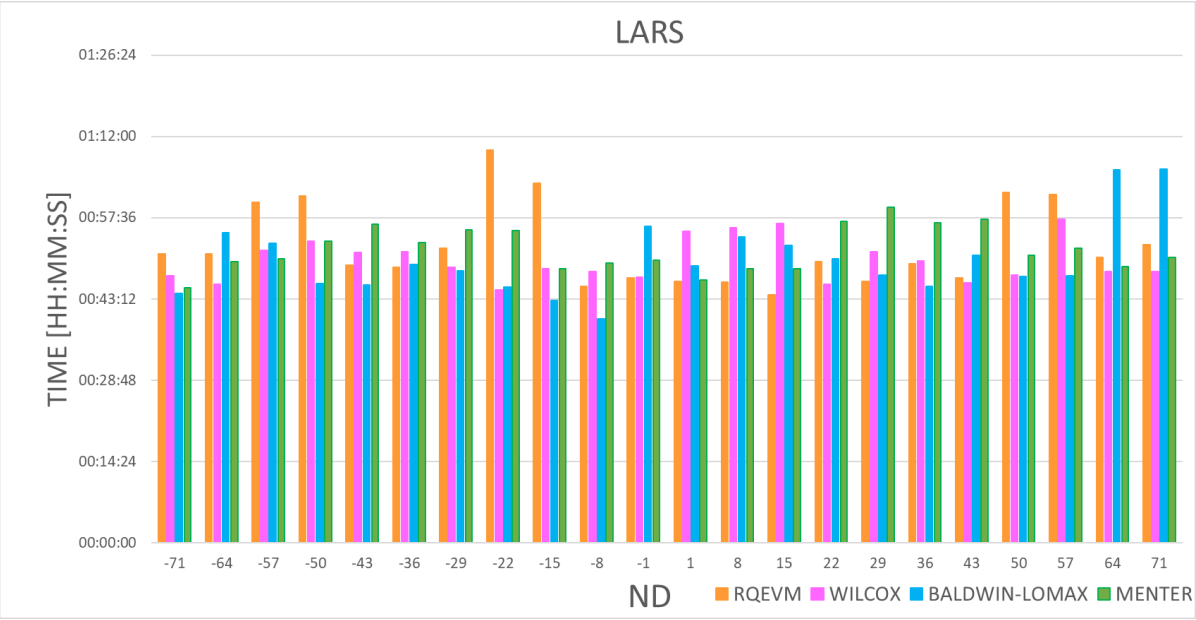

Figure 71: Computation time LARS

LARS WITH 2 CORES		
TURBULENCE MODEL	TOTAL TIME [hh:mm:ss]	MEAN TIME ND [hh:mm:ss]
Baldwin-Lomax	18:21:53	0:50:05
Wilcox k-w	18:20:10	0:50:00
Menter k-w	19:03:56	0:52:00
RQEVM	19:15:42	0:52:32

Table 5: LARS turbulence models with 2 cores

As visible in the previous histogram and related table, the computation times for these linearized analyses are similar. This is valid for both total time and mean time for each nodal diameter.

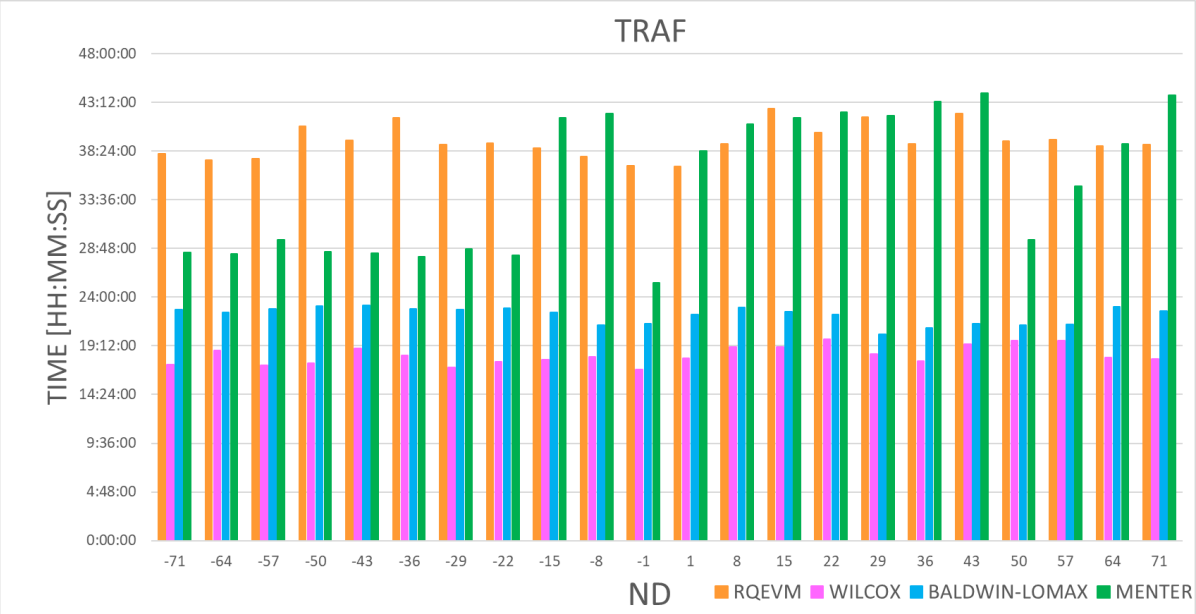

Figure 72: Computation time TRAF

TRAF WITH 2 CORES		
TURBULENCE MODEL	TOTAL TIME [hh:mm:ss]	MEAN TIME ND [hh:mm:ss]
Baldwin-Lomax	489:19:19	22:14:31
Wilcox k-w	402:44:38	18:18:24
Menter k-w	777:40:34	35:20:56
RQEVM	865:56:32	39:21:40

Table 6: TRAF turbulence models with 2 cores

As visible in the previous histogram and linked table, the total computation time increases with the turbulence model complexity, except for the Baldwin-Lomax, that has a computation time higher than Wilcox k-w. This could be possible due to the HPC, the cluster on which were run the analyses, but also to the complexity of equations.

5.7 Sensitivity on solver software

Let's take a closer look to differences visible between flutter simulation with linearized and non-linearized equations with the four turbulence models.

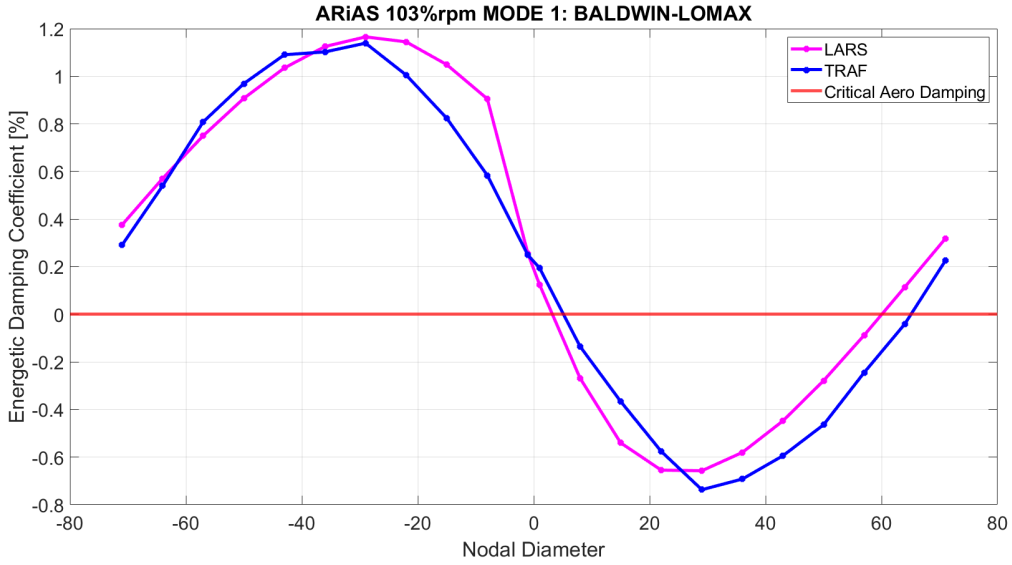

Figure 73: LARS vs TRAF with BALDWIN-LOMAX

With *Baldwin-Lomax* for linearized and non-linearized simulations the most unstable nodal diameter is the ND=29.

BALDWIN-LOMAX		
Solver	Aerodamping ND=22 [%]	Aerodamping ND=29 [%]
LARS	-0.654634	-0.657257
TRAF	-0.576083	-0.736893

Table 7: Baldwin-Lomax LARS vs TRAF ND 22 29

In the next histogram is visible the difference regarding the computation time, with 8 cores, between linearized and non-linearized simulation for Baldwin-Lomax.

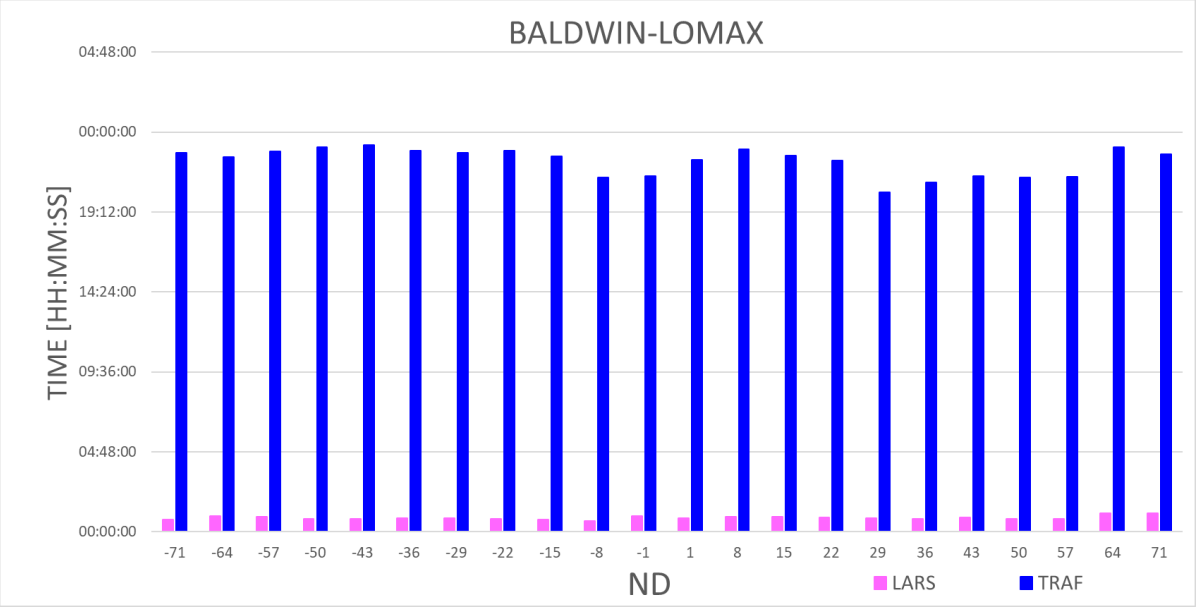

Figure 74: Histogram Lars vs Traf Baldwin-Lomax

For the other turbulence models, the most unstable nodal diameter is always the ND=22 for linearized and ND=29 for non-linearized simulations, as visible in the following plots and tables.

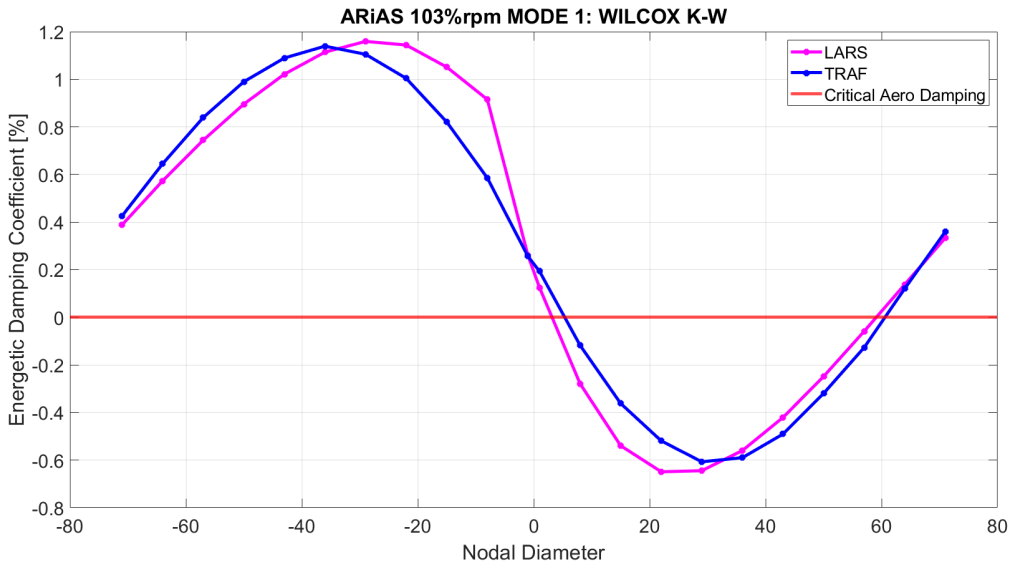

Figure 75: LARS vs TRAF with WILCOX K-W

WILCOX K-W		
Solver	Aerodamping ND=22 [%]	Aerodamping ND=29 [%]
LARS	-0.648922	-0.644579
TRAF	-0.519077	-0.607005

Table 8: Wilcox k-w LARS vs TRAF ND 22 29

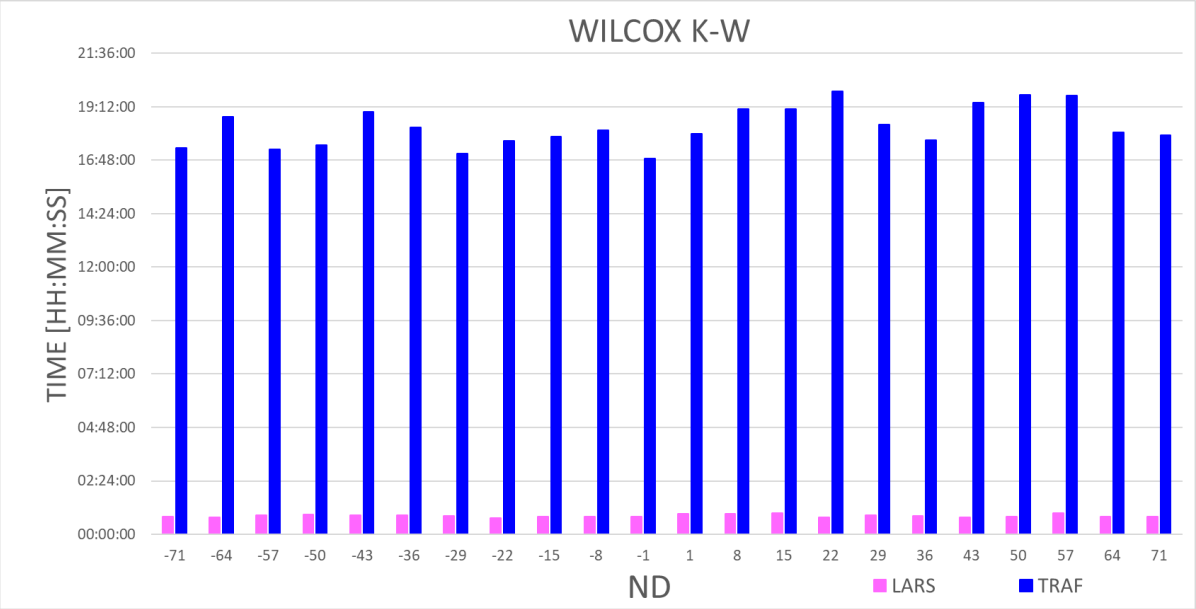

Figure 76: Histogram Lars vs Traf Wilcox k-w

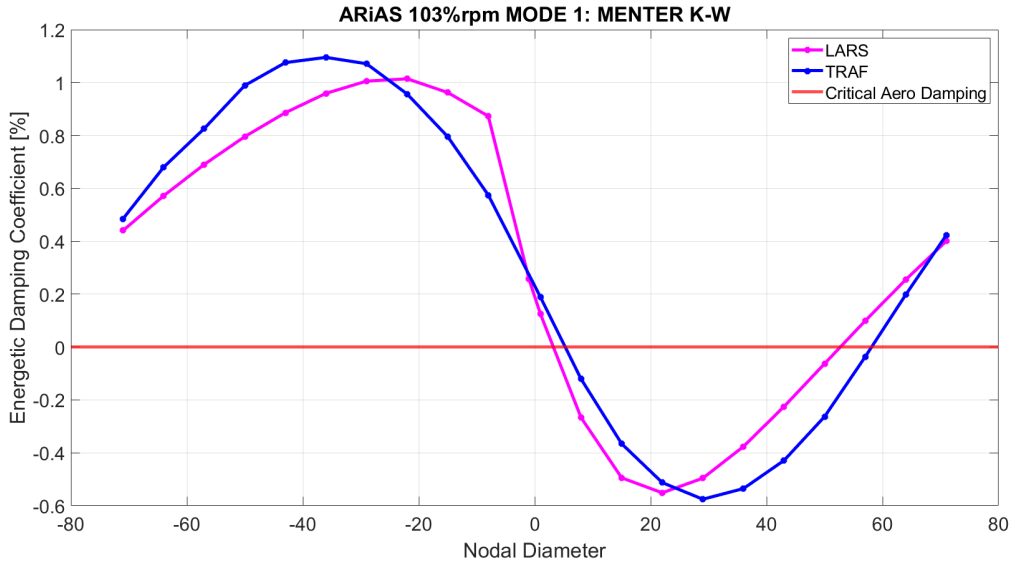

Figure 77: LARS vs TRAF with MENTER K-W

MENTER K-W		
Solver	Aerodamping ND=22 [%]	Aerodamping ND=29 [%]
LARS	-0.551091	-0.495856
TRAF	-0.512498	-0.575371

Table 9: Menter k-w LARS vs TRAF ND 22 29

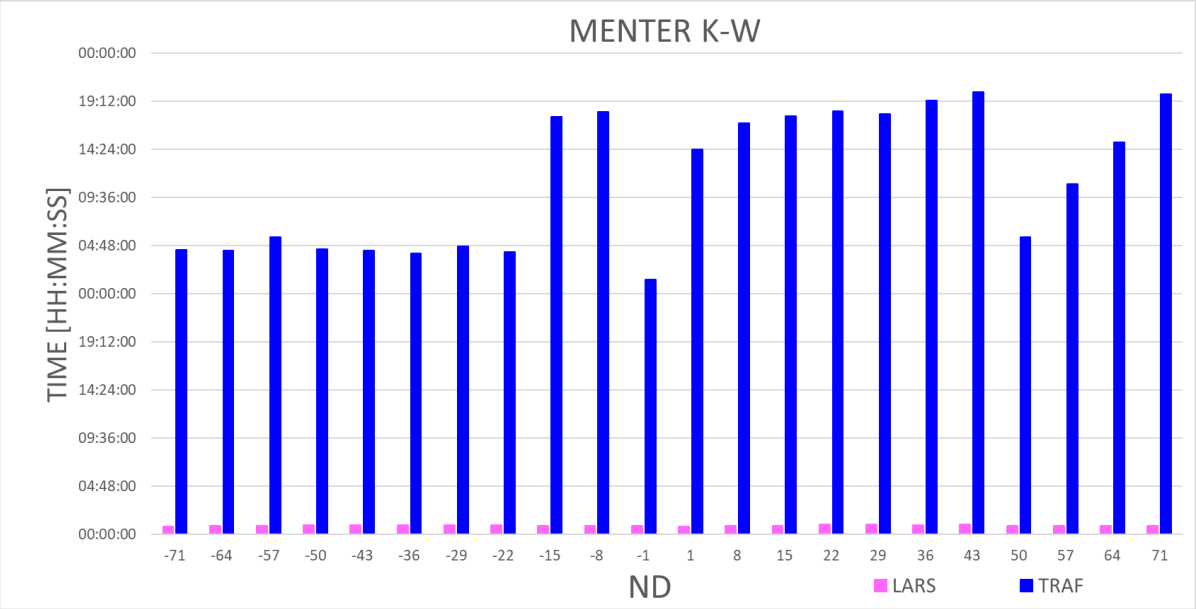

Figure 78: Histogram Lars vs Traf Menter

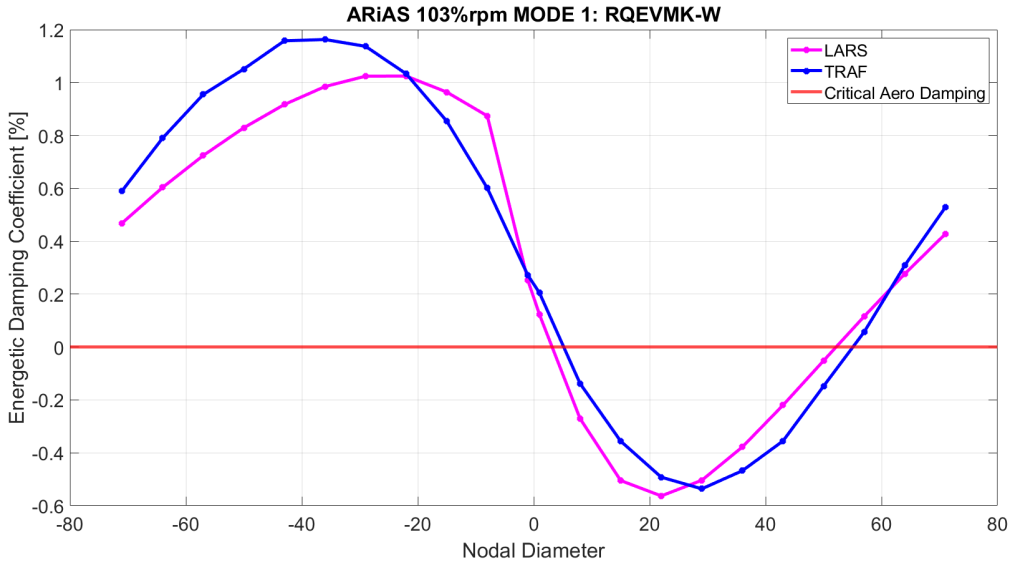

Figure 79: LARS vs TRAF with RQEVM

RQEVM		
Solver	Aerodamping ND=22 [%]	Aerodamping ND=29 [%]
LARS	-0.562883	-0.50374
TRAF	-0.492066	-0.536064

Table 10: RQEVM LARS vs TRAF ND 22 29

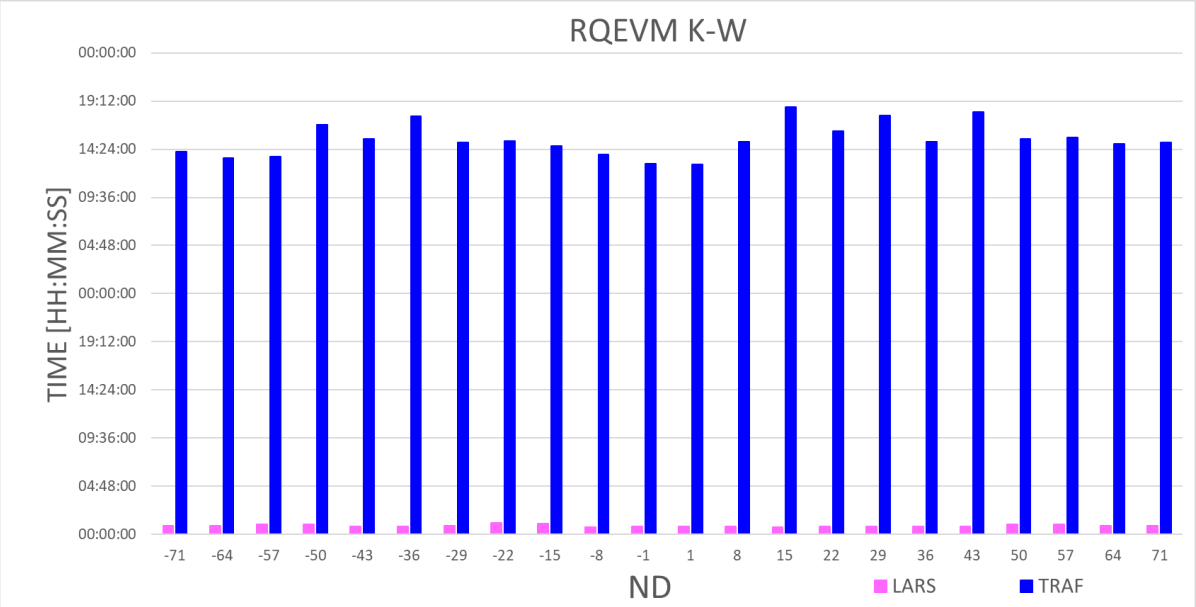

Figure 80: Histogram Lars vs Traf RQEVM

As it's possible to see, as said before, the TRAF computation has taken more time than the LARS ones.

6 Conclusions

In the case study analyzed, the CFD domain was always subsonic and there was no presence of non-linearity. This means that the analyses run, could have been done with the Linearized solver only, with a substantial time saving. The Non-Linearized solver need to be applied if there are non-linearities in the CFD domain as shock waves and separation flows.

With the two solvers, the most unstable nodal diameter changes: for Linearized is ND=22, except for Baldwin-Lomax model is ND=29, and for Non-Linearized it is always ND=29.

Improving the closure turbulence model, with non-linearized solver, the simulations take more time. The simplest turbulence model is more conservative because it overestimates the value of the most unstable nodal diameter of about 30%. If we need to determine if the blade is stable or not, it's possible to use the simplest turbulence model to save time. If the values of aerodamping are near the zero (critical damping ratio) and so a more accurate solution is required (i.e. value of a certain ND), it can be better to use the RQEVM k-w turbulence model.

Talking about the Linearized method, the calculation times are similar because it solves linearized equations and also the values of aerodamping aren't so different. If a more accurate solution is required, it is possible to implement the RQEVM k-w model, without increasing the computational cost.

References

[1] *E-TDCs ABSTRACT* 2021.11.29

[2] *ARiAS Project*, https://www.arias-project.eu/, [Last Access 21/05/2024]

[3] https://www.avioaero.com/_nuxt/assets/images/Logo-Avio-Footer.svg

[4] https://it.wikipedia.org/wiki/File:Logo_PoliTo_dal_2021_blu.png

[5] https://en.wikipedia.org/wiki/Turbojet/media/File:Jet_engine.svg, [Last Access 21/05/2024]

[6] https://www.geaerospace.com/sites/default/files/2023-09/GEnx-1B_Side_Closed_8K-sml.png, [Last Access 21/05/2024]

[7] https://en.wikipedia.org/wiki/Turboprop/media/File:JMSDF_P-2J_T64-IHI-10E_turboprop_engine_left_side_view_at_Kanoya_Naval_Air_Base_Museum_April_29,_2017.jpg, [Last Access 21/05/2024]

[8] https://en.wikipedia.org/wiki/Turboshaft#/media\/File:Turboshaft_operation_(multilanguage).svg, [Last Access 21/05/2024]

[9] https://link.springer.com/chapter/10.1007/978-3-030-28691-0_5, [Last Access 24/04/2024]

[10] https://earthscience.stackexchange.com/questions/2932\/what-are-the-differences-between-an-les-sgs-model-and-a-rans\-based-turbulence-mo%7D

[11] https://www.mm.bme.hu/~gyebro/files/ans_help_v182/ans_cmd/Hlp_C_RBE3.html

[12] https://www.researchgate.net/figure/Figure-1-Boundary-layer-for\-turbulent-flow-over-flat-plate_fig1_309160033 [Last Access 04/07/2024]

[13] Zucca Stefano, Botto Daniele. (2021) Slides del corso "Dinamica dei rotori per applicazioni Aerospaziali", Politecnico di Torino.

[14] Pinelli Lorenzo, (2024) Slides del corso sul Flutter, Avio Aero.

[15] A.Ferrero (2023) Appunti del corso "Fluidodinamica computazionale dei Sistemi

Propulsivi", Politecnico di Torino.

[16] Pinelli Lorenzo, (2024) Slides del corso sul Flutter, Avio Aero.

[17] Baldwin, B. S. and Lomax, H., 1978, *"Thin Layer Approximation and Algebraic Model for Separated Turbulent Flows"*. AIAA paper 78–257, 16th Aerospace Sciences Meeting, January 16–18, Huntsville, AL, USA

[18] Durbin, P. A., 1996, *"On the k–ϵ Stagnation Point Anomaly"*. International Journal of Heat and Fluid Flow, Vol. 17, pp. 89–90.

[19] Franke, M., Wallin, S., and Thiele, F., 2005, *"Assessment of Explicit Algebraic Reynolds-Stress Turbulence Models in Aerodynamic Computations"*. Aerosp. Sci. Technol., Vol. 9, pp. 573–581.

[20] Gatski, T. B. and Speziale, C. G., 1993, "On Explicit Algebraic Stress Models for Complex Turbulent Flows". J. Fluid Mech., Vol. 254, pp. 59–78

[21] Rung, T., Lubcke, H., Franke, M., Xue, L., Thiele, F., and Fu, S. *"Assessment of Explicit Algebraic ¨ Stress Models in Transonic Flows"*. In Rodi, W. and Laurence, D., editors, Engineering Turbulence Modelling and Experiments - 4, pp. 659–668. Elsevier, Amsterdam, 1999

[22] Wilcox, D. C., 1998, *Turbulence Modeling for CFD*, 2nd edition, DCW Ind. Inc., La Canada, CA, ~ USA, ISBN 1-928729-10-X

[23] Wilcox, D. C., 2008, *"Formulation of the $k-\omega$ Turbulence Model Revisited"*. AIAA J., Vol. 46, No. 11, pp. 2823–2838

[24] *THE ROLE OF OPERATING CONDITIONS ON FLUTTER INSTABILITY OF A LOW-PRESSURE TURBINE ROTOR* Lorenzo Pinelli, Francesco Poli, Andrea Arnone,Antonio Giuseppe D'Ettole, Emanuele Rosso, Gianmaria Sartor,Vsevolod Kharyton- Department of Industrial Engineering, University of Florence, Firenze, Italy;Avio Aero – a GE Aerospace company, Torino, Italy; Siemens Energy AB, Finspång, Sweden